Cluster Formation in Supersonic Beams of Dense Fluids: A Surface Scattering Study

DISSERTATION

zur Erlangung des akademischen Grades

doctor rerum naturalium

(Dr. rer. nat.)

im Fach Chemie

Spezialisierung: Physikalische und Theoretische Chemie

eingereicht an der

Mathematisch-Naturwissenschaftlichen Fakultät

Humboldt-Universität zu Berlin

von

Herr M.Sc. Bo-Gaun Chen

Präsident der Humboldt-Universität zu Berlin:

Prof. Dr. Jan-Hendrik Olbertz

Dekan der Mathematisch-Naturwissenschaftlichen Fakultät:

Prof. Dr. Elmar Kulke

Gutachter:

1. Prof. Dr. Klaus Rademann

2. Prof. Dr. Hans-Joachim Freund

eingereicht am: 24.02.2015

Tag der mündlichen Prüfung: 17.04.2015

Dedication

To my family and my mentors.

Zusammenfassung

Mit zeitaufgelöster Massenspektrometrie untersuchen wir die Winkelverteilung von Kohlendioxid-Monomeren bei der Streuung von Kohlendioxid-Clustern an einer Si(111)/Siliciumdioxid-Oberfläche unter Ultrahochvakuum-Bedingungen. Die präsentierten Studien decken eine große Breite der Clustergrößen, $\langle N \rangle$, $10^3 < N < 2\times10^5$ Moleküle pro Partikel, ab. Dabei liegt der Fokus auf dem Einfluss der Ausgangsentropie, die durch eine präzise Einstellung des Ausgangsdruckes und der Düsentemperatur realisiert wurde. Es zeigt sich, daß die Streuverteilung direkt den Expansionspfad widerspiegelt, wodurch eine Unterscheidung zwischen Clustern, die durch eine Expansion auf der gasförmigen oder flüssigen Seite des kritischen Punktes und der metstabilen Phase entstehen, ermöglicht wird.

Um bei den hohen Teilchendichten eine verlässliche Aussage zu ermöglichen, wurden im Vorfeld die Eigenschaften gepulster Molekularstrahlen untersucht, insbesondere deren Abhängigkeit vom Restgasdruck und den Wechselwirkungen mit Strahlblenden. Hierzu diente die elektronische Anregung eines Helium-Strahls. Die Optimierung der Randbedingungen ermöglicht viel kältere Strahlen, so dass Helium-Cluster sogar bei einer Ausgangstemperatur von T = 410.0 K gefunden werden können. Dieses Ergebnis ist für die Cluster-Forschung, die Molekülspektroskopie und Experimente in der Quantenphysik von Bedeutung.

Schlagwörter: Atom/Molekular Cluster, Strahl-Blende-Wechselwirkung, Cluster-Bildung, Oberflächenstreuung

Abstract

Employing pulsed high-pressure supersonic jet expansion and a dedicated setup for the experimental investigation of chemical processes occurring between neutral, van der Waals bound clusters and a solid surface, we report on the angular distribution observed for large carbon dioxide clusters scattered off a Si(111)/Silicon Dioxide surface under ultrahigh vacuum conditions. Scattered particles are detected using angle and time resolved mass spectrometry. The presented studies cover a broad range of cluster sizes, $\langle N \rangle$, $10^3 < N < 2\times10^5$ molecules per particle. The focus is on the influence of source entropy, realized by accurately setting stagnation pressure and temperature. This thesis demonstrates a dependence of the angular distribution of scattered carbon dioxide monomers on source conditions: the scattering distribution directly reflects the expansion path, allowing us to distinguish between clusters generated via expansion on the gaseous or on the liquid side of the critical point, and an intermediate regime where the expansion passes the metastable gas-liquid region.

To optimize the supersonic beam, on the other hand, we reveal a substantial influence of residual gas pressure and beam–skimmer interactions on beam properties, particularly the minimum attainable translational temperature in a model system. This study contains the systematic investigation of supersonic jet expansions of helium at source conditions of $P = 0.60 – 9.60$ MPa, $T = 228.0 – 410.0$ K, employing the variable distance between the Even-Lavie valve and different types of skimmers. Utilizing the ultra-high precision time-of-flight measurements of electronically tagged particles, the detected terminal velocities and the spread of particles allow us to correspondingly obtain much colder beams with the same source conditions. As a result, helium clusters can be found even in the jet expansion from a source temperature of $T = 410.0$ K, meaning that the improved settings allow for better control of the cluster beams. This knowledge is of particular interest to cluster science, molecular spectroscopy, and quantum physics.

Keywords: Atomic/Molecular Clusters, Beam Skimmer Interaction, Cluster Formation, Surface Scattering

Table of Contents

List of Figures

List of Tables

CHAPTER 1

1 Introduction

1.1 Background

"Clusters" in the natural sciences involves several aspects. In astronomy, a cluster usually represents a spherical collection of stars,[1] in geoscience, a cluster often refers to the aggregated aerosol particles in the atmosphere. A biological cluster may indicate a group of genes/proteins that are similar in functionalities; while for materials science, a cluster is called a nanoparticle (NP) with the size of 1–100 nm.[2-5] In chemistry, a cluster can be a group of bonded atoms or molecules that is intermediary in size rather than a bulk phase, or it can be a certain kind of molecules in a confined space,[6] and in physics, a cluster donates multi atom particles from 2 up to 10^7 atoms.[7-12] Clearly, clusters play an important role in bridging the gap between singular elements and the macroscopic materials in modern technology. Therefore, both theoretical and experimental studies of cluster formation have received much attention over the last century.[13-20]

To produce clusters, organic and inorganic chemists normally synthesize the desired product from the molecular level in the solution. A solution offers a surrounding to control the concentration of each compound. In addition, the high mobility in the solution allows the chemical reaction to easily reach the equilibrium within a short time period. As a result, the synthesized clusters might contain both the anticipated bonding as well as the modification of the functional groups.[21,22] Recently, using organometallic clusters as a building blocks to construct nanoparticles, two-dimensional (2D) linear polymers[23] and two or three dimensional (2/3D) metal-organic frameworks (MOFs)[24,25] have been discussed abundantly. Such systems have great potential for energy generation, efficient catalysis, novel semi-/conducting materials and gas storage/separation.

Parallel to the synthesis of clusters, many analytic techniques allow for the separation and identification of those aggregated particles, which is essential for defining the desired physical properties. Depending on the type of samples, several methods are used accordingly. For solid samples, scanning/transmission electron microscope (SEM/TEM) and atomic force microscopy (AFM) are used as direct physical contacts to measure the size or energy distribution of the clusters, while the magnetic investigation (e.g. magnetic resonance force microscopy, MRFM, and superconducting quantum interference device, SQUID) conducts secondary information from those clusters. For samples in solution, nuclear magnetic resonance (NMR) provides the chemical shift relating to structural information, high performance liquid chromatography (HPLC) separates the mixed clusters by polarity and the optical methods (e.g., UV/Vis, IR, Raman, and X-ray) identify the energetic properties of each cluster. For samples in the gas phase, various types of mass spectrometers are applied to define the weight and size distribution of clusters in two steps:

sampling and mass analysis. Sampling often requires a transfer process to carry clusters into the gas phase, and subsequently excite/ionize those clusters to highly energetic status (e.g., chemical ionization, CI; electronic ionization, EI; field ionization, FI, and matrix-assisted laser desorption, MALDI[26-28]). After that, those charged clusters are detected by different mass spectrometers through several mechanisms, which include sector instrument, ion traps, Fourier transform ion cyclotron resonance (FT-ICR), radio-frequency quadrupole mass filter and time-of-flight (TOF).[29-34]

Aiming to improve the efficiency and resolution of all these analytical methods, the cluster formation mechanism with respect to each technique was studied by a theoretical model construction and experimental parameter optimization. In particular, the molecular dynamics simulations are widely used to depict the straight formation/degradation mechanism of neutral/ionic clusters, for which the velocity is very important in defining the energetic status of each particle.[15,35-38] Nevertheless, the theoretical calculation are still limited by the computational power, especially when the calculation requires a large number of particles and very small time steps. The experimental data is therefore needed to pioneer the research.

Concerning to the determination of particle energy in physical chemistry experiments, supersonic molecular beams are useful tools to probe basic physical properties. The weakly bound atomic and molecular clusters are often attractive because they contain the simplest bonding mode, which is essential to construct a model for application to more complex systems. Many experimental and theoretical studies in relation to the van der Waals (vdW) clusters have been described in past few decades.[36,39-45] By focusing on structural information or the measurements of binding energies, these results from the vdW clusters were proved to bridge the ideal gas to real gas system and thus improve the understanding of nucleation processes. The regulation of cluster growth has received much attention in both academic and industrial topics in 21th century such as astrophysics, atmospheric dynamics and the size controlling of nanoparticles (NPs).[2,20,46-48]

1.2 Research Objectives

The motivation of this work is to correlate the fundamental thermodynamic equation of state to the physical properties of clusters and to improve the knowledge of the cluster surface interaction with various sizes of clusters. These two objectives will contribute to cluster sciences and surface sciences.

Aiming to characterize the source conditions, the noble gas - helium - will be used as a reference experiment to optimize the mechanical settings of molecular beam instruments. Since an ideal gas like helium minimizes the condensation probability during the jet expansion from ambient temperature, the measurements from helium expansion should be easier to monitor various flow properties such as particle spread, velocity and the temperature of the beam. These results will be compared to the theoretical predictions of thermodynamics.

Following from this, the improved regulation of instruments should apply to the real gas system of carbon dioxide. Because the chemically inert CO_2 not only provides simple bonding modes for analysis, but also can be easily compared to the unambiguous database in literature. By accurately and comprehensively control the CO_2 jet expansions from the vapor to supercritical to liquid phases, the condensed clusters in the beam give an opportunity to extend the nucleation theory to the ultra-high density region, which is currently limited in theoretical simulations by the number of total particles. Consequently, the generated $(CO_2)_N$ clusters and the ionized $(CO_2)_N^+$ beams will be evaluated directly via time-resolved detection to learn about the size distributions and velocities by a micro-channel plate detector. Also, the neutral $(CO_2)_N$ cluster beams will undergo surface scattering off $Si(111)/SiO_2$ to obtain the scattering pattern and to verify the collision channel by quadrupole mass spectrometry. The direct and indirect analysis of supersonic beams thus can provide kinetic and size information of those clusters, respectively. These outcomes are expected to contribute to the fundamental issues of condensation and real fluid properties of nozzle flow.

In combination with a state-of-the-art machine for ultra-high precision measurements as well as advanced statistics for all model descriptions, all the above-mentioned results should concrete the bridge between micro- and macroscopic world, and further develop the understanding of nano-material science.

1.3 Thesis Content

Chapter 2 gives an overview of the experimental setup of supersonic molecular beam expansion, focusing on the cluster jet and its size distribution. Combined with the numerical and statistical evaluation of time-of-flight spectra, the fitting result ensures the precise determination of physical properties. This chapter also shortly introduces the analysis of scattering angular distribution after the cluster surface interactions.

Chapter 3 describes the improvement of translational cooling of the supersonic beam. It starts by defining the steady state condition of pulsed expansion from ultra-high pressure, the result provides extremely precise velocity determination of helium beams. This is followed by a carefully investigating of the effect of interference; the outcome further demonstrates the advanced control of sensitive clusters in the beam.

Chapter 4 pertains to the physical properties of the $(CO_2)_N$ clusters generated via high-pressure jet expansion. The macroscopic temperature of the cluster is derived from the thermal dynamic equation of state (EOS), which incorporates the precise beam velocity and the concept of isentropic expansion pathway. For the main topic concerning to the surface scattering of $(CO_2)_N$ clusters off Si(111)/SiO_2, broad range of cluster sizes is covered, $\langle N \rangle$, $5\times10^3 < N < 2\times10^5$ molecules per particle. Focus is on the influence of source entropy, realized by accurately setting stagnation pressure and temperature. A dependence of the angular distribution of scattered CO_2 monomers on source conditions is reported: the scattering distribution directly reflects the expansion path, allowing clusters generated via expansion on the gaseous or on the liquid side of the critical point to be distinguished. An intermediate regime where the expansion passes the metastable gas-liquid region can also be addressed. These studies result in a better understanding of the cluster formation channel with respect to the source conditions in the vicinity of the critical point.

Chapter 5 summarizes the results from this thesis and an outlook for the future work.

CHAPTER 2

2 Experimental Setup and Basic Principles

A supersonic atomic/molecular beam is formed when a gas is expanded from a region of higher pressure to a region of extremely low pressure, through a certain geometry of a nozzle with a small orifice. Supersonic atomic/molecular beams have advantages on the energy-related research topics because of the adiabatic environment. Thus, supersonic beams are applied to various scientific purposes. Depending on the aim of the research project, one should customize a state-of-the-are machine and analyze the output data precisely.

2.1 Experimental Setup: Ultra High Vacuum System

Ultrahigh vacuum (UHV) conditions are achieved using completely hydrocarbon-free pumping stages, consisting of magnetically levitated turbo molecular pumps which are backed by chemically inert diaphragm pumps. A dedicated chamber also allows angle- and energy-resolved investigations of cluster-surface collisions, see Figure 2.1-1.

The machine can be described in five parts. (1) Pulsed supersonic high-pressure jet source, which is capable of operating at the source pressure of 0.20 – 12.0 MPa. (2) A shielded electron gun for electronic excitation or electron impact ionization. (3) Two skimmers with diameters of ϕ: 2.0 mm and ϕ: 3.0 mm, both can be replaced according to the specific experimental need. (4) Two different detectors: multichannel plate (MCP) and quadrupole mass spectrometer (QMS). (5) A Si(111)/SiO_2 surface is mounted on a *xyz*-translator with 360° rotatable holder for surface scattering experiment.

Additionally, four linear translators are mounted in this state-of-the-art machine for different purposes: (a) 0 – 600 mm TD_z: the tunable distance contains a tolerance of setting of less than 50 μm, which allows the multichannel plate (MCP) detector to precisely determine the terminal beam velocity in combined with the mean time-of-flight; (b) 0 – 50 mm TB_y: the tunable distance contains a tolerance of setting of less than 10 μm, which allows the beam blocker to precisely define the vertical spread of particles; (c) 0 – 200 mm TQ_y: the tunable distance contains a tolerance of setting of less than 50 μm, which allows the quadrupole mass spectrometer (QMS) detector to precisely determine the scattered beam velocity when combined with the mean time-of-flight. Also, the QMS can probe the direct beam by lowering the *y*-position; (d) 0 – 200 mm TN_z: the tunable distance contains a tolerance setting of better than 50 μm, which permits a systematic optimization of beam transmission for different source densities by adjusting the nozzle to first skimmer distance ($d_{N–S}$: 33.3 – 233.3 mm). In addition, the translator TN also offers *xy*-adjustments to precisely centralize the nozzle to the skimmer with a tolerance of better than 10 μm.

Surface scattering chamber includes quadrupole mass spectrometer (QMS) with liquid nitrogen cooled shroud. The ion getter pump (N_2 pumping speed exceeding 150 Ls^{-1}), titanium sublimation pump (N_2 pumping speed of 500 Ls^{-1}), and turbo molecular pump (N_2 pumping speed of 400 Ls^{-1}) provide a base pressure of 2×10^{-8} Pa without baking. All chambers are connected via gate valves.

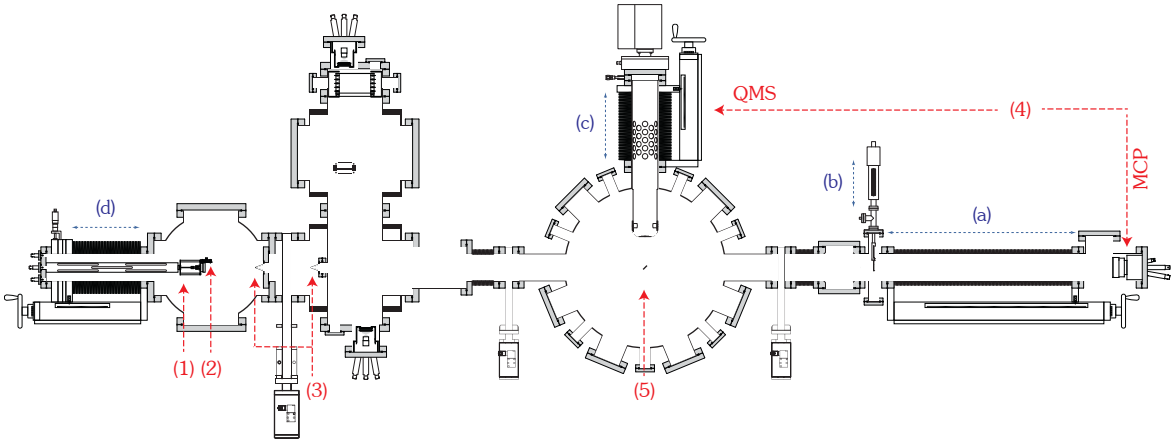

Figure 2.1-1 Overall system configuration in this study, detailed design has been published.[32,49-51] Equipped with a liquid nitrogen cold trap, an ion getter pump, and a titanium sublimation pump it permits pressures down to 10^{-8} Pa.

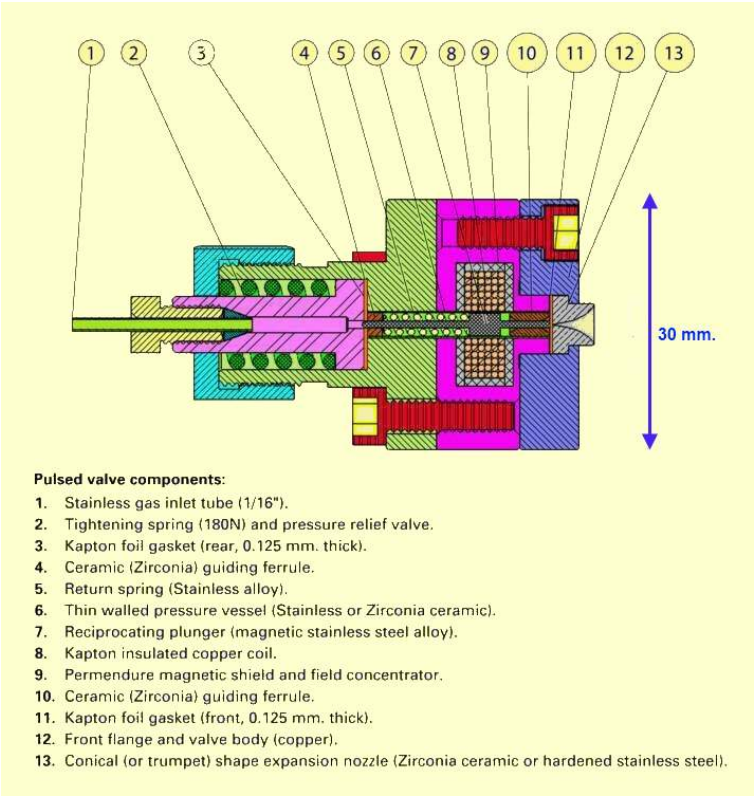

Figure 2.1-2 Detailed configurations of Even-Lavie valve. Current model contains a 0.10 mm diameter of the gas outlet, which is followed by a trumpet expansion nozzle. (https://sites.google.com/site/evenlavievalve)

2.1.1 Cluster-Ion Generation

- **Pulsed Nozzle**

Supersonic atomic/cluster beams were formed by pulsed fluid expansion with a solenoid nozzle. The nozzle allows source condition of high pressure and temperature, which is also suitable to cryogenic operation. A new design of jet source is introduced by Even *et al.* with the invention of a valve.[16] This valve in our experiment is customized by Nachum Lavie (School of Chemistry, Tel-Aviv University, Israel) for optimizing the cluster formation, and the valve body is manufactured from stainless steel and can be electrically heated to temperatures of up to 450 K, see Figure 2.1-2. The maximum of sampling rate is up to 25 Hz.

For operational specification in experiments, a syringe pump (Teledyne Isco, Inc., 500D, USA) is used to control the stagnation pressure of P_0 = 0.20 – 12.0 MPa. The gas reservoir is further temperature maintained by a circulation system (Julabo Labortechnik GmbH, FP 50, Germany). On the other hand, the stagnation temperature of source is controlled by highly dynamic temperature system (Julabo Labortechnik GmbH, LH85, Germany) to work in the range of T_0 = 225.0 – 425.0 K. This temperature is given by a NiCr/Ni thermocouple, which is spot-welded to the exterior of the valve body. A custom built active temperature controlling experimental setup is used for the stabilization and control of the stagnation conditions (ΔT_0 < 30 mK and ΔP_0 < 2.9 kPa).[32,51] For helium expansions, the standard valve controller adjusts the opening duration to δt_0 = 25 μs at source pressure of 9.60 MPa and source temperature of 319.0 K, which reduces the gas usage and maintains good vacuum condition in expansion chamber at the same time. On the other hand, for CO_2 jets, the pulse duration is controlled at δt_0 = 18 μs for all source temperatures and pressures.

Experimentally, the real opening duration is determined by reaching the stationary flow condition at given the source density, the actual valve setting is thus required further systematic study in section 3.1. In addition, this high-pressure jet source is mounted on a *xyz* precision translation stage. The *xy* stage permits movements of ± 12.5 mm with a resolution of 10 μm for the accurate alignment of the valve with respect to the axis defined by the two skimmers in the downstream side. Finally, the nozzle exit has a diameter of 0.1 mm with a parabolic shape, providing an improved collimation of the expanding flow.

- **Chemicals**

In this study, Helium-4 gas with a specified purity of 99.9999% (Helium 6.0, Air Liquide) or carbon dioxide with a specified purity of 99.9995% (Air Liquide) is expanded into vacuum.

- **Electron Gun**

Owing to improve the knowledge of weakly bonded clusters, this study required an efficient method to generate gas-phase ions from cluster beams and subsequently analyzed by either time-of-flight detector or quadrupole mass spectrometer. In general, supersonic expansions result size distributed clusters, the width of this distribution is based on the

bonding mode of given molecules, source pressures together with temperatures, and the type of nozzle as well as its pulse duration.

For some methods such as chemical ionization (CI) or electrospray ionization (ESI) or matrix-assisted laser desorption ionization (MALDI), although all these soft ways reduce fragmentation during the process of ionization, the added ion(s) might influence the physical properties of target clusters. In this study, however, we will also focus on the terminal physical properties to derive the macroscopic thermodynamic status. Direct ionization would thus be the optimal type of method to excite clusters. One may still consider photoionization (PI) with lasers for higher efficiency, but the selectivity of wavelength-specific excitation
limits the application to various clusters. When the molecules undergo their single photon absorption process in the ultraviolet regime,[52] the strong degradation of clusters is also not desired in following experiments. To sum up, among many tools of ionization as listed in Table 2.1-1, electron impact (EI) is a widely recognized method to preform ions in the early stage.

Table 2.1-1 Ionization methods of atomic/cluster beam research.

Ionization method	*Electron impact (EI)*	*Chemical ionization (CI)*	*Field ionization (FI)*	*Electrospray ionization (ESI)*	*Matrix-assisted laser desorption ionization (MALDI)*
Type	hard/mild[a]	mild	mild	mild	mild
Mass Limit	~ 10^4 Da	~ 10^3 Da	~ 10^3 Da	~ 2×10^6 Da	~ 5×10^6 Da
Phase	(*g*), (*l*), (*s*)	(*g*), (*l*), (*s*)	(*g*), (*l*), (*s*)	(*g*), (*l*)	(*g*), (*s*) in matrices
Ions	M^+, M^-	$[M+H]^+$, $[M+X]^+$	$[M+H]^+$, $[M+X]^+$	$[M+nH]^{n+}$, $[M-nX]^{n-}$	$[M+H]^+$, $[M+X]^+$
Analytes	volatiles, clusters	volatiles, clusters	volatiles	peptides, proteins, injected nonvolatiles	clusters, peptides, proteins, nucleotides

[a] The placement of e-gun in the early stage of cluster formation reduces the overall fragmentation as electrons impact the growing clusters.

With advanced control in low electronic energy and focusing, EI provides either negative or positive species depending on the nature of the neutral sample with reduced fragmentation of original clusters.[53,54] Normally the ionization probability is maximized between 50 – 100 eV, where the electron current and effective electron energy is related to the ion yield after the electron attach-/detachment process.[33] To optimize this electron current, space charge effect of the beam is the essential parameter.[55]

In this thesis, current setting of cluster source is to place the electron gun (e-gun) at the nozzle exit. According to the need of probing the journey of cluster development, the screw mounted e-gun body can be adjusted to ~ 8 mm to excite the beam from different positions. When the strong collisional clustering happens in front of the nozzle exit, after the

ionization by e-gun, those ionized particles are still able to grow further by attaching more proximate particles.[56] Therefore, the fragmentation of clusters is reduced by this design and the slightly warmer ion clusters can continue the collisional cooling process afterward, which simultaneously benefit for the study of low temperature clusters in a supersonic beam.

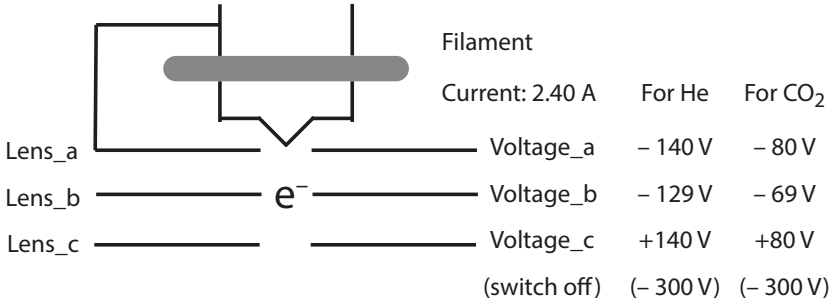

Figure 2.1-3 Schematic drawing of the electron source (e-gun), the emitted electron stream is focused by three einzel lenses. According to different working fluids, the focus by electronic field must be optimized to ensure the excitation/ionization efficiency. Two settings with respect to helium (He) and carbon dioxide (CO_2) are listed on the right side.

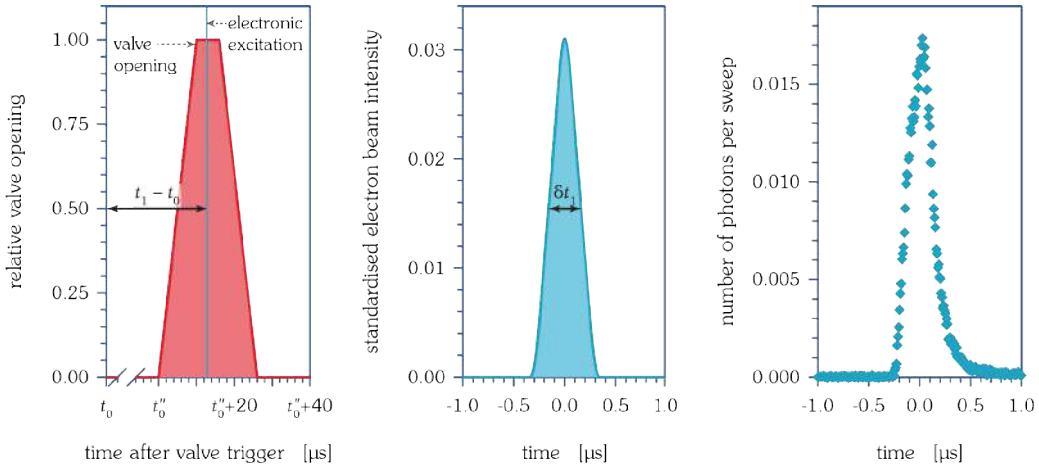

Figure 2.1-4 Schematic excitation process of helium beam.[50] (*left*) A trapezoidal shape of a pulsed beam starts at the t_0'', which is electronically excited by e-gun at t_1. (*central*) This electronic excitation at t_1 lasts for a time period of δt_1. (*right*) The excited helium particles in the beam partially undergo a sudden quenching process, which yields the emission of ultraviolet photons. This resulting sharp peak is evaluated to have a peak spread of $\approx \delta t_1$ (full width of half maximum, FWHM), when δt_1 is shorter than 3 µs.

All experimental settings of shielded e-gun is constantly providing electron current of 2.40 A to the jig-formed filament (Agar Scientific, AGA054, U.K.), and the focused electron beam is directed perpendicularly to the axis of the expanding gas jet. For carbon dioxide and helium beams, as shown in Figure 2.1-3, electron energy of 80 ± 1 eV and 140 ± 1 eV were applied to excite these supersonic beams,[57] respectively. After applying

given voltage to the filament, the emitted electrons are focused by two electronic lenses to improve the excitation. Finally, the output electrode reduces space charge effects by operating in a pulsed mode with pulse duration as short as 100 ns, which provides high resolution in slicing scan in each part of pulsed beams. Figure 2.1-4 demonstrates an example of electronic excitation process of helium beam, which results in a quick ultraviolet quenching peak from the de-excited helium particles. The result shows a well-defined and desirable peak shape for a 300 ns excitation.

- **Skimmer**

Two skimmers are located at the downstream of the nozzle between the first and the second chamber, in order to eliminate the outer shell of the beam. In the study of beam–skimmer interaction, the first skimmer (closer to the nozzle) can be replaced by mechanic drilled skimmer (ϕ: 3.0 mm), thin nickel skimmer (ϕ: 3.0 mm, Beam Dynamics, Inc.) and thin nickel skimmer (ϕ: 2.0 mm, Beam Dynamics, Inc.), while the second skimmer (ϕ: 3.0 mm) is fixed at 209 mm downstream to the first skimmer.

2.1.2 Detection System

- **Microchannel Plate Detector**

A fast and sensitive detector is needed for a linear time-of-flight mass spectrometer, because, in general, the response time of the employed detector defines the upper limit of the maximum possible resolution. The advantage of ion detection with micro-channel plate (MCP) detectors[58] evolved to the default detection method in time-of-flight spectrum alongside many other methods.

Most of the MCP detectors offer fast rise times (below 500 ps) of an output signal and large detection areas (up to a diameter of ϕ = 40 mm). For the advanced setup such as Chevron configuration (V-like)[59] improves the signal gain by combining two MCPs with angled channels rotated 180° from each other, or the Z-stack with three MCPs for even higher signal intensity (about 100 times compared to single MCP). In this experiment, we use a high-speed bipolar MCP hybrid device with a sensitive area of ϕ = 40 mm (Burle, Inc., USA), which contains of a MCP (convert ion-to-electron) and amplification, a scintillator surface (convert electron-to-photon) and a photomultiplier tube (PMT). By this configuration, this MCP detector offers the post acceleration of both positive and negative ions with up to 10 kV.

Such distinguished feature is important for detecting large and heavy species,[26,53,60] a surprising result of the observation of neutral $(CO_2)_N$ clusters from high-density jets by this detector will be discussed in Chapter 4. In addition to precisely measuring the velocity of the beam, this detector is mounted on a linear translation stage along the central line of the expanded jet. The tunable range is from 0 – 600.0 mm and a tolerance of setting is less than 50 μm.

- **Quadrupole Mass Spectrometer**

Surface scattering of clusters off rigid plate generate abundance of fragmented clusters, these degraded clusters need a conventional way to determine the size distribution. In this study, a retractable detector for mass analysis is placed at about 1.9 m downstream the nozzle. This high-performance quadrupole analyzer mass spectrometer (QMS, Hiden HAL 3F) with 10 μs time resolution, 500 amu mass range, and single-ion counting capabilities allowing time-resolved scattering studies of neutral clusters with kinetic energies of 0.01–1 eV/molecule.

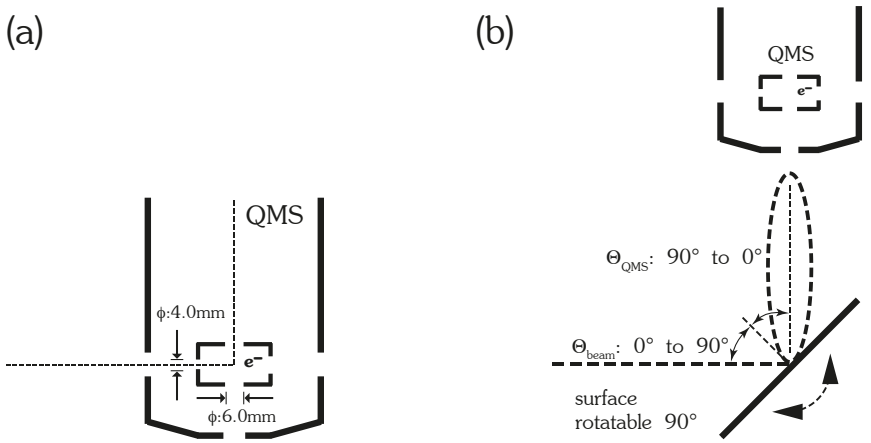

Figure 2.1-5 Sketches of the quadrupole mass spectrometer (QMS) as a cluster beam analyzer. (a) Directly place the QMS in the beam axis to analysis the mass over charge (m/z) information. (b) Measuring the angular distribution of scattered particles in the perpendicular direction of the beam by rotating the surface. When the surface is fixed, the QMS mounted on a linear translator offers a precise flight distance to precisely define the velocity.

A linear translator stage, TQ_y, provides the possibility to sample the incoming beam (target surface retracted) or to measure the velocity distribution of scattered particles. Note that, the sketch in Figure 2.1-5 shows the cross-beam electron gun can ionize the cluster by two different directions, the acceptance diameter of ionization cross-section from the side and bottom is 4.0 and 6.0 mm, respectively.

When the cluster beam is scattered off the $Si(111)/SiO_2$ surface in an 8×10^{-8} Pa UHV chamber, by rotating the surface holder, the angular information of the outgoing particles can be accessed according to the fixed angle ($\Theta_{beam} + \Theta_{QMS} = 90°$) from nozzle to QMS. In current setting of angular distribution measurements, the QMS records scattered particles with an acceptance angle of 5.4° in respect of the distance to the surface of 63.25 mm (along the beam-surface-detector plane or in-plane scattering). With constant voltage of 100 V of the filament, the electrical currents of 21 μA and 250 μA were applied to ionize the scattered CO_2 particles for m/z: 44 (monomer) and 88 (dimer) measurements, respectively. In addition, for another serious of experiments on sensitive helium clusters, the quadrupole mass analyzer probes the ion signal of fragmented helium clusters at m/z = 8, 12 and 16, wherein the voltage setting of filament for ionization is 40 V and the emission current is 250 μA.

2.1.3 Electronics

To record the time-of-flight spectra of either charged particles via MCP detector or neutral clusters via QMS, a highly precise timebase is required. The DG645 digital pulse-delay generator (Stanford Research Systems, Inc., USA) provides well-defined rubidium time-base with an accuracy of 1 ns and resolution of 5 ps. Consequently, all the instruments are synchronized by this fast "stopwatch". Start with the nozzle, the DG645 (Rb atomic clock) triggers the operational time of opening by a 20 μs long transistor–transistor logic (TTL) pulse.

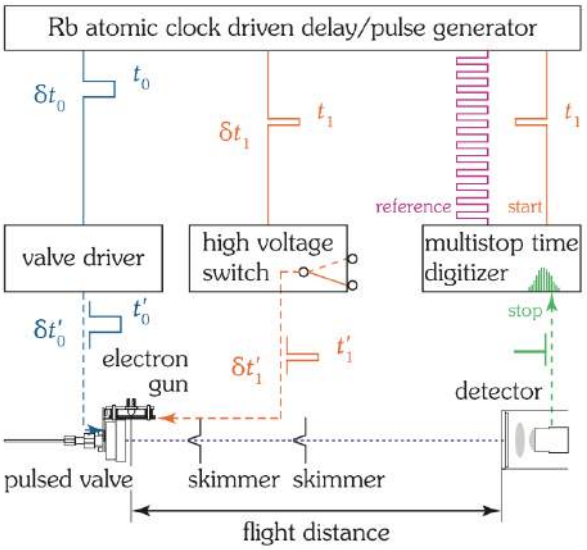

Figure 2.1-6 The regulation of short pulsed beam (starts at t_0', for δt_0' period), quick electronic excitation (starts at t_1', for δt_1' period) and time-resolved detection in current experimental setting, which is controlled by a multi I/O atomic clock.[50]

Whenever the electron source (e-gun) is needed for excitation/ionization, certain pulse delays on a precise time scale can be defined after the nozzle opening, see Figure 2.1-6. The respective electrode voltage of the e-gun is changed using a high-voltage push-pull switching unit (Behlke GHTS 30) with a turn-on jitter of 100 ps. Thus, optimizing this pulsed and focused e-gun allows efficient electronic excitation of pulse beam, which slices the expanded jet with ultra-short time resolution.

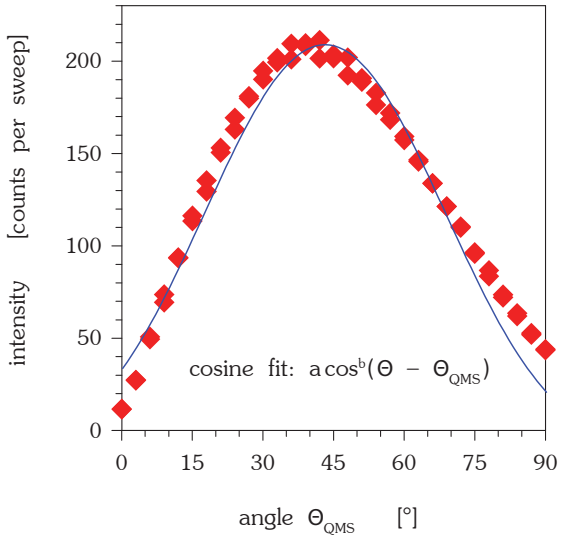

Figure 2.1-7 Nonlinear curve fit to the experimental angular distribution of scattered $(CO_2)_N$ beam off Si(111)/SiO_2 surface, where the source conditions of CO_2 beam are T_0 = 305.0 K and P_0 = 0.24 MPa. The resulting parameters Θ_{QMS} is 44.3° and the exponent term, b, is 2.4. Clearly, the angular distribution of scattered particles tends to the specular direction from the incoming beam and ends up with narrower spread rather than the "diffusive cosine round", which is assumed to be b = 1 and direct to the surface normal (0°).

For time-resolved ion counting by MCP detector, the DG645 can provide the start and stop signal to a 4 GHz multiple-event time digitizer P7887 (FAST ComTec, GmbH, Germany) with 250 ps time resolution. Note that power supplies NHQ (iseg Spezialelektronik, GmbH, Germany) provide the push-pull switches by virtually ripple-free (< 5 mV) high voltage, which can be optionally computer controlled and set within ± 40 mV.

2.1.4 Scattering Analysis

- **Cosine Law Scattering**

Since 1909, the Knudsen cosine law of scattering has been used to describe the evaporation, desorption and scattering of atoms/molecules from a rough surface.[61-65] This over 100-year-old concept has elevated the following research of gas dynamics, chemical bonding/dissociation and physical vaporization. Subsequent studies from Gaede, Epstein, and Clausing extend the cosine law to the general restitution process,[66-68] including scattering and reflection. Rideal has concluded that the second law of thermodynamics causes the cosine law of restitution.[69] Although the pure diffusive process shows the cosine pattern, the lack of kinetic data in scattering limits the development of molecular dynamics. Nevertheless, the extended cosine law with exponent term "$\cos^b\Theta$, $b > 1$" demonstrates the good spatial characterization of inelastic surface scattering.[70-72]

In this study, we applied surface scattering as a tool to analyze many weakly bonded $(CO_2)_N$ cluster beams, the resulting scattered particles have a lobular scattering structure. Because the reflected energy from the surface to the cluster may not simply undergo self-relaxation by changing the shape of cluster, which will result in solid clusters, the strong fragmentation of these van der Waals (VDW) clusters occurs just after the scattered beam has left the crystalline surface. As a result, the non-specular scattering with energy

loss by bond breaking process is assumed to produce the inelastic distribution. For all those scattering results from the current setup, as shown in Figure 2.1-7, we use the "$\cos^{b}\Theta_{QMS}$, $b > 1$" formula to evaluate the profile.

- ***In situ* Correction by the Geometry: Surface Positioning**

Before going into the detail of the evaluation of an angular distribution, one needs to be aware of the instrumental uncertainty of the geometrical placement of each device. With the current settings, the spatial relation of the incident beam to the scattering surface to the QMS detector defines the incoming/outgoing angle of the particles. Here we introduce a universal correction method of placing the scattering surface at the "right" position with the precision of sub-millimeter.

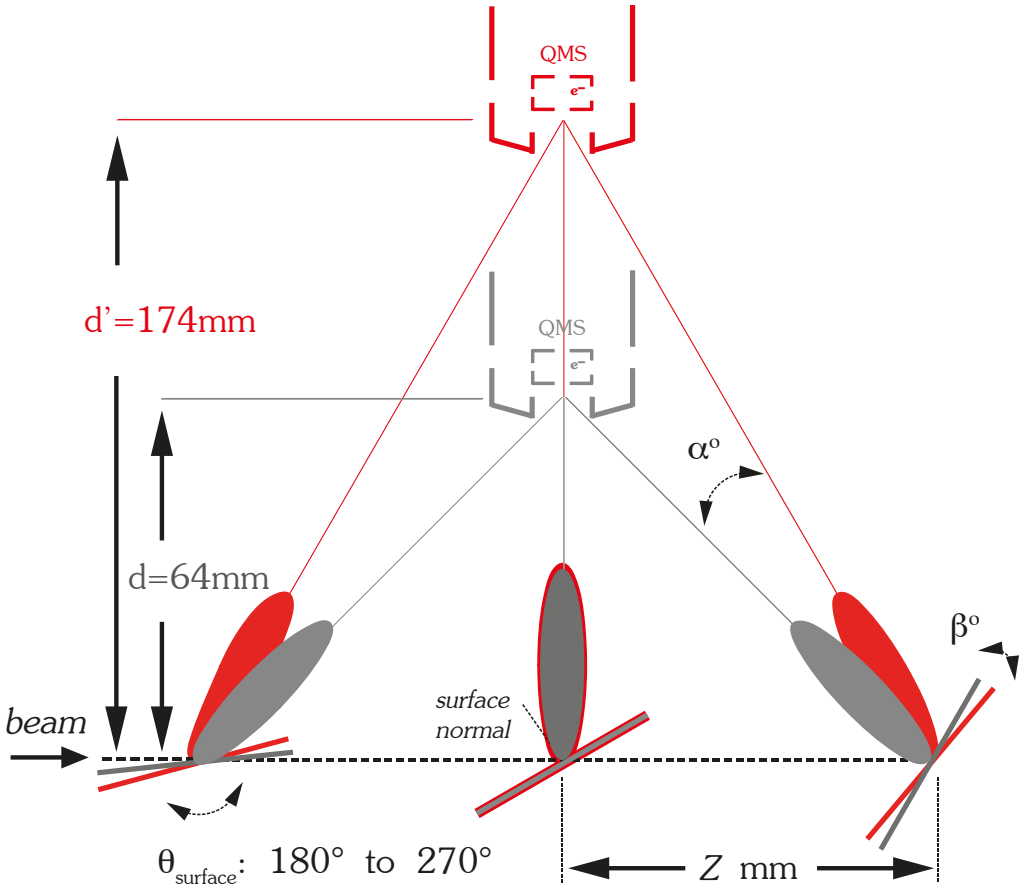

Figure 2.1-8 Geometric relation of surface positions to the detector positions. Here, the quadrupole mass spectrometer (QMS) is mounted on a linear translator and thus can be moved vertically perpendicular to the beam. On the other hand, the Si(111)/SiO_2 surface is mounted on a rotatable (360° in surface rotation angle, $\Theta_{surface}$) manipulator, which allows a linear translation on the beam axis. According to the predefined vertical line from two different QMS positions, only if the surface is precisely placed under the QMS, the $\Theta_{surface}$ is going to be identical (α or β = 0°) because both surface settings have to be rotated to reflect the incoming beam to the perpendicular direction. In other words, when the α or β from two surface settings is greater than 0° with respect to the two QMS positions, the surface is not considered just below the detector. This geometric relation helps to confine the surface position in z-axis to a sub-millimeter precision.

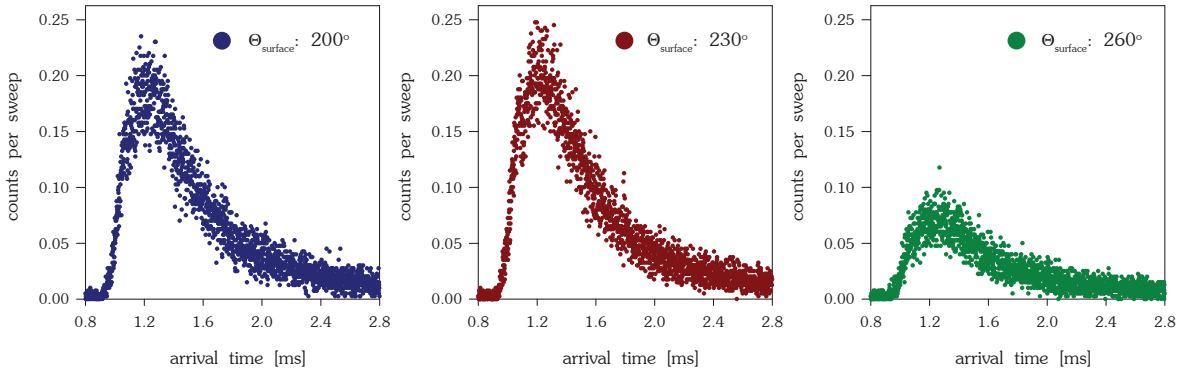

Figure 2.1-9 Scattering spectra of pulse helium beams scattered off Si(111)/SiO_2 surface. Three different angles of rotated surface were applied to deflect the incoming beam to the QMS detector: $\Theta_{surface}$ = 200°, 230° and 260°. The QMS detector probes the m/z: 4.0 signal for gaseous helium beam at the source conditions of T_0 = 319.0 K and P_0 = 1.20 MPa. Here, the *z*-position and *y*-position of the surface is 26.03(5) mm and 25.00(0) mm, respectively.

With the fixed beam source from the left side and impact to the surface, as shown in Figure 2.1-8, the surface mounted on a rotatable *xyz*-translator at first offers an opportunity to move along the beam axis (*z*-axis). While the surface is moved away from the theoretical downstream of the QMS detector, secondly, the surface must be rotated accordingly to reflect the beam to the detector. Followed by recording the rotated surface angles with respect to several positions of the surface with fixed detector (mounted on a linear translator stage with the position of TQ_y = 70 mm).

Experimentally, three model spectra from different angles of rotated surface at given *z*-position are depicted in Figure 2.1-9. The overall signal intensities from each spectrum were then collected by rotating the surface, see Figure 2.1-10. In the end, the maximum intensity with respect to the scattering angle ($\Theta_{surface}$) is defined, meaning that the surface has mostly reflected the incoming beam to the QMS.

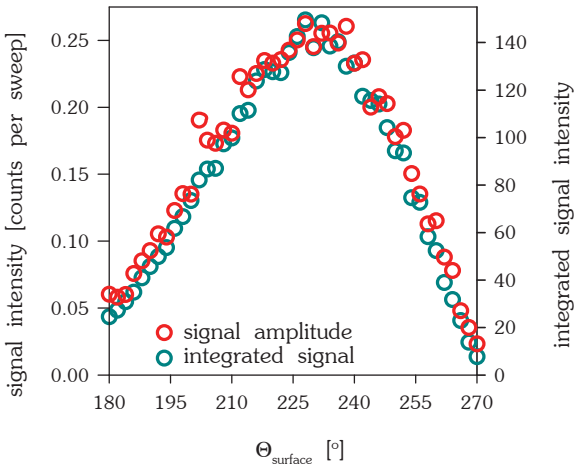

Figure 2.1-10 Illustration of scattered signal intensities compared to different angles of rotated surface. Both signal amplitude (red circle) and integrated signal (green circle) from the spectra in Figure 2.1-9 show a similar distribution. Therefore, at the angle of $\Theta_{surface}$= 230.11° (by numerical regression), the Si(111)/SiO_2 surface has mostly deflected the incoming helium beam to the QMS detector.

According to the analysis in Figure 2.1-11, these measurements show a roughly linear dependency of the angular shift against the surface *z*-position. Then, we repeat the measurements at these surface positions but with another detector position at TQ_y = 180 mm, which result in another linear trend. Both data sets were linearly regressed to two lines, they show a cross to preliminary define the *z*-position of the surface (TS_z) of 26.1 ± 1.6 mm. This cross *z*-position represents the indifferent setting of the surface angle just under the detector. Detailed model of this placement will be discussed later.

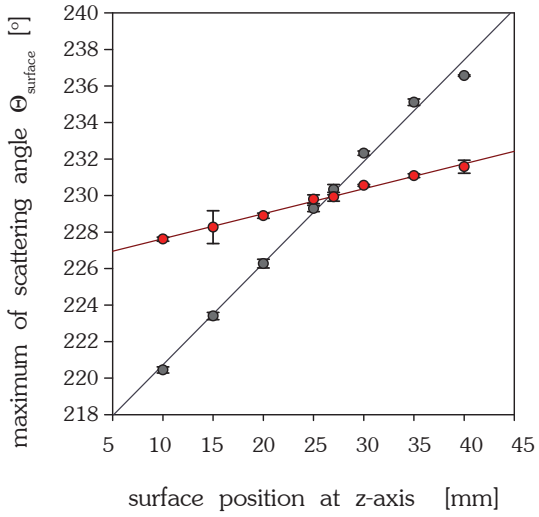

Figure 2.1-11 Linear dependency of the surface angle ($\Theta_{surface}$) along the z-axis. Each surface angle ($\Theta_{surface}$) is given by the maximum scattered particle intensity to QMS detector at different surface position. The gray dots are recorded when the QMS locates close to the surface (~ 64 mm above the central position of the surface) while all red dots are recorded when the QMS is far from the surface (~ 174 mm). Four measurements of full angular distribution in 4° step were taken according to each surface position. The linear regression depicts the continuous change of $\Theta_{surface}$ in order to reflect the incoming beam to the detector.[73]

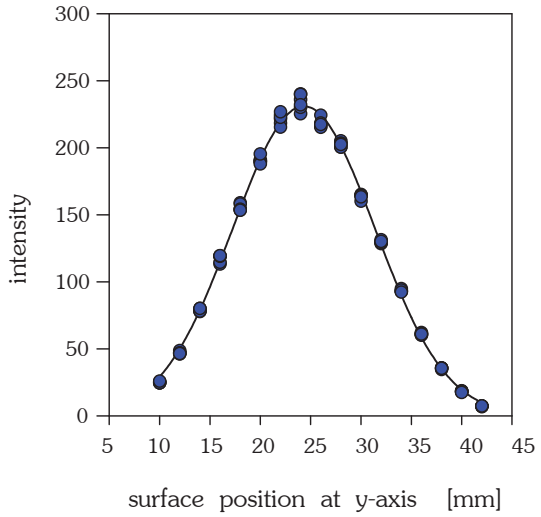

Figure 2.1-12 Reflected particle intensity from Si(111)/SiO_2 surface to the QMS along the y-axis. The crystal surface and the QMS detector are moved simultaneously to linearly scan the helium beam up or down. The maximum of scattered intensity is located at the surface position of TS_y = 24.3 ± 0.1 mm, which is numerically derived from a fitting function of normal (Gaussian) distribution.[73]

This defined *z*-position of the surface can be moved up or down along the *y*-axis (surface translator, TS_y) to probe the central line of the beam. Figure 2.1-12 depicts the relation between the recorded signal intensity from QMS detector and the *y*-position of the surface. When the central line of the beam meets the center of the surface, the maximum intensity of scattered beam appears at certain *y*-position. At this position, the rigid surface provides most efficient scattering and guides the outgoing beam to the detector.

It is worth mentioning, we kept the fixed distance between the surface and detector to cease the distortion of the detecting acceptance angle of QMS with respect to the central surface. In addition to aligning the surface to the central line of the beam, this Gaussian-like distribution in Figure 2.1-12 also shows the spread of the beam along the *y*-axis. This spread of the beam, standard deviation of ~ 4.1 ± 0.1 mm, affects the angular distribution of signal intensity, which should be considered during the data evaluation (in the next section).

Using the analogy of the auto correction process, the output *y*-position of the surface is thus fixed to scan and refine the *z*-position with higher precision. According to two different QMS detector positions, TQ_y = 70 (where the distance between QMS and surface is d = 64 mm) and 180 mm (where d' = 174 mm), six surface *z*-positions, including three ones right to the center and another three ones left to the center, were taken to record each angle of the rotated surface. The advanced evaluation at this second iteration is to compare the experimental data with a geometric relation. In Figure 2.1-13, the angle, α, based on two different distances between the QMS and surface, should follow this equation:

$$\alpha^\circ = \tan^{-1}\left(\frac{174}{z - z_c}\right) - \tan^{-1}\left(\frac{64}{z - z_c}\right). \qquad (2.1.1)$$

Here, z is the position of the surface and z_c represents the central position based on the geometry. This angle, α, is proportional to the difference angles of the rotated surface at given *z*-position, which is angle β. Experimentally, we take the absolute difference from two surface angles by recording the rotatable manipulator with an angular resolution of one degree. These data provide V-shaped dispersion in Figure 2.1-13 and can be perfectly described by the geometric relation:

$$\alpha^\circ \propto \beta^\circ = \gamma\left[\tan^{-1}\left(\frac{174}{z - z_c}\right) - \tan^{-1}\left(\frac{64}{z - z_c}\right)\right]. \qquad (2.1.2)$$

γ is the transforming factor. In view of the high accuracy of fitting quality of R^2 = 0.999, the model function precisely confines the surface *z*-position at TS_z = 25.9 ± 0.1 mm (but the translator only offers the step size as small as 0.05 mm). When we consider the stability of defining the maximum scattering intensity, the four rounds measurements gives up to 0.4° relative uncertainty from each angle, which should contribute to the uncertainty of ~ 0.1 mm for the surface *z*-position. Herein, the outcome of surface positioning provides the orthogonal geometry of ∠beam–surface–detector = 90°, which is essential to derive the incoming/outgoing angle of the beams.

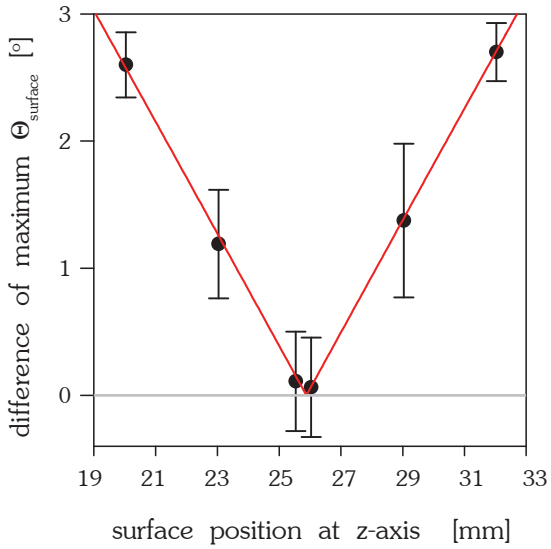

Figure 2.1-13 According to the geometric relation, the difference of two surface angle ($\Theta_{surface}$) with respect to two QMS positions has a "0" point when the surface is exactly located under the QMS. The black dots contain 4 rounds of $\Theta_{surface}$ scanning for different surface *z*-positions as well as QMS *y*-positions.[73] On the other hand, the red line represents the numerical fit of the geometric model Eq. 2.1.2 to the experimental results. This result suggests a surface *z*-position at $TS_z = 25.9 \pm 0.1$ mm with a fitting quality of $R^2 = 0.9998$ including the error bars.

- **Model: Conservative of Parallel Velocity**

When the position of the surface is precisely defined, by rotating the surface holder, the angular information of the outgoing particles can be accessed according to the fixed angle ($\angle$ beam–surface–detector = $\Theta_{beam} + \Theta_{QMS} = 90°$) from nozzle to QMS, see Figure 2.1-14. Whenever the incident angle (Θ_{beam}) of cluster beam is increasing, the complementary detection angle (Θ_{QMS}) is decreasing, accordingly. In current setting, the scattered particles will travel ~ 64 mm to the QMS's ionization zone from the bottom after leaving the surface, which represents an acceptance angle of 5.4° in respect of the surface center (along the beam-surface-detector plane) for given spectrum.

As this experimental setting requires continuously rotating the surface holder for data acquisition, which should be differentiated from another type of instrument with fixed incident beam and rotatable detector. To rationalize the intensity versus the complementary detection angle (Θ_{QMS}), preceding simulation is thus helpful to clarify the scattering concept.

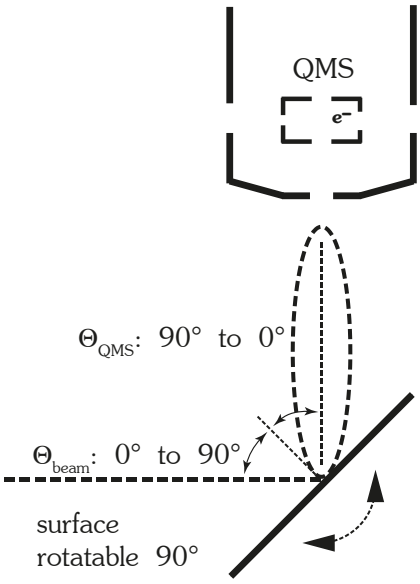

Figure 2.1-14 Schematic plot of surface scattering experiment in current study, where the beam and QMS detector are fixed and the surface is rotatable, which results a correlation of ∠beam–surface–detector = $\Theta_{beam} + \Theta_{QMS} = 90°$. The incoming beam from the left side will be reflected and turn to the QMS. Thus, the angular distribution of the scattered beam can be recorded by rotating the surface and collecting the Θ_{QMS} from 0° – 90° (reference to the surface normal). Here, the distance between surface center and the QMS in this study, if, not specified, is ~ 64 mm.

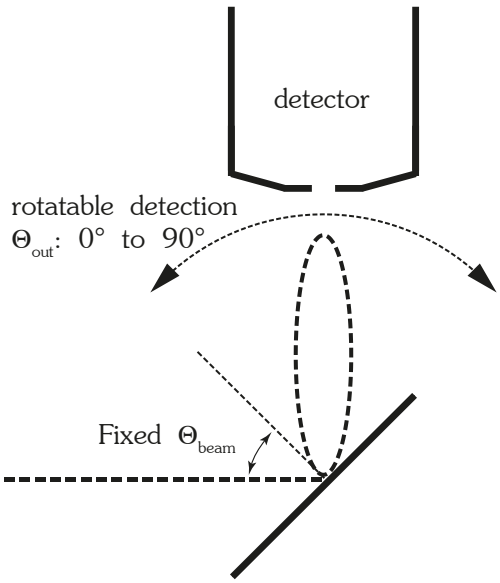

Figure 2.1-15 Schematic plot of surface scattering experiment in some other groups,[74-84] where the beam and surface are fixed and the detector is rotatable. The incoming beam from the left side will be reflected and turn to the QMS in different angles, which result in $\Theta_{out} = 0° – 90°$.

For the trapping desorption channel, those trapped clusters on the surface will continuously evaporate along the surface normal. The diffusing as cosine distribution will be recorded from different detection angle (Θ_{QMS}) and unrelated to the incoming beam. When the elastic scattering of atomic/molecular beam or the inelastic scattering of molecular/cluster

beam left a rigid surface, on the other hand, the surface scattering coefficient (ε) is sued to describe the change in direction. It can be defined equally to 1 or smaller than 1 to correlate the outgoing direction (Θ_{out}) of the beam to the oriented incoming beam (Θ_{beam}), respectively. Thus, we determined the correlation by using

$$I_{\mathrm{out}} = \cos^n(\Theta_{out}) = \cos^n\left(\tan^{-1}\left(\frac{\tan\Theta_{\mathrm{beam}}}{\varepsilon}\right)\right). \qquad (2.1.3)$$

Θ_{out} is the predicted scattered beam direction. Experimentally, the Θ_{out} reveals the maximum of signal intensity over the whole range of scattering angles, as shown in Figure 2.1-15. Nevertheless, in current experimental setting, the detection angle Θ_{QMS} is fixed with respect to one specific incoming beam (Θ_{beam}). By applying the cosine law of scattering, the signal intensity (I_{QMS}) recorded at Θ_{QMS} can be expressed as

$$I_{\mathrm{QMS}} = \cos^n\left(\Theta_{out} - \Theta_{QMS}\right) = \cos^n\left(\tan^{-1}\left(\frac{\tan\Theta_{\mathrm{beam}}}{\varepsilon}\right) - \Theta_{QMS}\right), \qquad (2.1.4)$$

where the n is an exponent term depended on the spread of spatial expansion of the scattered particles. To simplify and distinguish from diffusive desorption along the surface normal (n = 1), we simulate the imitation signal distribution as n = 2. The results of ε from 1 to 0.25 versus the different detection angle (Θ_{QMS}) and the outgoing angle (Θ_{out}) can be compared in Figure 2.1-16. If necessary, this outgoing angle (Θ_{out}) can still be simulated by different orientation of the beams, but the output phenomena won't disrupt the tendency as the ε changing continuously.

Clearly, both of the maximum signals shift toward larger angle while the ε decreases. When the scattered beam gets closer to the surface, as described in the literature, the larger mean cluster size of the incoming beam is predicted even for the incident cluster beams with weekly bounded.[37,41,85] In short, the increase of Θ_{QMS} indicates the larger mean cluster size of the incoming beam.

In earlier studies, the scattering coefficient (ε) of cluster beams was reported to be changed especially at boundary angles either vertical impact (Θ_{beam}= 0°) or parallel (Θ_{beam}= 90°) to the surface. Therefore, to avoid the uncertainty caused by these cases, this thesis only reports the angular dependence of scattered particles but rather specify the absolute scattering angles from any fixed incoming beams in the following discussions.

- **Correction of Scattering Angle While Rotating the Surface**

Take helium beam for example, which performs the surface scattering of atoms regardless the dissociation of bond. The angular distribution of scattered particles (m/z: 4) is plotted according to the detecting angle (Θ_{QMS} = 0° – 90°) at source condition of T_0 = 319.0 K and P_0 = 9.60 MPa, see Figure 2.1-17. The hill-shaped profile was first fitted by single cosine function with exponent term

$$I_{QMS} = w \times \cos^n(\Theta - \Theta_{QMS}) \,. \qquad (2.1.5)$$

In this formula, parameter w is the scaling factor, and parameter n is the angular spread indicator. Resulting symmetric curve is centered at Θ_{QMS} = 44° with the cosine exponent of 5.3. This preliminary result shows a narrow scattering structure, which is clearly different

from the broad trapping-desorption process along the surface normal. Although the R-squared value (R^2) is 0.994 by the least squares fitting, the inherent asymmetry still needs to be discussed.

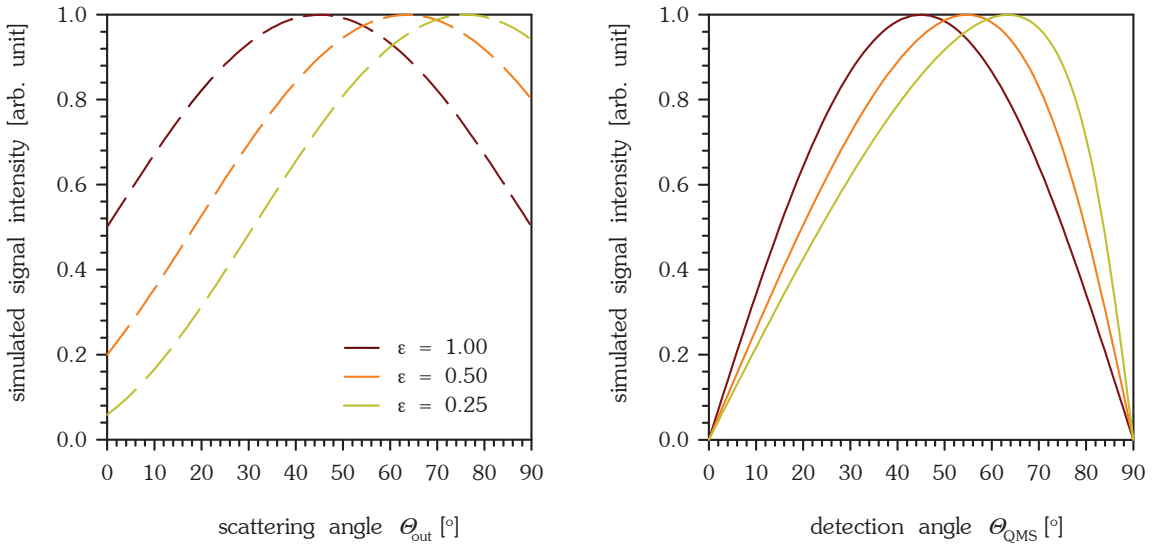

Figure 2.1-16 (*left*) Simulated signal as a function of scattering angle (Θ_{out}) based on the fixed incident beam of Θ_{beam} = 45° in Figure 2.1-17, where the signal intensities are calculated by Eq. 2.1.3 according to three different scattering coefficients (ε). (*right*) Simulated signal intensity for three different scattering coefficients based on Eq. 2.1.4. The detection angle (Θ_{QMS}) changes with respect to different incident angles (Θ_{beam}= 0° – 90°), see Figure 2.1-12. Comparing to these two experimental settings, both resulting angles (Θ_{out} and Θ_{QMS}) show the same increasing trend when ε is getting smaller.

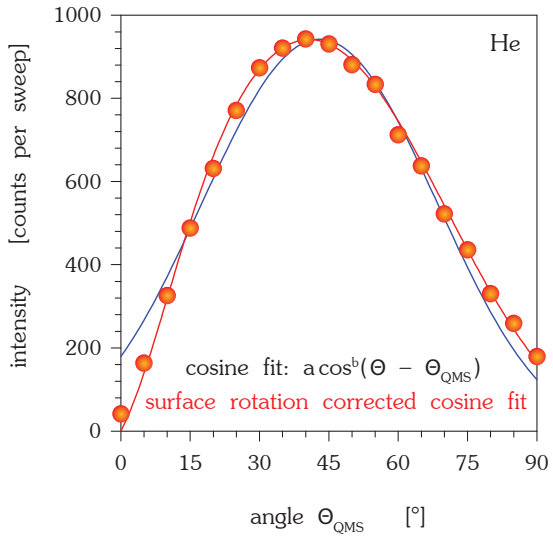

Figure 2.1-17 An angular distribution of He^+: m/z = 4.0 from pulsed atomic helium beam scattered off Si(111)/SiO_2 surface. The dark blue line is directly fitted by the cosine function with exponent term, which yields a fitting quality of R^2 = 0.94. When the geometric relation between the beam and rotated surface is further considered, meaning that the symmetric cosine with exponent term has to further multiply a correction factor by Eq. 2.1.6, the resulting red asymmetric fitting curve gives a reasonable good fitting quality of R^2 = 0.997. Here, the source conditions of helium beam are T_0 = 319.0 K and P_0 = 9.60 MPa, and the crystal surface is rotated in 5° step.

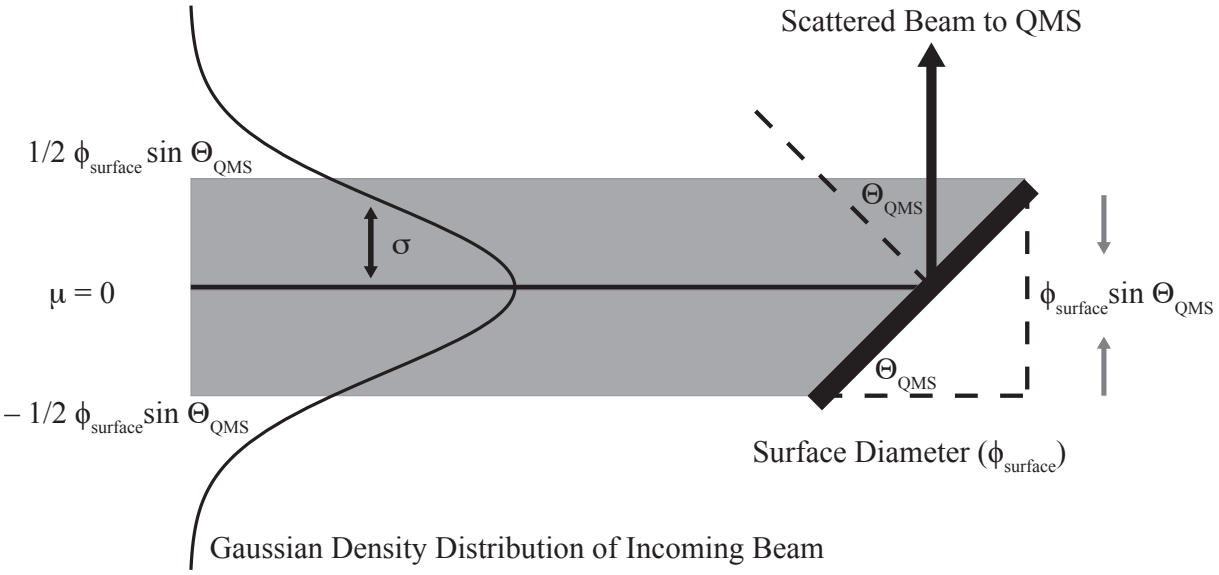

Figure 2.1-18 Schematic relation of effective scattering region from a rotated surface to an incident beam with normally distributed density. The gray effective region is determined by the projected diameter of a crystal surface ($\phi_{surface}\sin\Theta_{QMS}$) and the vertical spread (proportional to σ) of the incident beam. When the surface lies parallel to the central line of the beam, no incident particle is assumed to collide the crystal surface. Thus, the correction factor gives 0 % in scattering probability if the surface is rotated to the incident angle of 90°, where the detection angle is $\Theta_{QMS} = 0°$. On the other hand, whenever the projected diameter of a crystal surface ($\phi_{surface}\sin\Theta_{QMS}$) is greater than the vertical spread of an incident beam, the scattering probability is 100% of the incident particles.

In Figure 2.1-18, when the surface is rotating, the effective impact area to the incoming beam is also changing. Assuming a Gaussian-like beam profile in the vertical direction with certain spread of σ = 2.0 mm, even the circular surface's diameter is $\phi_{surface}$ = 20.0 mm, most of the beam will not impact the surface if the surface lies down along the beam axis. That is to say, the cosine fitting should be modified with respect to different surface rotating angle by a scaling factor.

Figure 2.1-19 shows the projected two-dimensional effective region of a surface, which can be calculated to cover the effective height of $\phi_{surface} \times \sin\Theta_{QMS}$ at the vertical direction. The correction factor is calculated using an integrated possibility distribution function of a normal distribution as

$$Correction\ Factor(\Theta_{QMS}) = \int_{-\frac{1}{2}\phi_{surface}\sin\Theta_{QMS}}^{\frac{1}{2}\phi_{surface}\sin\Theta_{QMS}} \frac{1}{\sigma\sqrt{2\pi}} e^{-\frac{(x-\mu)^2}{2\sigma^2}} dx, \qquad (2.1.6)$$

where the estimated spread of σ = 2.0 mm and the predefined central position of the surface is μ = 0 mm. Then, this correction factor can be used to represent the percentage of a Gaussian-like beam interacted to the corresponding surface.

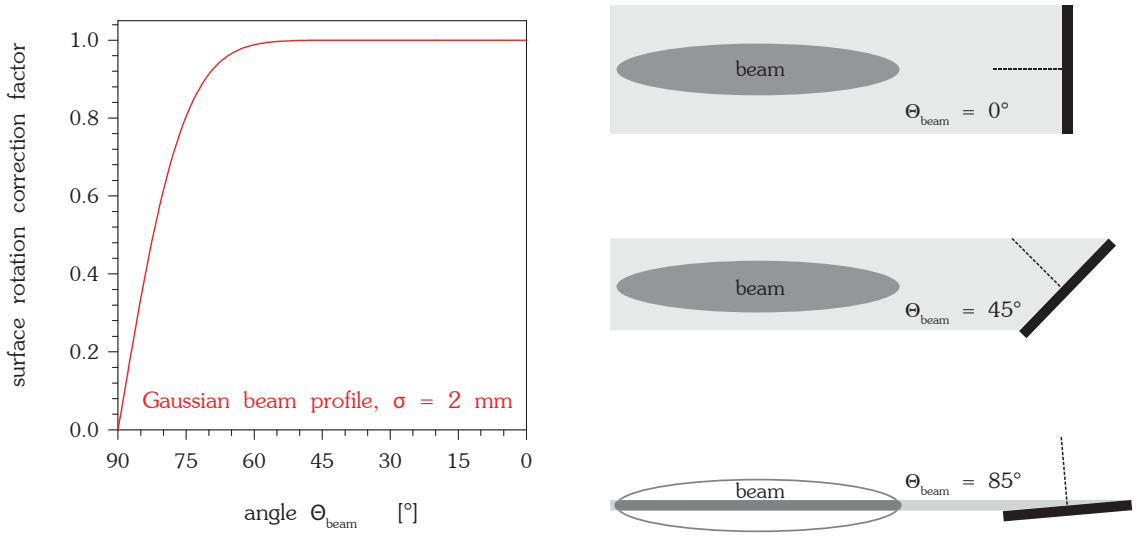

Figure 2.1-19 The correction factor for the Gaussian-like beam (with σ = 2.0 mm) to the crystal surface with a diameter of $\phi_{surface}$ = 20 mm. Depicted graph on the right side visualizes the effective portion from three different surface settings.

As depicted in Figure 2.1-17, the final fitting is based on the cosine function with exponent term and multiplied by the expected density probability of an incoming beam. After the correction, the Θ_{QMS} is 41.4° and the exponent term is 4.2 after correction with the $R^2 > 0.999$, which is better than the previous result. It is worth to mention that the trapping-desorption behavior of a cosine round along the surface normal can also be simulated in combined with the correction factor of current instrument in Figure 2.1-20, which yields a maximum intensity located at ~ 24.0°. In short, this consideration of surface geometry improves the accuracy of describing the scattered particles for current experimental setting.

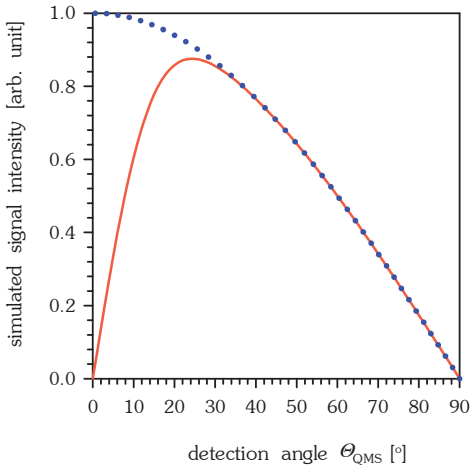

Figure 2.1-20 Illustration of trapping-desorption channel along the surface normal (Θ_{QMS} = 0°). The blue dots are plotted by the simulated signal intensity for the QMS detector. When this simulation is further scaled by the correction factor, as mentioned earlier, the red line represents the angular distribution of desorbed particles from the surface. The maximum signal of the detecting angle is calculated to be $\Theta_{QMS} \approx 24.0°$.

- **Fitting Condition**

In addition to all the R-squared (R^2) values by least squares fitting of angular distributions, in this study, whole numerical fittings are further verified by the statistical test to avoid the over-fitting. The unnecessary free parameter may lead to wrong interpretation during data evaluation. Therefore, the extra fitting function is added only if all the included parameters are passing the *t*-test, which is set at the p-value below 0.001 (one-tailed, d*f* = 31, this degree of freedom is rationalized by the experimental 3° interval over 90° range).

2.2 Basic Principles

2.2.1 The Molecular Beam

Molecular beam is an extermely useful tool to generate and study particles for their physical properties and chemical dynamics.[77,86-96] To precisely determine these properties, an ultra-high vacuum environment is required to reduce the interaction between particles in the beam and the residual gas in the chamber. Consequently, the large gradient between a high-pressure source of molecules and the vacuum chamber accelerates the jet expansion through a nozzle. Based on the different type of nozzles, the resulting jets can be separated into two categories: effusive beams and supersonic beams.

An effusive beam is commonly formed through a capillary pipe, where the orifice diameter (d) is an important factor of the beam. In order to reduce the collisions between expanded molecules in the beam, the exit diameter, d, is designed to be smaller than the mean free path (λ_0) of the atoms/molecules inside the beam source. Those expanded atoms/molecules result in a velocity weighted Boltzmann distribution according to the source temperature of the beam. The overall most probable velocity of the particles in an effusive beam is commonly between 10^2 – 10^3 m/s from a room-temperature reservoir. At the end, by confining the source temperature and pressure, the distribution over the internal degrees of freedom of the molecules (rotation, vibration) in the effusive beam is also the same as that in the reservoir.

When the source pressure is raised or the nozzle diameter is reduced (normally with converging shape), the λ_0 may be smaller than d. In the case that d is much larger than λ_0, the strong collision of expanded particles causes adiabatic cooling of all degrees of freedom in the vicinity of the nozzle exit. For these molecules, the total energy available per molecule in the container is converted into kinetic energy (translational movement), leading to an accelerated beam. The terminal velocity (v) of such beams is thus above the local speed of sound $c = \sqrt{\gamma RT/m}$, where γ is the heat capacity ratio and m is the mass of a single molecule in kilograms, named supersonic beam. Another index uses the particle velocity divided by the local speed of sound, the Mach number ($M = v/c$), which is greater than 1 for a supersonic beam.

Concerning the efficient cooling during the expansion, the cooled degrees of freedom (translational, rotational, and vibrational) of the molecules provides sharp spectral lines for optical analysis. For noble gas expansions, especially pure atomic beams, a translational temperature below 1 K can be easily obtained. In the real gas system, on the other hand, the terminal temperature in the beam is often limited by clustering. These two research orientations have led the cold molecule and nucleation theory for few decades.

2.2.2 Time-of-Flight Spectrum

Time-of-flight spectrum recorded by either MCP detector or QMS represents the terminal particle distribution within a particular time window. The arrival time of each particle reflects the coupling of speed and travel distance. Thus, a defined distance allows us to calculate the velocity by the arrival time of given particle. In the pulsed molecular beam

system, the arriving particles often distribute in a certain time range. In general, the mean arrival time and the arrival time in maximum intensity of all particles are taken to derive the average speed ($\langle v \rangle$) and the most probable speed (v_p), respectively. Because these velocities of particles are essential to calculate their kinetic energies, the precise measurement of arrival time as well as the analysis method is the key to achieving the goal.

Concerning to the detection, the sufficiently energetic photons and particles can be recorded as a function of time. Later, the signal is digitized to data in the computer with short intervals of equal time period. This interval length, however, is normally short enough to be disregarded. One of the paramount factors affecting the precision is the initial pulse duration of the supersonic beam, which contributes to the width, δt, of the arrival time distribution. Consequently, the scatter of arrival times in each pulse defines the precision of mean arrival time, $\langle t \rangle$. The random error in the estimate of the $\langle t \rangle$ is given by the standard deviation of the centroid, σ_c, and is independent of the peak shape:[97]

$$\sigma_c = \frac{\delta t}{\sqrt{N}}. \qquad (2.2.1)$$

Here N is the number of measurements contributing to the peak, δt is the standard deviation. When narrow distributions are repeated by many measurements, the uncertainty in the estimated peak position is diminished. Although the contribution of the initial pulse duration to the measured width of the time-of-flight spectrum can be considered numerically, particle sources with pulse widths as short as possible are advantageous because the process of de-convolution is not lossless. Thus, we use electronic tagging to ensure the pulse duration is much shorter than the fastest mechanical pulsed valves by more than one order of magnitude.

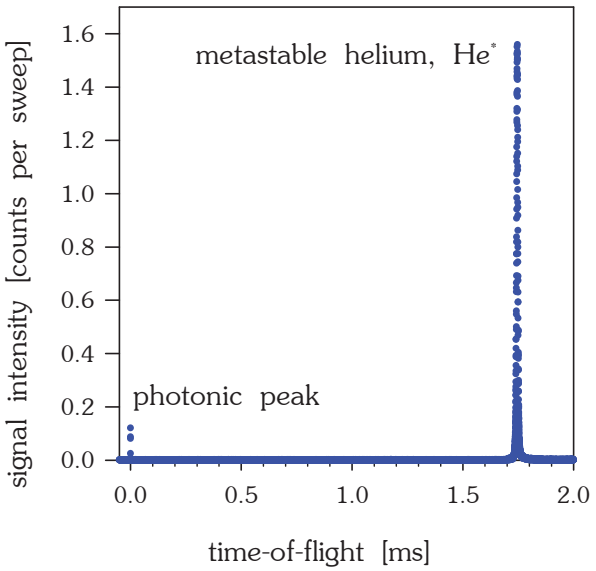

Figure 2.2-1 Time-of-flight spectrum for an electronically tagged helium beam at source conditions of P_0 = 9.60 MPa and T_0 = 319.0 K. The ultra-fast electronic excitation is 300 ns long with the electron energy of 140 eV. This excitation is chosen to tag the pulsed helium at 90 μs after the nozzle opening, t_0. Here, the tiny early photonic peak is attributed to the quick ultraviolet quenching after the electronic excitation while the later and larger signal belongs to the highly energetic metastable helium.

Employing accurate electronic system to prompt the nozzle and record the data from different detectors with finite resolution, the experimental procedure should provide sufficient signal intensity with high stability and reproducibility allowing for data analysis. Zero-assumption statistics and nonlinear curve fitting were both applied to ensure the accuracy of given condition of a pulsed jet.

- **Robust Statistics: Median, Interquartile Range**

Figure 2.2-1 displays an arrival time spectra of an electronically tagged helium beam at source conditions of P_0 = 9.60 MPa and T_0 = 319.0 K at the excitation delay of 90 μs referenced to the nozzle opening time, t_0. When we select the region of metastable helium peak, this signal distribution can be analyzed by signal amplitude, integrated intensity, mean arrival time, peak width and peak shape. A robust and model-free statistical data evaluation[98] is used to avoid possible artifacts from fitting procedures. Therefore, we can apply the statistical median to represent arrival time and the interquartile range (IQR) to characterize peak width. The interquartile range is defined as IQR = $P_{75} - P_{25}$ (P_n is the n^{th} percentile, $0 \leq P \leq 100$) for a rather robust measure.

For some systematic experiments, the identical procedure of data acquisition cannot apply to each individual condition, e.g., helium source pressure of P_0 = 9.60 MPa at T_0 = 319.0 K results different arrival time and signal intensity of detected particles compared to the same source pressure at another T_0 = 410.0 K. We then use the probability distribution model to fit the detected signal, which allows to independently evaluate the signal amplitude, overall intensity, mean arrival time, peak width, peak shape, etc. regardless the count statistics of signal. Based on the different working fluids, the ideal gas like helium beam requires symmetric peak function while the CO_2 beam requires asymmetric distribution function because of the clustering during jet expansion.

- **Central Moment: Estimation of Fitting Functions**

Generally, the fitting procedures require estimating population parameters from sample statistics such as maximum likelihood, least squares, and method of moments. These results from different methods yield consistent estimation of the uncertainties incorporated in entire data analysis. For instance, the first moment represents the weighted average of the sample distribution. This mathematical average can be used to describe the expectation of the mean arrival time, $\langle t \rangle$. In current data evaluation from our experiments of helium beams by MCP detector, the difference between mean and median of all TOF spectra is less than 210 ns. Then, the second central moment gives a measure of peak width as the variance, σ^2. Concerning to the asymmetry of a probability distribution, the third central moment displays a measure of skewness, which can be evaluated as:

$$m_3 = \frac{\sum_{i=1}^{n} y_i (t_1 - \bar{t})^3}{\sum_{i=1}^{n} y_i} . \qquad (2.2.2)$$

where n denotes the number of counting intervals, y_i the number of counts in interval i, and $\bar{t}$ the sample mean. Figure 2.2-2 shows numeric values of standardized central moments, and a least-squares fit of Student's t distribution. When the skewness is rather small, this evidence suggests a highly symmetric distribution for data fitting.

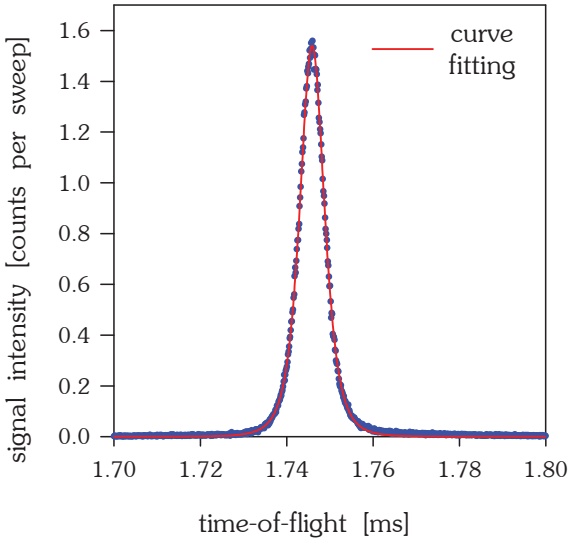

Figure 2.2-2 A zoom-in graph for the metastable helium in Figure 2.2-1. The statistic result from this spectrum gives a median of 1.7463 ms and a skewness of – 0.03. For a fitting result, Student's t distribution with least-squared method gives the mean arrival time of 1.7478 ms and a standard deviation of 3.246 μs.[98]

- **Symmetric Distribution: Gaussian, Lorentzian and Student's *t* Distributions**

For example, Figure 2.2-2 shows a typical metastable helium (He^*) peak shape with the skewness close to zero (–0.03), which is fitted by a Student's t distribution with least-squared method. The overall fitting quality R^2 from this Student's t distribution is greater than 0.999 with background subtraction. Normally, one would preliminary use a normal (or Gaussian) distribution to fit a symmetric distribution of data with the time scale (t):

$$f(t,a,b)\,dt = \frac{1}{\sqrt{2\pi}b} exp\left[-\frac{1}{2}\left(\frac{t-a}{b}\right)^2\right] dt\,, \qquad (2.2.3)$$

where a is the position parameter and b is the scaling parameter of width. In other word, the mean arrival time $\langle t \rangle$ is given by a and the full width of half maxima (FWHM) of the peak can be determined by $\delta t = 2(2\ \ln\ 2)^{1/2}b$. Or, some related works have also used a Lorentzian (or Cauchy) distribution,

$$f(t,a,b)\,dt = \frac{b}{\pi[(t-a)^2 + b^2]}\,dt\,, \qquad (2.2.4)$$

to describe the data points. This probability density function with Lorentzian line shape demonstrates a homogeneous broadening in optical spectroscopy while the inhomogeneous broadening shows a Gaussian profile. The difference between these two functions is that the Lorentzian distribution describes the broader wings of given peak better than the Gaussian distribution. Since the high-density helium jet expansions have no physical

justification for applying one of these two functions, a mathematical solution of Student *t* probability distribution,

$$f(t,a,b,c)\,dt = \frac{\Gamma\left(\frac{c+1}{2}\right)}{\sqrt{c\pi}b\Gamma\left(\frac{c}{2}\right)}\left[1+\frac{(t-a)^2}{(cb^2)}\right]^{-\frac{c+1}{2}} dt\,, \qquad (2.2.5)$$

is an ideal function to take place. Because the parameter *c* in this non-central Student's t function offers the transformation from a Lorentzian distribution to a Gaussian distribution, when *c* changes from 1 to ∞. It is worth to mention that the mean arrival time $\langle t \rangle$ is given by the analytic solution of *a*, but the *c* must be greater than 1 otherwise the mean of this probability density function of student's t distribution could not be defined.

- **Asymmetric Distribution: Maxwell–Boltzmann Distribution**

An ionized carbon dioxide cluster $(CO_2)_N^+$ peak shape in Figure 2.2-3 shows the asymmetric arrival time distribution, which is fitted by a Maxwell–Boltzmann distribution. Normally, the velocity distribution of particles in supersonic molecular beam is assumed to be a three-dimensional Maxwell distribution.[99] This distribution relates to the mean flow velocity, v_1, and a local beam temperature, T_1. For the parallel velocity along the expansion axis, *v*, the function can be expressed as:

$$f(v,l,T_1,v_1)\,dv \propto \frac{1}{l^2\pi^{\frac{3}{2}}}\left(\frac{m}{2k_BT_1}\right)^{\frac{3}{2}} v^3 exp\left[-\frac{m}{2k_BT_1}(v-v_1)^2\right] dv \qquad (2.2.6)$$

or

$$f(v,l,\Delta v,v_1)\,dv \propto \frac{1}{l^2\pi^{\frac{3}{2}}}\left(\frac{v}{\Delta v}\right)^3 exp\left[-\left(\frac{v-v_1}{\Delta v}\right)^2\right] dv\,, \qquad (2.2.7)$$

where *l* is the total field-free flight distance of particles, the Δ*v* represents the width of the peak, *m* is the molecular mass, and k_B is the Boltzmann constant. For experimental data, the function is transformed to a flight-time (*t*) domain distribution for a flux sensitive detection:

$$f(t,t_F,d)\,dt = d\frac{l^3}{(t-t_F)^4} exp\left[-\left(\frac{l/(t-t_F)-v_1}{\Delta v}\right)^2\right] dt\,, \qquad (2.2.8)$$

parameter *d* gives a scale factor related to the signal intensity along the expansion axis. Here, the mean arrival time ⟨t⟩ is given by t_F.

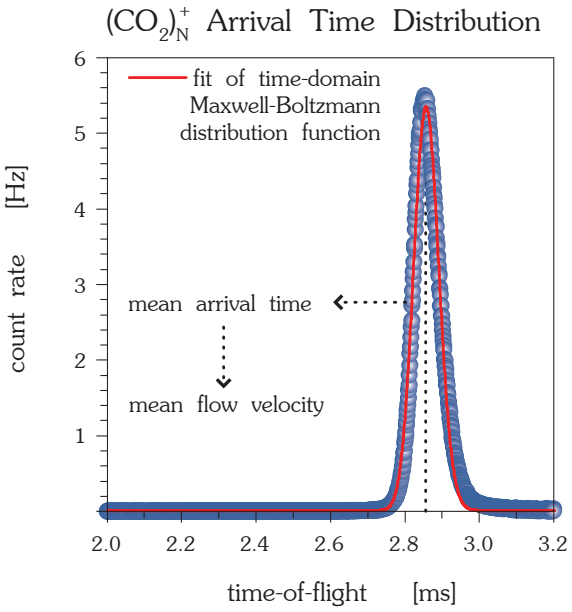

Figure 2.2-3 A typical time-of-flight spectrum of ionized $(CO_2)_N^+$ beam, which is fitted by a Maxwell-Boltzmann distribution. The beam was originally ionized by an electron source for 2.5 μs near the exit of the nozzle. The fitted mean arrival time can be converted to the mean flow velocity according to the flight distance.

2.2.3 Cluster Size Distribution

In the real gas system, the particles expanded to the vacuum not only result in translational movement with velocity distribution of individual particles, but also condense via strong cooling at the early stage. The source pressure and temperature define the initial density of these particles and subsequently affect the collision probability during the expansion. For rare gas, the aggregated atoms by van der Waals (VDW) force from atomic clusters, where the potential between each atom can be described by a Lennard-Jones formula with the interaction potential

$$V_{L-J}(r) = \varepsilon_d \left[\left(\frac{r}{r_0} \right)^{-12} - \left(\frac{r}{r_0} \right)^{-6} \right]. \qquad (2.2.9)$$

The ε_d is the depth of the potential well at the equilibrium inter molecular distance at $r = r_0$; inside of the square brackets, the first term responses to the repulsion of the filled orbitals from each particle at short distance, while the second term represents the long-range dispersion force between two induced dipoles. On the other hand, for molecular clusters, the stronger interactions include dispersion interactions, VDW forces, dipole-dipole interactions, induction forces, and hydrogen bonding… *etc.* allows molecules to construct larger clusters.

- **Clusters from Condensation of Gases: Hagena's Scaling Law**

To control the size distribution of clusters by a continuous jet expansion, Hagena's empirical scaling law expresses the effect as a function of source geometry, source

temperature and source pressure.[18,100-102] This scaling function has been widely used to estimate the size distribution based on the nucleation process, which includes:

$$\langle N \rangle = A\left(\frac{\Gamma^*}{1000}\right)^m, \qquad (2.2.10)$$

$$\Gamma^* = k d_{eq}^q P_0 T_0^{sq-(\frac{f}{2}+1)}, \qquad (2.2.11)$$

$$d_{eq} = \frac{f(\gamma) d}{\tan(\alpha)}. \qquad (2.2.12)$$

Here, $\langle N \rangle$ is the average number of atoms per cluster, A relies on the second dimension-less gas specific constant and m is a scaling parameter determined experimentally. For the second equation, Γ* is the condensation parameter, which includes: k the gas specific constant, P_0 the source pressure, T_0 the source temperature, d_{eq} the throat nozzle diameter which is approximated by the conical shape and the exponent term, q, is gas-specific constant parameter determined experimentally and s is defined by the number of thermally active degrees of freedom f as $s = (f - 2)/4$. In the additional formula for the nozzle, $f(\gamma)$ is a parameter as a function of the ratio of the heat capacity (0.736 for monatomic gas, 0.866 for diatomic gas or linear molecular and 0.933 for other molecular system[103,104]), d is the diameter of the nozzle exit and α the half-opening angle of the conical nozzle. In this study, according to the geometry of trumped nozzle, the half opening angle is approximated to 8°. As a result, when the beam starts at low density as gas expansion, at given geometry of nozzle, the clusters were aggregated proportional to the square root of number of particles in the beam, meaning that the terminal size of clusters can be referred to the source density.

- **Clusters from Liquid Expansion**

On the other hand, Henne *et al.* present another size distribution model of the clusters via liquid jet expansion.[105] These clusters are fragmented from large droplets, which thus links to the surface tension of droplets and also the size of a nozzle exit

$$\langle N \rangle = \frac{80\pi}{3}\frac{s}{m_s}\left(\frac{d}{a}\right)^2. \qquad (2.2.13)$$

The $\langle N \rangle$ represents the average number of atoms per cluster, s is the surface tension, m_s is the molecular mass, d is the diameter of the nozzle and a is the sound speed at the throat of the nozzle. That is to say, the formation channel of clusters, either condensation from the gas phase or fragmentation of a liquid phase, defines different size distribution and thus should be identified to improve the prediction of cluster growth. Therefore, the presented studies cover comprehensive source conditions from gas to supercritical to liquid jet expansions, which generate clusters from few hundred up to sub-million molecules. These clusters can be successfully separated to two formation channels by time-resolved surface scattering methods.

CHAPTER 3

3 Characteristics of Dense Supersonic Jets

Dedicated research of supersonic cluster beams requires the source conditions to be well understood. Here, we start with a model system of a pulsed supersonic helium expansion, aiming to advance the experimental method for the generation of cold particle bunches and the highly accurate determination of their velocities. For any adiabatic expansion process, from a macroscopic point of view, the conservation of total energy for a free jet expansion of a fluid system into a vacuum can be described by the following:[106]

$$E = U_0 + P_0V_0 + \frac{N_A m {v_0}^2}{2} = U_1 + P_1V_1 + \frac{N_A m {v_1}^2}{2}. \qquad (3.1.1)$$

Where the subscript "0" represents the state in the reservoir and "1" is a property of the beam. E represents the total energy of the bunch of particles, U is the potential energy, P is the pressure, V is the volume, m is the molecular mass of the particle and $N_A = 6.022 \times 10^{23}$ mol^{-1} is the Avogadro constant. When a vanishing small center-of-mass motion within the reservoir, the initial velocity can be assumed to zero, $v_0 \cong 0$. Experimentally, the overall terminal velocity of the beam, v_1, is determined by the terminal particles' velocity, $\langle v \rangle$. In addition to the enthalpy $H = U + PV$, the mean terminal particles' velocity can thus correlate with the enthalpy change:

$$\langle v \rangle = \sqrt{\frac{2(H_0 - H_1)}{N_A m}}. \qquad (3.1.2)$$

$\langle v \rangle$ is given by the terminal flow velocity provided that the center-of-mass motion of the particles in the reservoir; H_0 is the initial enthalpy of working fluid before jet expansion while the H_1 is the terminal enthalpy of the beam after a certain distance.

This means that an atomic helium beam (He^4: 4 amu) with precisely measured terminal flow velocity provides the magnitude of enthalpy change during the expansion. It is necessary to control and quantify the source pressure, P_0, and the source temperature, T_0, with high accuracy, because the computation of the source entropy, S_0, and of the source enthalpy, H_0, of the respective working fluid by means of an advanced equation of state (EOS) requires these two "actual" values of the source, see Figure 3-1. In combination with the systematic setting of jet source parameters and a suitable EOS, the experimentally determined enthalpy change can be used to define further macroscopic properties of the supersonic beam such as the atomic beam's temperature or the amount of condensation in the cluster beam.

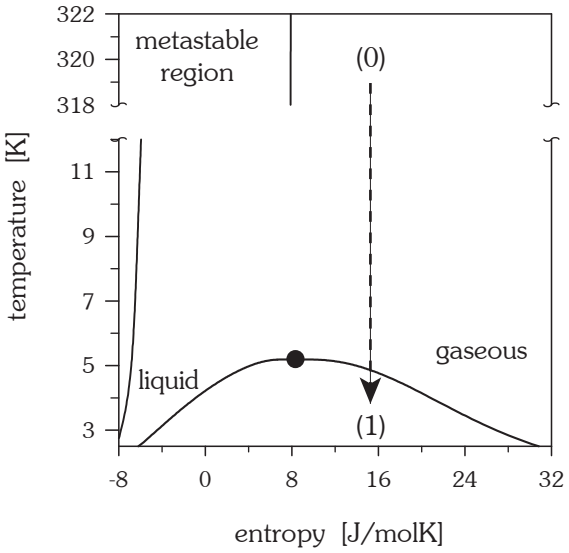

Figure 3-1 Helium *T*–*S* phase diagram with isentropic jet expansion trajectory. The vertical dash line indicates the change from helium initial state "0" to the final state "1", where the initial state "0" can be defined by the source conditions of temperature, T_0, and pressure, P_0. Based on the most accurate equation of state, the *T*–*S* phase diagram can be calculated according to the given reference condition.[107] Here, the critical point (black dot) is located at the temperature T_c = 5.20 K and the molar entropy S_c = 8.32 J mol^{-1}K^{-1}.

3.1 Nozzle Operation

To elaborate the nozzle action in a wide range of source conditions, the systematic research of jet sources not only requires a high precision, but also a steady state condition during the operation. Although the pulsed supersonic nozzle is widely used to generate an intense beam with low duty cycle, this fast-acting process is often simplified to ideal valve behavior with respect to the ideal gas system. However, when the initial properties of the working fluid need to be used to calculate the energies, the real acting behavior of the nozzle should also be considered. The characteristics of a nozzle have been described in Chapter 2, based on this Even-Lavie type valve we demonstrate that, in principle, it is possible to achieve quasi-continuous flow conditions. Two prerequisites, a minimum pulse duration and a suitable tagging of the appropriate beam segment, will be discussed in terms of diagnosing the flow behavior of a real fluid during the jet expansion.

3.1.1 Pulsed Duration of the Beam

Detailed electronics setting can be found in Chapter 2, Figure 3.1-1 illustrates a control signal of rectangular pulse shape and pulse width of δt_0 applied at the valve driver, which determines the corresponding opening time of the valve, δt_v. Based on the full width at half maximum (FWHM) of this opening duration, the pulse is thus defined. Though it is obvious that all pulsed valves cannot achieve steady-state conditions for pulses that are shorter than the rise time of the valve opening (the limitation of current valve is $\delta t_v \leq 10$ μs).

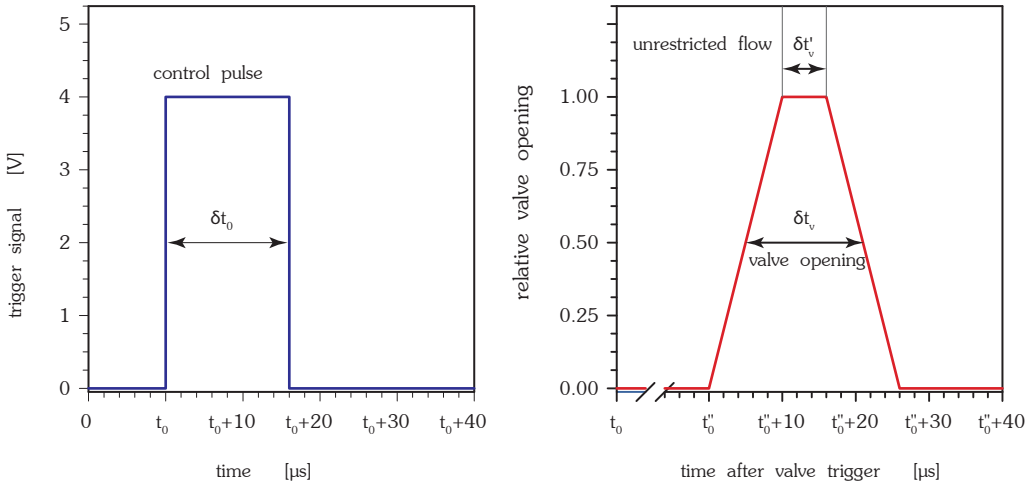

Figure 3.1-1 Schematic pulsed nozzle operation.[50] (*left*) The rectangular pulse shape is electronically generated by a valve driver, which allows a short opening time of δt_0 = 16.0 µs. (*right*) The trapezoidal structure of real valve operation contains an innate delay by the movement of plunger in the nozzle (~ 10 µs, estimated by the approximated speed of 10 ms^{-1} and a full stroke of 0.1 mm) for the rising or falling edge. Thus, in order to match the FWHM of δt_v to the ideal δt_0 of 16.0 µs, the constant flow region in an ultra short pulse can only be maintained for $\delta t_v' \leq 6$ µs.

Experimentally, this actual opening characteristic of a valve can be investigated, making use of ultraviolet photons that are emitted from excited particles right in front of the valve and detected by a suitable detector. The resulting time-resolved spectrum in Figure 3.1-2 demonstrates a convolution of the opening function in Figure 3.1-1 to the local velocity distribution of the expanding particles. This ultraviolet signal ends up with the width of δt_p with a shape similar to an exponential power distribution

$$f(t,a,b,c)\,dt = \frac{1}{2bc^{1/c}\Gamma\left(1+\frac{1}{c}\right)} exp\left(-\frac{|t-a|^c}{cb^c}\right) dt\,, \qquad (3.1.1)$$

which includes rise time and fall time in accordance with the expected value of 10 µs and a short period of flat-top.

One may consider that the "flat-top" shape of the distribution in Figure 3.1-1 as a constant flow behavior at first glance. However, the significant enlargement of signal amplitude after we slightly increased the solenoid current, I_v, set at the valve driver, implies that the steady-state condition has not been reached. That is to say, the constant flow of density doesn't directly refer to a fully opened valve.

In addition, Figure 3.1-2 shows that the width of the photon peak, δt_p, is varied when the distance between valve and electron source, l_{ve}, is changed from 6 mm to 11 mm. By extrapolating the "zero" distance for the "true" nozzle opening, the variation in photon pulse width provides an estimated effective opening time of the valve of $\delta t_v \approx 0.85 \times \delta t_p$ for the l_{ve} = 11 mm. Finally, a thorough study of the dependence δt_p (δt_0, I_v) reveals the full opening of the valve is presented in Figure 3.1-3. The overall analysis suggests a lower threshold of a true valve opening time of $\delta t_v \geq 40$ µs for saturating the photon signal, meaning that the flow is throttled for shorter times.

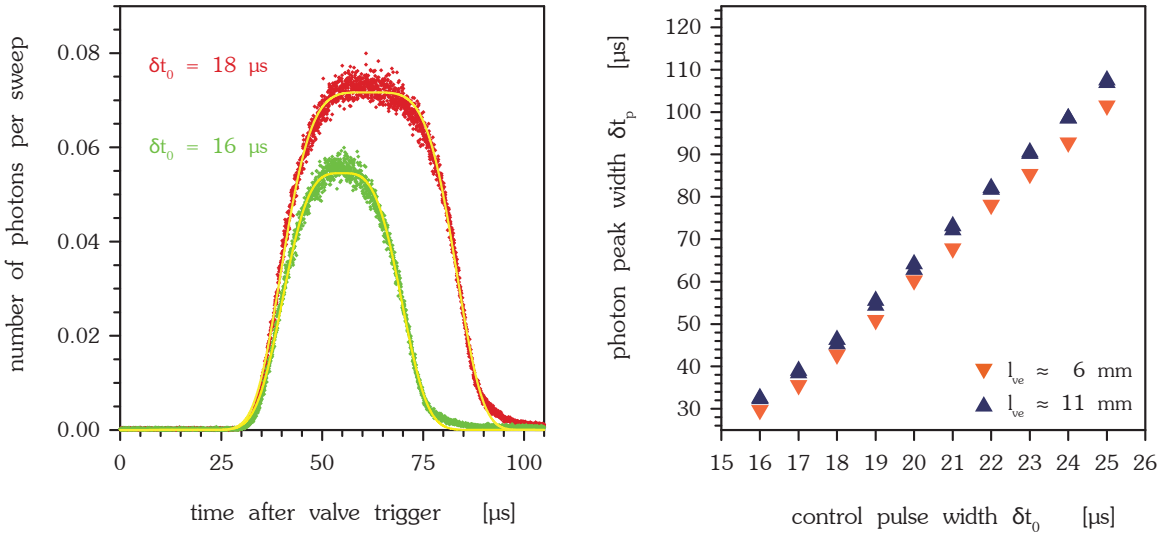

Figure 3.1-2 Illustration of pulsed helium beam along the time axis after the valve trigger. (*left*) Ultraviolet photons recorded by MCP detector.[50] These photons were emitted from electronically excited helium particles close to the e-gun. Two different pulsed opening settings (pulsed time of δt_0 = 16.0 and 18.0 μs) are depicted to experimentally confirm the trapezoidal structure of real valve operation. The yellow line is the nonlinear model fit by an exponential power function, which describes the photon peak width, δt_P. (*right*) The linear relation of controlled pulsed width from the valve driver versus the detected width from UV photons. When the distance between the fixed valve and the e-gun, l_{ve}, is enlarged from 6 mm to 11 mm, the resulted photon peak width becomes wider.

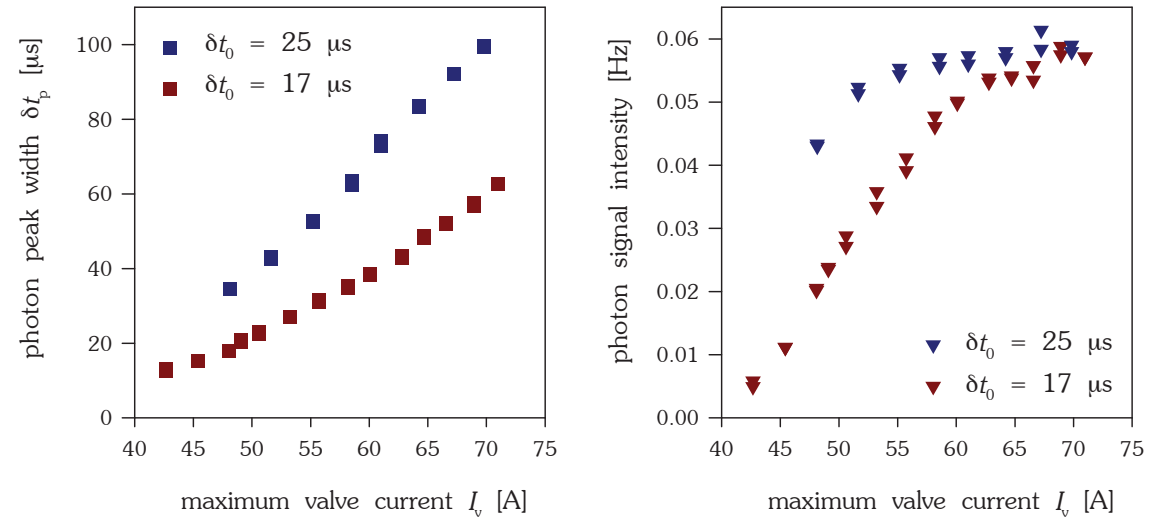

Figure 3.1-3 Relation between the valve current, I_v, and the photon peak. (*left*) Width of photon peak versus the maximum valve current with two different duration of the valve control signal of δt_0 = 17.0 μs and δt_0 = 25.0 μs. (*right*) The saturation threshold of $I_v \geq 64$ A indicates that the signal intensity of photon peak higher than this threshold is independent of the "effective valve opening", which means the valve can be considered as fully opened. When the $I_v \geq 64$ A is referenced to the photonic peak width, the minimum δt_p should be greater than ~ 47 μs to ensure the full opening of the valve. The e-gun is placed at a distance of $l_{ve} \approx 11$ mm downstream to the nozzle exit.

In short, the collision-induced fluorescence signal provides a vivid image of real acting of the valve, which helps to determine the operating parameters required for an entirely open valve. Also, the direct photon signal from the very early stage holds the advantage of not being affected by later events such as the beam–skimmer and beam–residual gas interactions.

3.1.2 Suitable Tagging of the Beam Segment

Just after the pulsed beam has left the nozzle, the strong particle-particle collisions result in a velocity distribution of particles with two characters: translational cooling and cluster formation. As the helium jet expansion above the ambient temperature possibly rules out the effect from the cluster formation[108], in this section, we slice the beam in 1 μs step and probe its terminal velocity spread to understand the translational cooling. The "coldest" region would thus indicate the steady-state status within the beam.

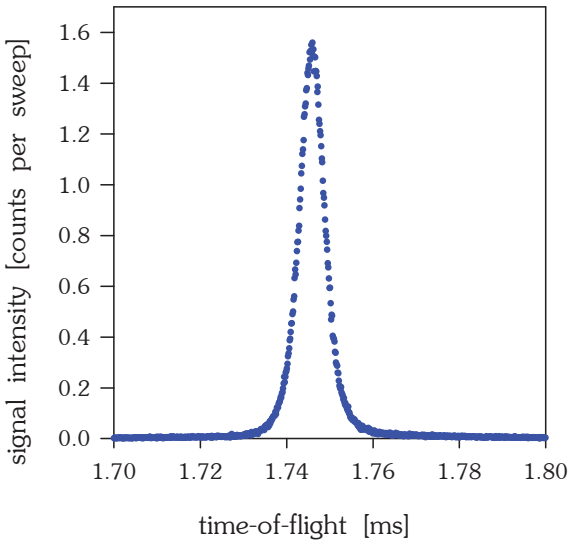

Figure 3.1-4 Time-of-flight spectrum of an electronically tagged helium beam (or metastable helium, He^*) at source conditions of P_0 = 9.60 MPa and T_0 = 319.0 K. The ultra-fast electronic excitation is 300 ns long with the electron energy of 140 eV. This excitation is chosen to tag the pulsed helium at 90 μs after the nozzle opening, t_0.

For the supersonic expansion of He^4 at T_0 = 319.0K and P_0 = 9.60 MPa, in Figure 3.1-4, an excitation duration of 300 ns in FWHM from electronic source is used to tag the helium beam. The particles in the helium beam are excited to the metastable state by varying the time delay between the gate control pulses (t_1) of the electron source and of the valve driver (t_0), $t_1 - t_0$, see Figure 3.1-5. According to different time delays, those tagged particles reveal the details of particle distribution in 2 μs steps. Each part of tagged beam arrives the MCP detector ~ 1.3 – 2.0 ms after the valve trigger for current instrumental setting with the total flight distance of ~ 3 m, the long-lived metastable helium with a life-time of 19.7×10^{-3} s for the 2 $^1S_0$ state[109] or 7.9×10^3 s for the 2 $^3S_1$ state[110] permits the energetic particles can be detected before they were self-quenched.[111]

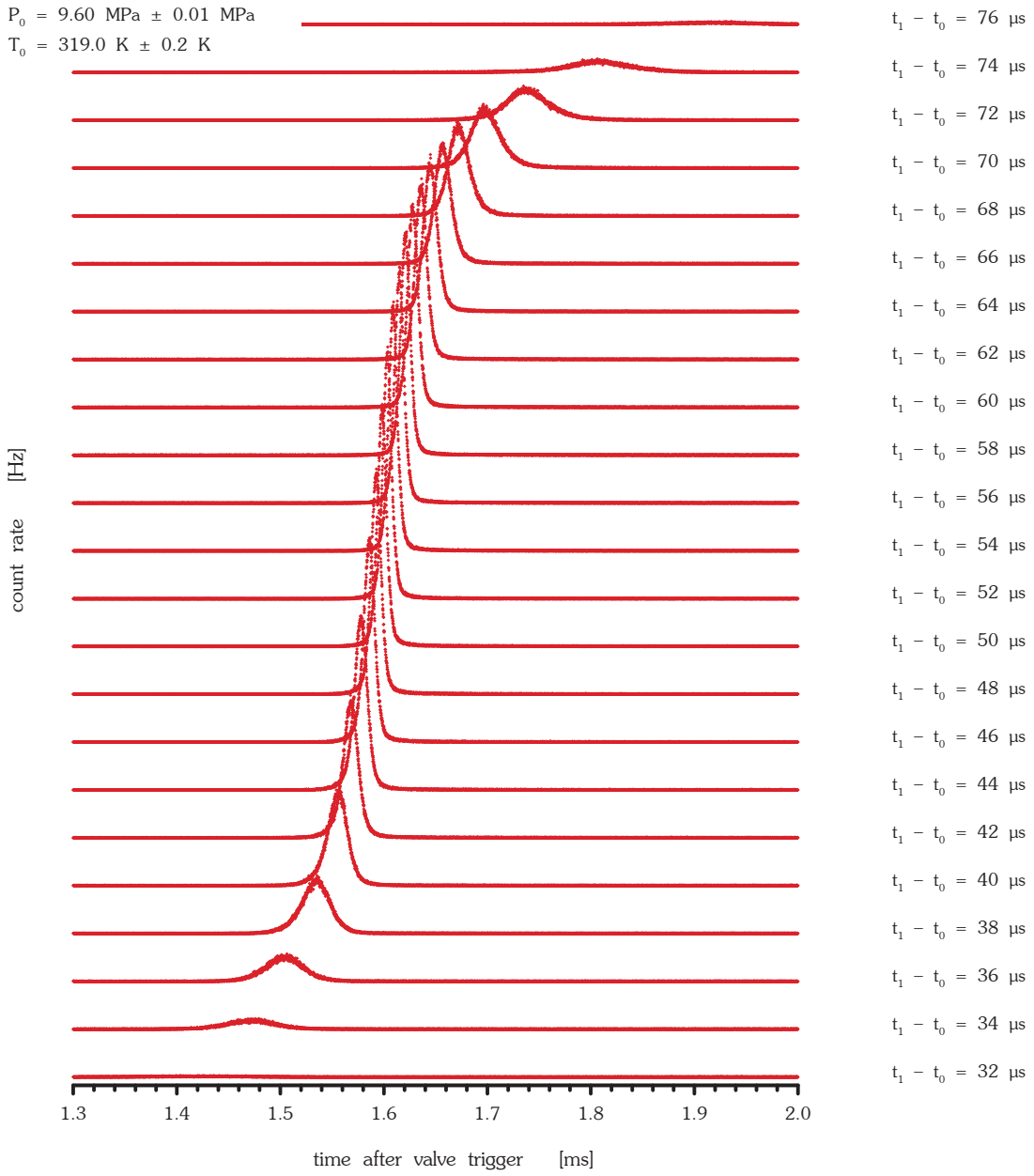

Figure 3.1-5 A series of metastable helium (He^*) arrival time distribution spectra (600 sweeps) from electronically tagged He beams as a function of the time delay between the valve opening and the electronic excitation, $t_1 - t_0$. The electronic excitation time is δt_1 = 300 ns and the time resolution of a spectrum is 128 ns.[50]

Figure 3.1-6 shows the terminal signal intensity of the metastable helium at given time delay. This intensity distribution reflects the density map of expanded helium particles in front of the electron source, which can be seen as a photo shoot of helium particles just left the nozzle. Clearly, the signal intensity won't be saturated if the nozzle's pulse duration is shorter than 16 μs; on the other hand, the width of the signal distribution is only getting broad after the pulse duration is longer than 17 μs. This result is in a good agreement with the observation of photon's signal, where the true valve opening time must be $\delta t_v \geq 40$ μs to provide a constant intensity of emitted photons.

3.1.3 Quasi-equilibrium Condition

Frequently, the maximum of the signal intensity is directly selected as the starting parameter to probe the beam experiments, however, the highest signal doesn't guarantee to represent the steady-state condition. Once we consider another property such as the peak width of the metastable of helium, the decreasing peak width appears at the later time delay when the pulse duration is longer than 17 μs. Here, the peak width of the metastable helium is described by the statistical dispersion–interquartile range (IQR), which is the 1st quartile subtracted from the 3rd quartile (in section 2.2.2).

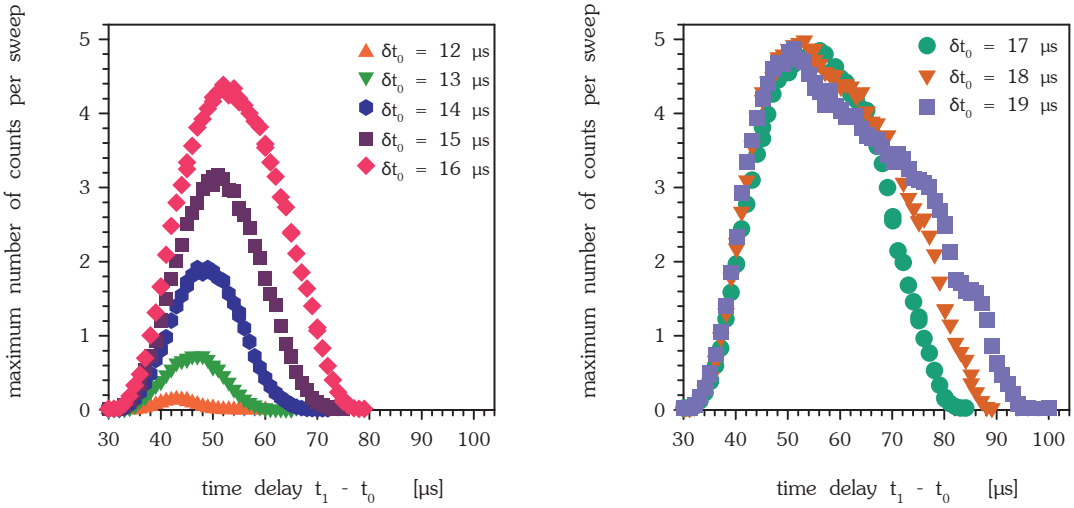

Figure 3.1-6 Comparison of valve opening duration, δt_0, and the statistical He^* signal amplitudes from different time delays between the valve opening and the electronic excitation, $t_1 - t_0$, at helium source conditions of $P_0 = 9.60$ MPa and $T_0 = 319.0$ K.[50]

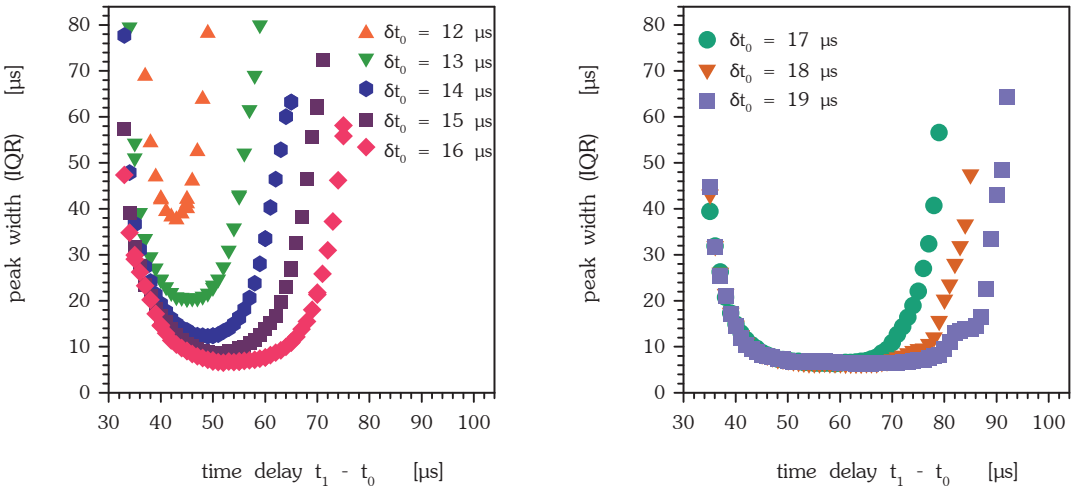

Figure 3.1-7 Comparison of valve opening duration, δt_0, and the He^* signal widths (by statistical interquartile range, IQR) from different time delays between the valve opening and the electronic excitation, $t_1 - t_0$, at helium source conditions of $P_0 = 9.60$ MPa and $T_0 = 319.0$ K.[50]

The minimum of IQR within each pulsed beam decreases no more after the controlled pulsed width is over $\delta t_0 = 21$ μs, see Figure 3.1-7. This second criterion for discriminating the steady-state status during the jet expansion has described that spread of metastable helium can be well confined in the middle of the pulse. Consequently, the arrival time of these confined particles might represent the beam's velocity.

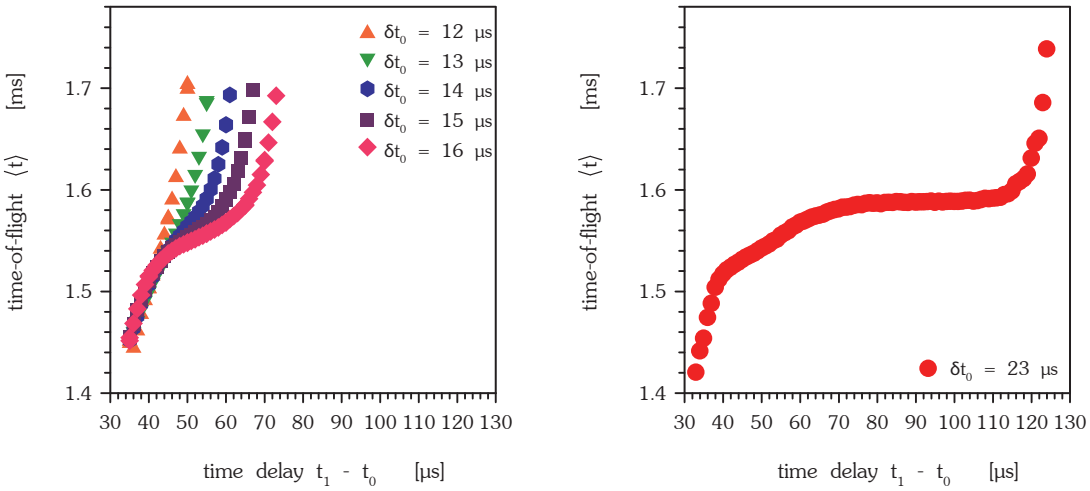

Figure 3.1-8 (*left*) Mean He^* time-of-flights (TOFs) from different time delays between the valve opening and the electronic excitation, $t_1 - t_0$, against valve opening durations, δt_0. For short valve opening durations, no constant period of TOF was validated. (*right*) When the valve opening duration, δt_0, is longer than 23 μs, a non-changed mean TOF can be determined by the time delay ($t_1 - t_0$) between 84 μs and 93 μs. Helium source conditions are $P_0 = 9.60$ MPa and $T_0 = 319.0$ K.[50]

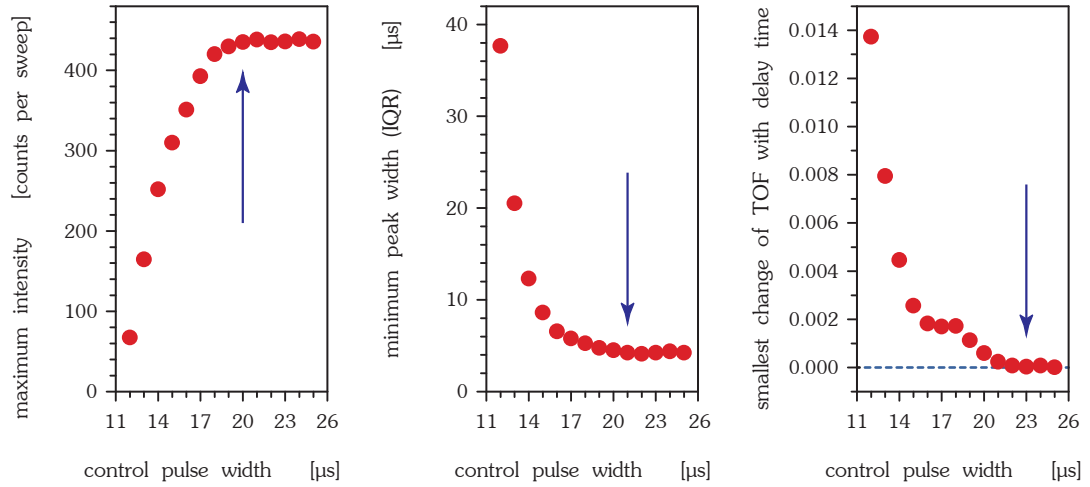

Figure 3.1-9 Three criteria for searching the steady-state condition in a pulsed helium beam. (*left*) A saturation of He^* peak height indicates the "full" open of the pulsed nozzle when the valve controller is regulated to have a longer opening duration, δt_0, than 20 μs at the extreme helium source conditions of $P_0 = 9.60$ MPa and $T_0 = 319.0$ K. (*central*) Minimized peak width at longer opening duration ($\delta t_0 > 21$ μs), which provides the least velocity spread of electronically excited particles (He^*) in a pulsed high-pressure beam. (*right*) The smallest change of TOF with delay time demonstrates the minimum requirement of opening duration ($\delta t_0 > 23$ μs) to reach the most unified particle velocity of He^*.[50]

The velocity of terminal particles within the beam will be identical if they have reached equilibrium during the jet expansion. In other word, the smallest change of the velocity, if close to zero, of each slice should validate the existence of a steady-state condition. Experimentally, the mean velocity, $\langle v \rangle$, of terminal particles is the flight distance (l) divided by the time-of-flight (TOF),

$$\langle v \rangle = \frac{l}{TOF} = \frac{l}{\langle t_2 \rangle - t_1} . \qquad (3.1.3)$$

Here, the TOF represents the metastable helium's real flying time between the electronic excitation (t_1) and the mean arrival time ($\langle t_2 \rangle$) at the detection side. On the other hand, Figure 3.1-8 shows the smallest change of the TOF versus the controlled pulsed width, the $\delta t_0 \geq 23$ μs gives an even higher threshold of pulse duration to ensure that the velocity, velocity spread, and the particle density all reach the steady-state condition within the beam.

To sum up, the most sensitive criterion to ensure the quasi-equilibrium condition is the homogeneity of particles' velocity. Even though the pulsed molecular beam is normally assumed to provide the particles moving at approximately equal velocities, the high resolution (in nanosecond scale) electronic slices the pulse and validates the steady-state flow condition more accurately. As a result, the quasi-equilibrium condition can be found inside of the beam, from the helium source conditions of T_0 = 228.0 – 410.0 K and P_0 = 0.60 – 10.80 MPa, the constant velocity and spread of these tagged particles are thus useful to operate with the thermodynamic equation of state (EOS) to calculate other physical properties of the beam. An improved method of determining the ultra-precise particle velocities will be discussed separately in the later chapter.

3.2 Skimmer and Background Scattering Effects

In this section, comprehensive source conditions such as densities or sampling rates were used to define the beam properties, followed by changing various skimmers with the tunable distance to the nozzle in the range 0 – 200 mm. By comparing the difference between initial and final particle distribution of the beam, this study is intended to investigate three main issues: (a) residual gas effect, (b) a non-disturbed beam condition, and (c) beam skimmer interaction. After systematic study of the most sensitive segment of the helium pulse, with improved understanding of the beam evolution, this research provides a simple method to improve the speed ratio and simultaneously rescue sensitive helium clusters during the jet expansions. This knowledge is of particular interest to cluster science, molecular spectroscopy, and quantum physics.

3.2.1 Residual Gas Induced Collisions

We firstly controlled the repetition rate of a pulsed beam sampling from 1.0 to 25.0 Hz to determine the number of particles per pulse from a helium source with high pressure. Figure 3.2-1 shows the pressure of gas particles from the first chamber recorded by an oscilloscope, where the valve connected to the next chamber is closed. Therefore, the pulsed helium beam will be evacuated after it collides with the wall of the first chamber, meaning that the particles removed by the pump are equal to the number of particles expanded to the first chamber in a steady state.[112] When combined with the pumping rate, $\Delta V/\mathrm{s}$ = 820 L/s for helium, of the turbo molecular pump, the number of particles per second removed by the turbo pump, $\Delta n/\mathrm{s}$, can be estimated by the modified ideal gas law, $P_{\mathrm{avg}}(\Delta V/s) = (\Delta n/s)\mathrm{RT}$. Here, the P_{avg} is the averaged background pressure and T is assumed to be room temperature: 300 K. Later, the variable $\Delta n/s$ can be converted to the n_{p}, the number of particles per pulse expanded to the first chamber, dividing by the pulse repetition rate. As a result, at a source temperature of T_0 = 319.0 K, pressure P_0 = 9.60 MPa and a valve opening of δt_{v} = 28 μs, each pulse of helium beam contains $n_{\mathrm{p}} \approx 10^{17}$ particles.

After the jet expansion, because of the parabolic shape of the nozzle, these particles are well focused and mostly move directly to the detector. In the current instrumental setup, two skimmers are placed between the first and the second chamber to remove the outer part of the beam and keep the ultra-high vacuum conditions in the detection chamber. Thus, a strong interaction between a dense beam and first skimmer yields many deflected particles. Obviously, the first skimmer located at the first chamber plays an important role in regulating the residual gas. When the sampling rate of pulsed beam increases, the number of residual gas particles in this chamber also increases (observed by higher average background pressure).

Normally, the valve opening of jet expansion should confine the entire pulse to be shorter than the flight distance in the first chamber, which ensures fewer collisions of the pulsed beam and the residual gas in the chamber. The later part of the pulsed beam, however, in the current setting, can still collide with the back-scattered gas particles from the front part of the beam. This interference will affect the transmission of particles to the

next chamber, the attenuation of weakly bonded clusters and the temperature of the pulsed beam. To quantify the effect of the residual gas, again, we monitor the electronically excited He* with the repetition rate of pulsed beam sampling from 1.0 to 25.0 Hz.

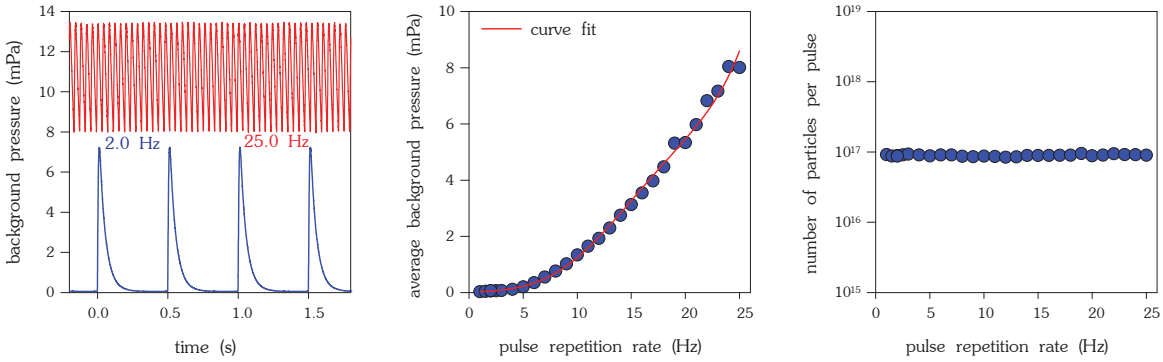

Figure 3.2-1 Analysis of helium particles per pulse by recording the background pressure versus pulse repetition rate from 0.5 – 25.0 Hz. (*left*) Comparison of background pressure at the pulse repetition rate of 2.0 Hz and 25.0 Hz. (*central*) Mean background pressure as a function of pulse repetition rate from 0.5 – 25.0 Hz. The curve fit is based on the modified ideal gas equation of $P_{avg}(\Delta V/s) = (\Delta n/s)RT$, where both the environmental temperature and pumping rate of 820 L/s for helium are assumed to be constant. Therefore, the parameter Δn can be calculated accordingly. (*right*) Resulted number of particles per pulse (n_p) is fixed at ~ 10^{17} regardless the pulse repetition rate. This constancy represents the high stability of nozzle operation till its frequency of 25.0 Hz.

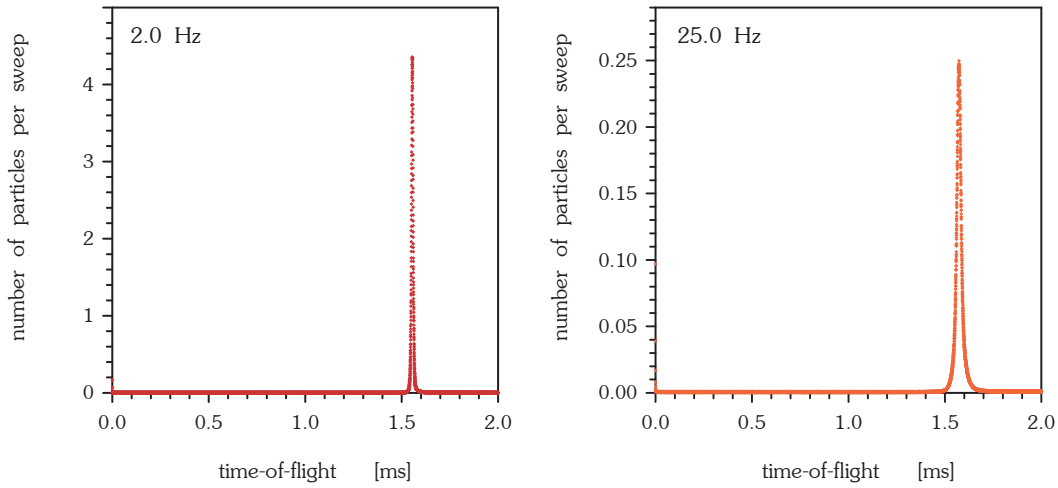

Figure 3.2-2 Difference of He* time-of-flight (TOF) spectra between the pulse repetition rate of 2.0 Hz and 25.0 Hz. At higher frequency, the TOF spectrum is broader but with lower signal intensity. The possible interpretation is that the higher pulse repetition rate induces the residual gas pressure in the chamber. Therefore, the electronic excited He* has a higher possibility to collide with the residual particles and consequently deviates from the central line of the beam or undergoes de-excitation process. In the end, the remaining He* particles show broader distribution and slightly longer mean TOF. Source conditions of helium are T_0 = 319.0 K and P_0 = 9.60 MPa.

In Figure 3.2-2, the arrival time spread of terminal He* from 2.0 Hz is much narrower than which at 25.0 Hz. On the other hand, the signal intensity at higher repetition rate

seems to be diminished. In addition, the mean arrival time also seems to be later when the source operates at 25.0 Hz. All these facts indicate the collision de-excitation/quenching of He^* in the first chamber. Clearly, the higher repetition rate can reduce the time in data acquisition or aid better count statistics for a fixed period. But this trade-off is not always beneficial to other purpose, for instance, to generate a colder beam.

A thermodynamic description of energy includes rotational, vibrational and translational motions of a particle. The rotational and vibrational motions are not included in an atomic beam system – pulsed He gases expansion. Because the atoms, in principle, only carry the initial energy from an equilibrium source status, the adiabatic process in a jet expansion allows those particles to demonstrate their thermodynamic energy in translational movements. Therefore, the thermal energy dispersion in this pulsed helium beam is going to express as a velocity spread of those particles, which are influenced by the local temperature in the beam. Here, a speed ratio (*SR*) is frequently used to express the velocity resolution of the beam. This speed ratio can be determined experimentally by a non-disturbed time-of-flight (TOF) spectrum,

$$SR = 2\sqrt{\ln 2} \times \frac{\langle TOF \rangle}{\delta t} = 2\sqrt{\ln 2} \times \frac{\langle t_2 \rangle - t_1}{\sqrt{\delta t_2{}^2 - \delta t_1{}^2}}. \qquad (3.2.1)$$

Here the mean time-of-flight is determined by the real traveling time of the He^* between the electronic excitation (t_1) and the mean arrival time ($\langle t_2 \rangle$) at the detection side; the measured particle spread, δt, is the full width of half maximum (FWHM) of the He^* arrival time distribution. Since the excited He^* has an inherent width from the electronic excitation of 300 ns, δt_1, the resulted spread of δt_2 should de-convolve with the innate δt_1 to reveal the actual particle spread, $\delta t = (\delta t_2{}^2 - \delta t_1{}^2)^{1/2}$, during the jet expansion. However, this correction only affects less than 1% of the FWHM because the very short excitation time.

After the SR is calculated, this value can provide an estimation of translational temperature, $T_{||}$. Assuming an isentropic expansion of an ideal gas, the translational temperature is expressed as[113]

$$T_{||} = T_0 \left(1 + \frac{\gamma - 1}{\gamma} SR^2\right)^{-1}, \qquad (3.2.2)$$

where $\gamma = C_p(\text{constant pressure})/C_v(\text{constant volume})$ is the ratio of heat capacities. When the helium beam starts at high source temperature, the ideal gas assumption can be even accurate. In short, the terminal velocity spread of particles relates strongly to the local temperature of the beam.

Therefore, the more collisions of the pulsed beam to the residual gases, which uptake higher temperature when they were scattered off the chamber, the warmer the helium beam will be determined by the particle spread. Figure 3.2-3 shows ascending dependency of the repetition rate to the terminal particle spread, where only below 3.0 Hz one can obtain the least disturbed beam. Also, the unchanged TOF and higher signal intensity both indicate that the lower sampling rate of pulsed helium diminishes the further collision to the residual gas in the first chamber. In the end, the sampling rate of 2.0 Hz permits minimized disturbances for pulsed helium to be expanded from a very high pressure of 9.60 MPa.

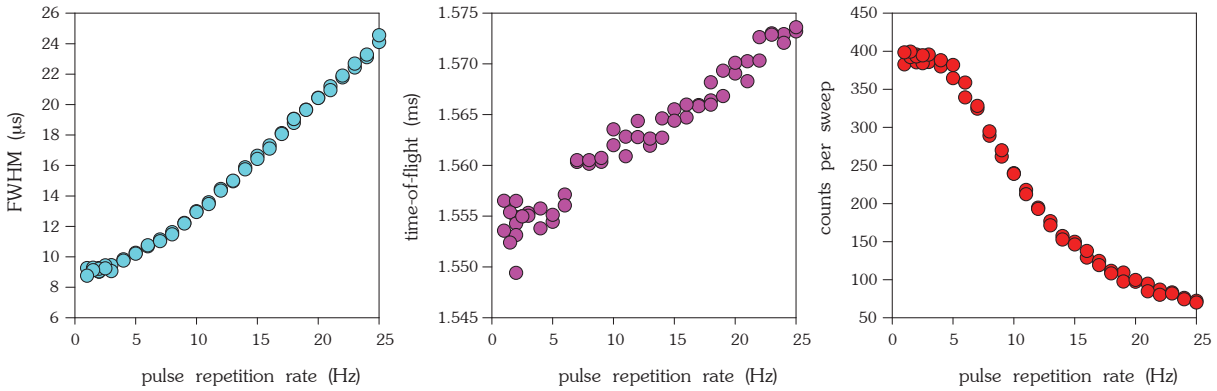

Figure 3.2-3 Strong influence of pulse repetition rate (0.5 – 25.0 Hz) to the spectra's spread, mean time-of-flight and signal intensity of the arrival He^* distribution. Source conditions of helium are T_0 = 319.0 K and P_0 = 9.60 MPa.

3.2.2 Non-disturbed Beam Condition

What is worth mentioning is the ultraviolet photon signal revealed first in our current publication,[50] which provides an opportunity to reveal the beam profile with minimized beam–residual gas interactions. This fast photon signal from the early stage has passed the ~ 3 m chamber and arrived at the MCP detector just a few nanoseconds after the helium beam was excited. Comparing the arrival time of photons to the metastable helium particles (He^*) which arrive later, the large difference in time scales between nanosecond and millisecond already indicates the decoupling of these two signals. In Figure 3.2-4, the earlier signal reveals the "live" image just after the electronic excitation at the exit of jet expansion, which was recorded by the detector before the jet subsequently collided with any other particles in the chamber.

This photon signal also increases when the source density increases as shown in Figure 3.2-5. A wide range of densities, different source temperatures, and pressures were applied to confirm that the tendency is independent of these two parameters. Therefore, the proportionality directly supports the idea that the emitted ultraviolet photons originated from the collision induced quenching of excited helium particles. The non-linear deviation of the photon signal at higher densities illustrates that some excited helium atoms may not only undergo elastic scattering and radiate afterward. Instead, some of them possibly were stuck and formed weakly bonded clusters at this stage. Experimentally, the existence of helium clusters in the supersonic beam that was expanded above ambient temperature has been firstly measured by the quadrupole spectrometer to support this interpretation. This observation will be further discussed in the final part of this chapter.

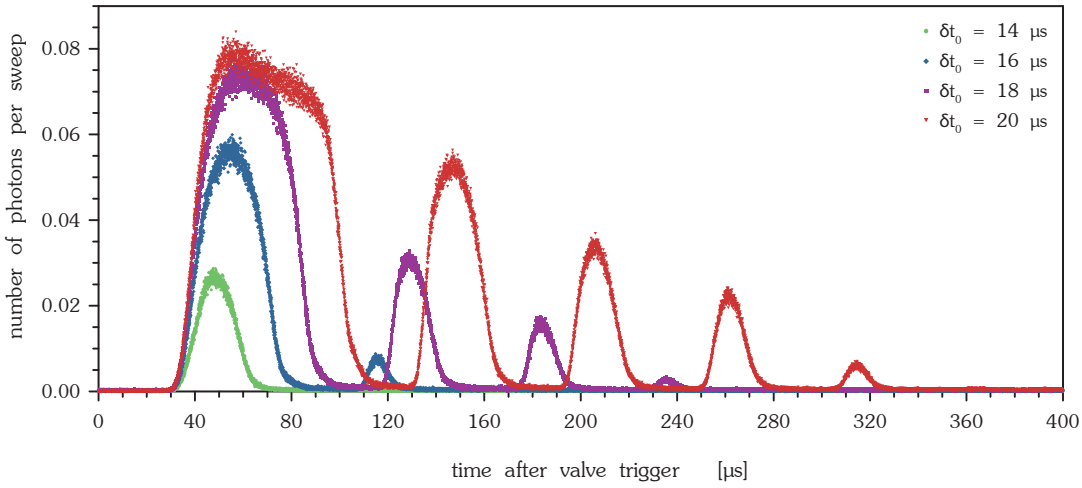

Figure 3.2-4 Depicted valve bouncing behavior for different pulse durations. The recorded signal by MCP detector is the emission of ultraviolet (UV) photons from metastable helium particles (He^*) in the pulsed beam, which are continuously excited by e-gun for 4 ms after the valve opening.[50] As the pulsed duration increases, the overall number of valve bounces (because the valve opening/closing is operated by a strong spring, see section 2.1.1.) displays a more than single event. Source conditions of helium pulsed beam are T_0 = 319.0 K and P_0 = 9.60 MPa.

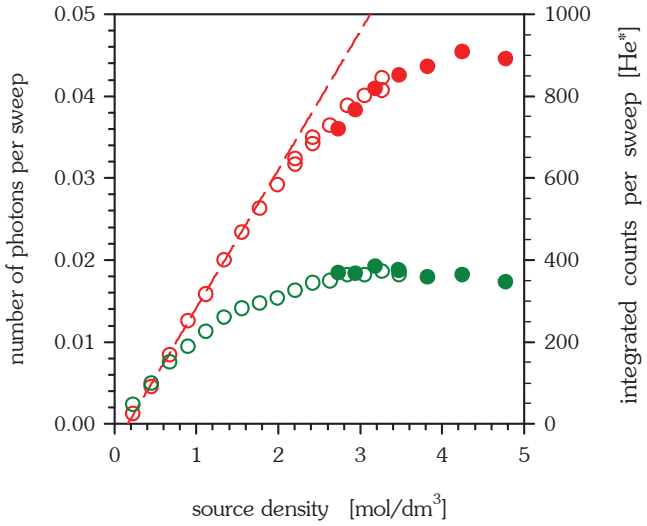

Figure 3.2-5 Dependency of helium source density to the signal of metastable helium (He^*). The red circles represent the source density dependence of the ultraviolet (UV) emission from the excited helium in the early stage, where the dashed line demonstrates the linear correlation up to source density of ~ 1.8 mol/dm^3. On the other hand, the green circles represent the source density dependence of the signal intensity from the terminal arrival time distribution of metastable helium, He^*. The hollow circles were obtained by the same source temperature of T_0 = 319.0 K and the solid circles were obtained by isobaric condition of P_0 = 9.60 MPa, all these source densities were calculated by the real gas equation of state.[107]

For the photon signal, the photon tagging technique with good time resolution not only rules out the non-targeting sequential bounces after the first valve opening, but also allows us to probe different portion of the beam internally. As a result, by recording the time-dependent slicing as a beam scan of metastable helium, the evolution of jet expansion from the nozzle via skimmer till the final detection can thus be precisely deduced. The “flat-top”

region of the photon profile has demonstrated the original constant flow property within the pulse and thus confirmed the existence of steady state status (in section 3.1). However, the difference between this profile and the scanning profile of metastable helium is quite large, especially in the later excitation period, see Figure 3.2-6. The reason of this cave structure can be attributed to several events happened during the jet expansion.

Firstly, concerning to the pulsed beam, the inner collision induced quenching of the excited helium particles might result in signal attenuation, especially along the central line of jet expanding. By this precondition, the decay should be directly proportional to the density (collision probability); in other words, the profile of helium signal should similar to the distribution of photons but only be multiple by certain scaling factor. This concept seemed to work only at the first 20 µs, but the following strong decay after 50 µs cannot be explained. However, the asymmetric decay of the signal showed an alternative effect from the beam to the environment.

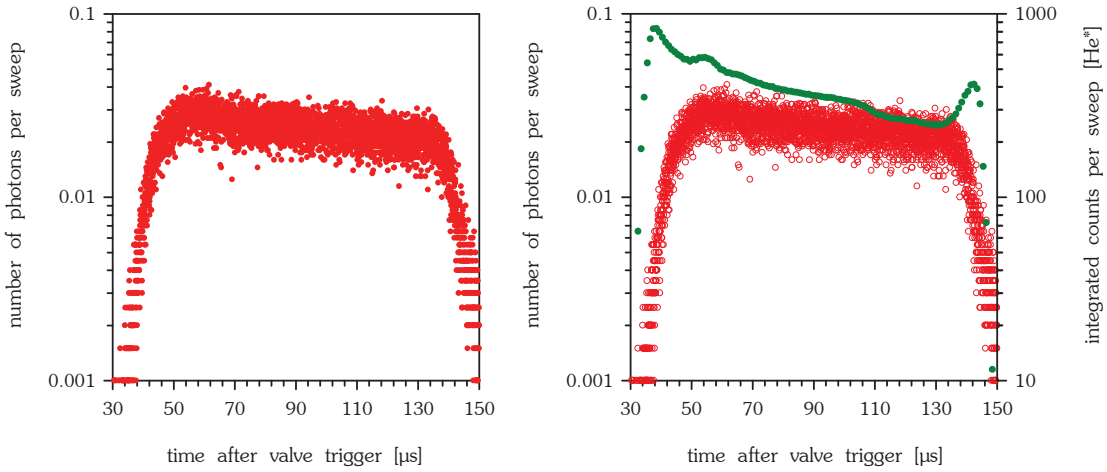

Figure 3.2-6 Structure of pulsed helium beam from the emitted UV photons and the terminal He^* particles. (*left*) The red dots represent ultraviolet photons resulting from a pulsed, electronically excited He beam at a source pressure of P_0 = 9.60 MPa and a source temperature of T_0 = 319.0 K, providing an ultrafast *in situ* characterization of the jet in the early stage. (*right*) The green dots represent the integrated signal intensity in 1.0 µs step as a function of a time (t) after valve trigger; the overall counts in a spectrum include arrival time range from 1.3 – 2.0 ms and were standardized by the number of sweeps.

Secondly, based on the instrumental setup, the expansion chamber was maintained below 10^{-4} Pa, followed by a propagation chamber in ~ 10^{-8} Pa and final to the detection chamber in ~ 10^{-7} Pa. Except the expansion chamber, the ultra-high vacuum condition is supposed to minimize the collisions between pulsed beam to the residual gases from the rest of flying path. Only at first chamber, the background pressure is strongly raised by the collision of a pulsed beam to the skimmer and also to the inner wall of the chamber.

All reflected particles by collision-induced quenching or by oriented perturbation might attenuate the excited helium signal especially for the later part of the pulse. In view of above-mentioned reason, this effect of signal quenching should be examined when the distance between nozzle-skimmer ($d_{N–S}$) is varied.

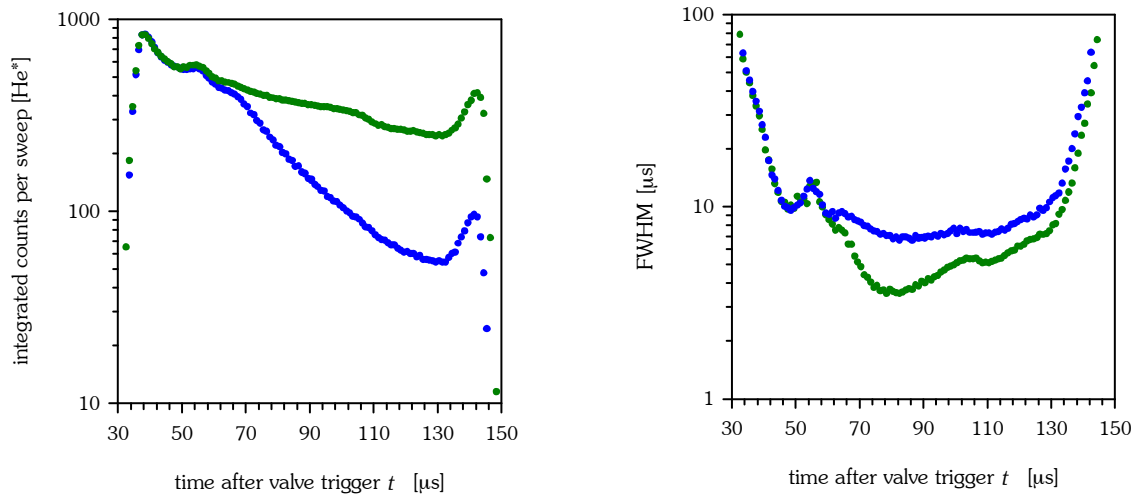

Figure 3.2-7 Effect of beam–skimmer interaction to the terminal He^* distribution. The blue dots represent the terminal metastable He^* signal in 1.0 μs step as a function of a time delay at the fixed nozzle–first skimmer distance of 183.3 mm, and the green dots display the scanning results from the enlarged nozzle–first skimmer distance of 233.3 mm. (*left*) The integrated counts of a spectrum include arrival time ranges from 1.3 – 2.0 ms and was standardized by the number of sweeps. (*right*) The full width of half maximum (FWHM) derived by the fitting of Student's t probability density function expresses a measure of peak spread. A time delay (t) in each plot is the difference between triggering the gate control signals of the electron source (t_1) and of the valve driver (t_0), $t = t_1 - t_0$.

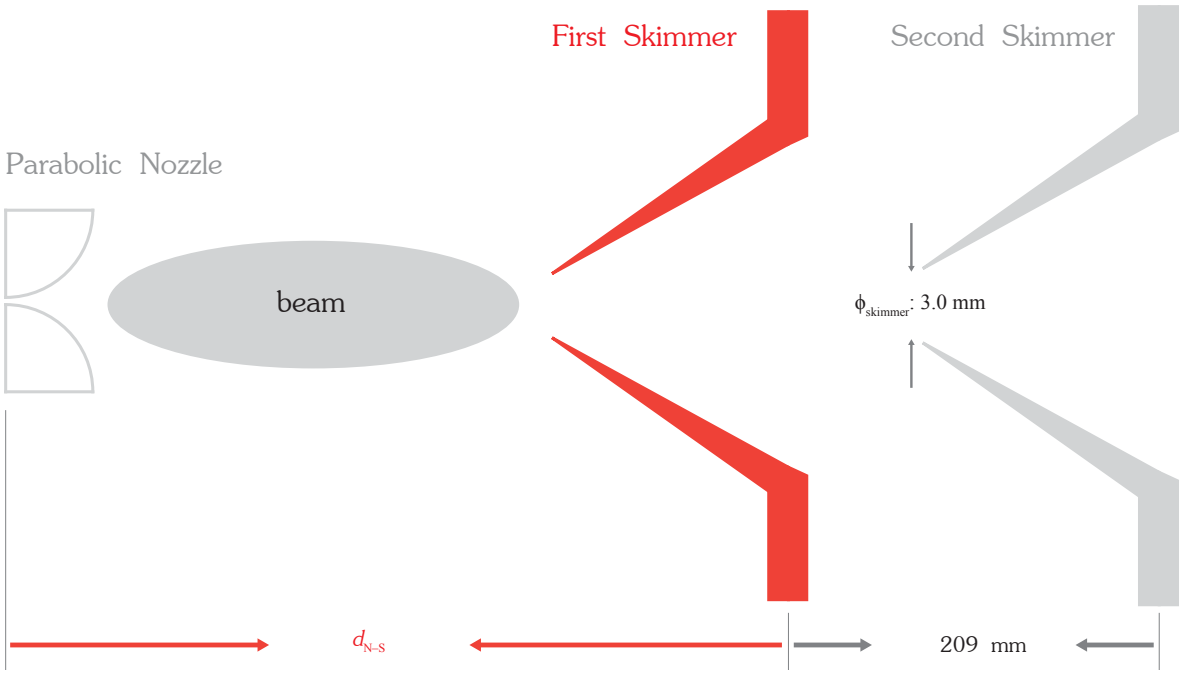

Figure 3.2-8 Illustrated relation of nozzle to two skimmers in current ultra high vacuum machine. The distance between nozzle and first skimmer, $d_{N–S}$, from 33.3 mm to 233.3 mm, can be varied by a linear translator (TN_z) along the beam axis, while both skimmers are mounted on the chamber with a fixed distance of 209 mm. Three different first skimmers were used to investigate the beam–skimmer interaction.

Comparing the metastable helium signal from different $d_{N–S}$ of 183 and 233 mm in Figure 3.2-7, the maximum intensity of the signal remains the same in shorter time delay, while the signal is increased at longer time delay for the setting of 233 mm. This experiment clearly pointed out the importance of strong perturbation by skimmer positioning in Figure 3.2-6, which causes the downstream beam profile may no longer directly proportional to the source conditions. Figure 3.2-7 displays that the gain from the extending $d_{N–S}$ not only yields higher signal intensity but also narrower spread of the metastable helium distribution. These improvements encouraged the follow-up studies of the systematic variations of nozzle in the next section. To sum up, the measurement of the photon signal is a useful tool to scope the beam profile and diagnose the disturbance in the instrumental configuration.

3.2.3 Beam Skimmer Interaction

Till now, the effect of the residual gas in the first chamber has already been investigated to ensure the least interference. We then turned to monitor the next occurrence when the pulsed beam passes the skimmer. Figure 3.2-8 depicts the relation between the nozzle and two skimmers. Two aspects are often considered for the design of skimmer: acceptance angle with respect to the beam and minimum interaction between the particles. Experimentally, the tunable distance of the nozzle to the skimmer ($d_{N–S}$) can determine the geometry of the former term while the later term can be realized by changing different type of skimmer. Both these results are going to be discussed in this section.

Owing to examine the beam to skimmer interaction, the nozzle mounted on a linear translator will be tuned for various distances along the beam axis. This distance variation determines the helium particle density just in front of the first skimmer. From a geometric point of view, the skimmer allows more particles to pass when the acceptance angle is large, meaning that the shorter $d_{N–S}$ results larger acceptance angle with respect to the nozzle. Although the higher signal intensity is benefit for the data evaluation, if the nozzle is nearly attached to the skimmer, huge amount non-ordered particles from the outer shell of the beam may cause very high background pressure and subsequently induce the extra collision to the desired beam. This effect surely needs to be avoided.

On the other hand, when the $d_{N–S}$ is too long, the skimmer might only permit very small amount of the beam to pass to the next chamber, especially when the diameter of skimmer is also relative small regarding the size of nozzle. That is to say, to carefully investigate the $d_{N–S}$ is essential to the beam with extreme high source density. Figure 3.2-9 shows a correlation of speed ratio (SR) to the $d_{N–S}$ from different source pressures.

As mentioned earlier, the SR represents the “uniformity” of the beam, which will be reduced if the interference increases. Clearly, at the source pressure below 1.20 MPa, the $d_{N–S}$ only affects SR when it is shorter than 100 mm. For a commonly used criterion of $d_{N–S}/d$ (diameter of the nozzle, which is 0.1 mm in our case) ≥ 1000,[114,115] if below this pressure (1.20 MPa/ 9000.7 torrs), the beam seems not to be affected by the skimmer. However, if the source pressure is extremely high over 9.60 MPa, the beam–skimmer interaction still degrades the speed ratio as $d_{N–S}/d > 2500$.[34,116]

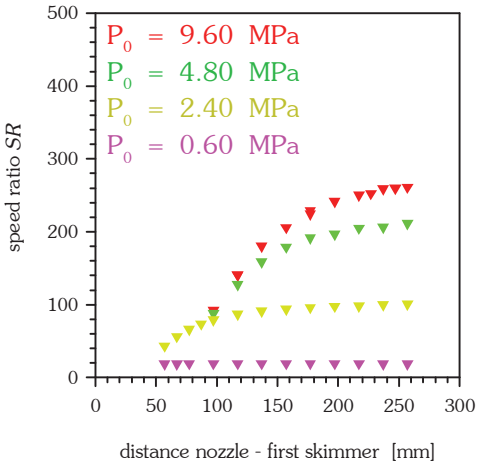

Figure 3.2-9 Depicted triangles represent the nozzle – first skimmer dependence of the highest terminal speed ratio within the pulsed beam from different helium source pressures at fixed T_0 = 319.0 K. Apparently, the speed ratio is dramatically decreased for a high source pressure at shorter $d_{N–S}$ (distance nozzle – first skimmer). This home built/mechanical drilled skimmer contains a stainless steel wall with a diameter of ϕ: 3.0 mm.[117]

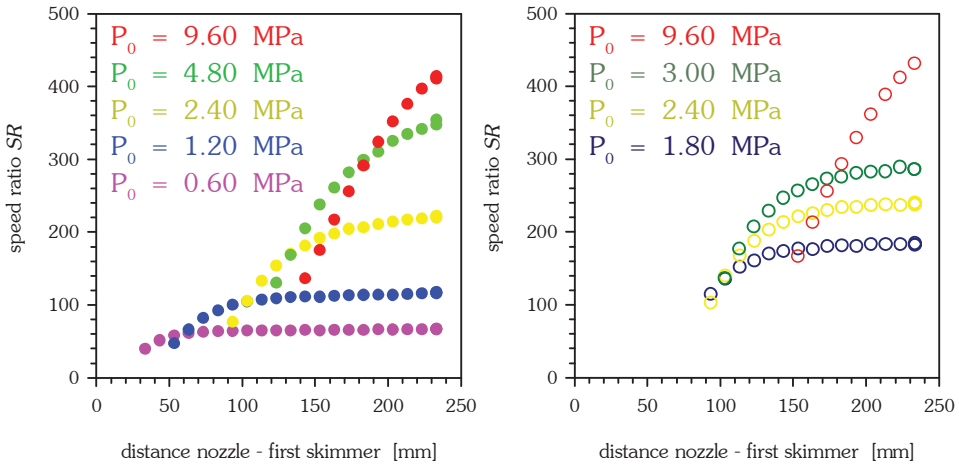

Figure 3.2-10 Effect of different first skimmer to the pulsed helium beam. (*left*) An ultra-thin wall nickel skimmer manufactured by *Beam Dynamics, Inc.* with a diameter of ϕ: 3.0 mm. (*right*) Another ultra-thin wall nickel skimmer with a diameter of ϕ: 2.0 mm. All helium source conditions are fixed at T_0 = 319.0 K. In addition, the highest speed ratio with respect to each helium source condition is determined by the "beam scan" of electronic tagging to the different portion of pulsed helium beam as discussed in section 3.1.

In the latest theoretical study, Even *et. al.* has already pointed out that the modification in skimmer design and positioning are required to allow the intense jet to propagate in a typical supersonic beam setup.[118,119] Herein, after the sufficient long $d_{N–S}$ has already improved the "unclogged" flight of the beam, we then turned to advance the body of the skimmer.

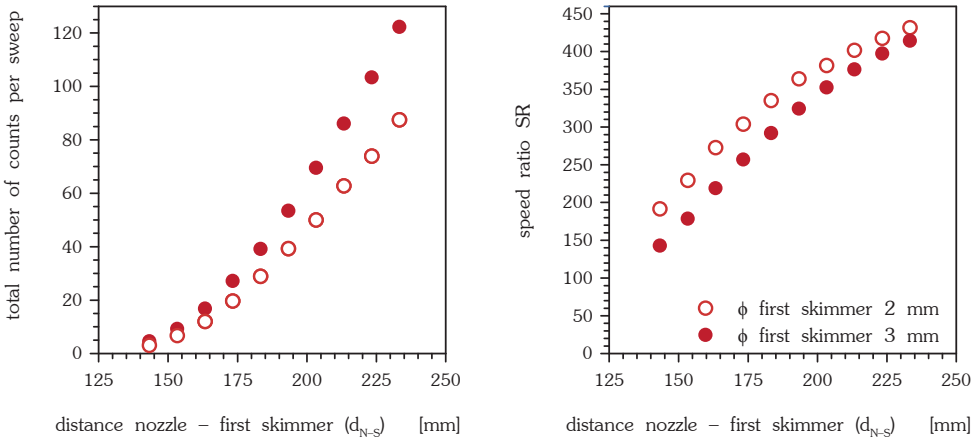

Figure 3.2-11 Comparison of terminal He^* distribution for different skimmer diameters. Helium beam at a source pressure of P_0 = 9.60 MPa and a source temperature of T_0 = 319.0 K was electronically tagged at the time delay ($t = t_1 - t_0$) of 90 μs for the quasi-equilibrium condition. (*left*) Larger skimmer diameter (ϕ: 3.0 mm) allows more helium particles to pass the hole and reach the detector. Shorten the distance between the nozzle and first skimmer results strong beam–skimmer collision, which reduces the terminal number of He^*. (*right*) Smaller first skimmer diameter (ϕ: 2.0 mm v.s. 3.0 mm) reduces the consequential beam–second skimmer (ϕ: 3.0 mm) interaction, which yields higher speed ratio as well as lower translational temperature. Because the vertical spread of skimmed helium beam with ϕ: 3.0 mm will slightly diverge in next 209 mm distance to the second skimmer, the beam–second skimmer collision is apparently larger than the beam skimmed by a ϕ: 2.0 mm skimmer. The experimental uncertainty is smaller than the size of each symbol.

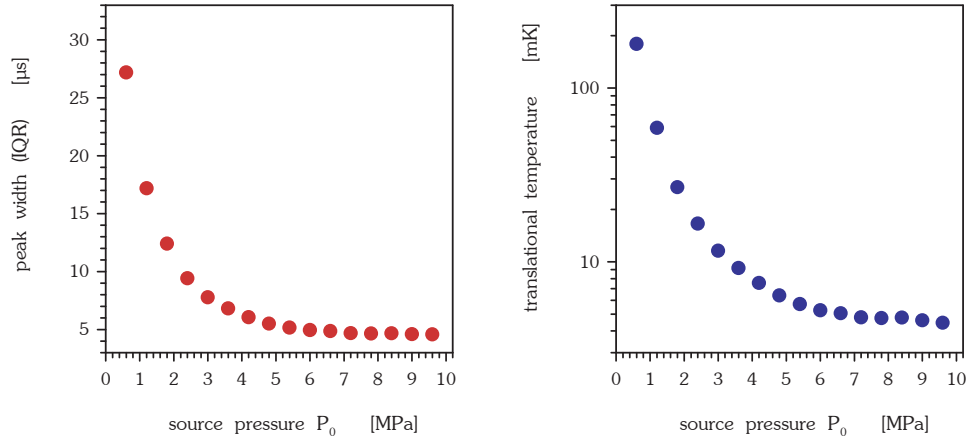

Figure 3.2-12 Pressure effect of translational cooling of helium beam from a fixed source temperature, T_0 = 319.0 K. (*left*) The relation of the narrowest peak spread by a statistical method (interquartile range, IQR) of terminal He^* distribution to various source pressures. (*right*) Calculated minimum translational temperature of pulsed helium beam versus source pressures of P_0 = 0.60 – 9.60 MPa. The experimental uncertainty is smaller than the size of each symbol.

Three different skimmers are mounted separately as the first skimmer to examine the beam–skimmer interaction. As you can see in Figure 3.2-9 and Figure 3.2-10, the thickest skimmer from the mechanically drilled stainless steel disturbs the beam most (Figure 3.2-9), which yields the lowest SR from the source pressure of 9.60 MPa.[117] For other two thin nickel skimmers (thickness of the orifice edge: 10 μm), the one with orifice diameter of ϕ: 2.0 mm results higher SR than another skimmer with ϕ: 3.0 mm.

This observation can be explained by the reduction of consequent interaction between the skimmed beam and the second skimmer. Even though the skimmer ϕ: 2.0 mm allows fewer particles to pass through, see signal intensity in Figure 3.2-11, the skimmed beam with smaller diameter is thus less disturbed by the second skimmer (ϕ: 3.0 mm) at the 209 mm downstream.

The optimized setting of skimmer permits a very high speed ratio, SR = 440, from a source condition of T_0 = 319K and P_0 = 9.60 MPa, which corresponds to the translational temperature of $T_{\parallel}$ = 4 mK. This systematic study of the least disturbed helium beam suggests that by restricting the residual gas and confining the suitable d_{N-S}, at given source temperature, 10 times higher in source pressure yields a 50 times colder terminal beam from a gas jet expansion, see Figure 3.2-12. In the end, such a "cold" beam of $T_{\parallel}$ = 4 mK implies the validation of helium clusters in the beam, because the binding energy of the He_3 is ~ 100 mK and He_2 is ~ 2 mK. [30,116,120]

3.2.4 Surprise: Validation of Helium Cluster

When the optimized colder beams were further detected by the quadrupole mass spectrometer (QMS), the helium clusters were found for the first time. These helium clusters were formed from the high source temperature (up to T_0 = 410.0 K) via helium gas expansion as shown in Figure 3.2-13. The cooling-down experiment at source pressure of P_0 = 9.60 MPa from T_0 = 410.0 – 228.0 K shows a gradual rise of the m/z = 8 signal, which indicates the increment of helium clusters. In the literature, Hagena and coworkers have demonstrated the empirical fitting parameters concerning to the mean size of cluster distribution,[18,102] which is the nucleation product from gaseous jet expansion, as shown in Eq. 2.2.10–12 (section 2.2.3).

Among the succeeding works,[105,121-126] the size of the rare gas clusters has been experimentally determined by the diffraction pattern of particles, high-energy electron diffraction, Rayleigh scattering or the particle scattering with atomic helium. In brief, the fitting results suggests no cluster formation when the condensation parameter, Γ^*, is smaller than 100, and the cluster formation up to the size of decamer when $100 < \Gamma^* < 350$. It seems that our source conditions with high source temperatures, unlike most of helium clusters in a jet expansion from the extreme low source temperature of T < 50 K,[127-131] are not able to generate helium clusters in the pulsed beam based on the current parameters of the scaling law. However, the unforeseen observation of cluster signal from the helium expansion of T_0 = 410.0 K and P_0 = 9.60 MPa motivates us to review the instrumental design.

After comparing many other machines that were used to determine helium clusters,[105,108,122,132] the significant difference in the mechanical design of our instrument is the placement of skimmers. The reduced beam skimmer interaction gives a rational interpretation of these measured helium clusters – they were the survivors and already preexist when the pulsed beam was expanded to the vacuum. When the nozzle moves closer to the skimmer, as shown in Figure 3.2-14, the signal of the helium cluster gradually falls until it vanishes at around 110 mm. This distance is equal to the value of x/d = 1100. In other

words, the common skimmer placing range of 10 – 1000 times the throat diameter may cause the extinction of helium clusters after skimming.

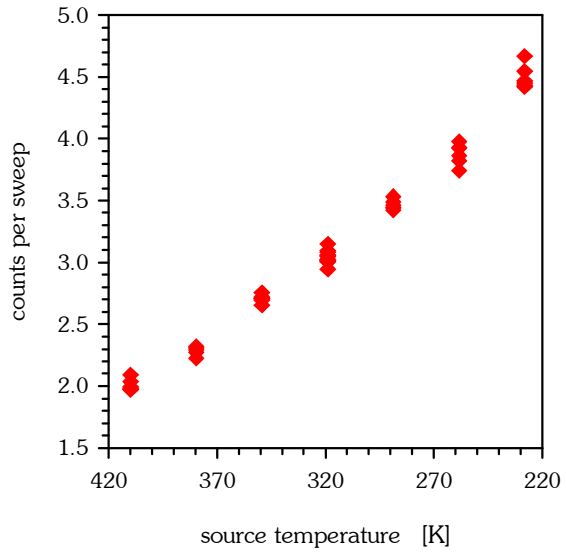

Figure 3.2-13 The red diamonds represent the source temperature dependence of the m/z: 8 signal from the pulsed helium jets, where the source pressure is fixed at P_0 = 9.60 MPa and the ionization energy is ~ 100 eV from the filament in the QMS.

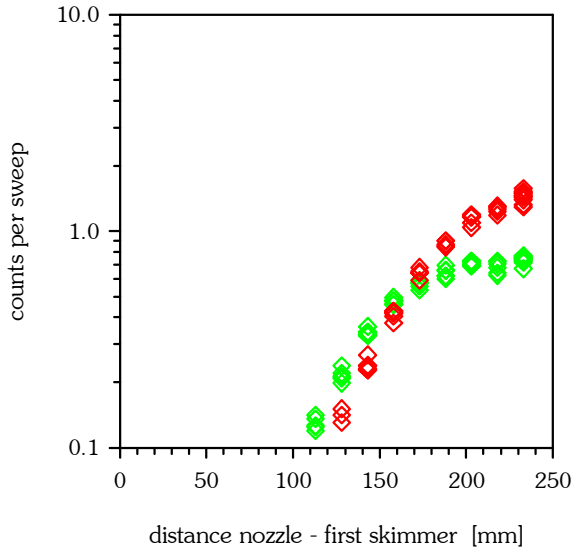

Figure 3.2-14 Depicted hollow diamonds represent the nozzle – first skimmer dependence of the m/z: 8 signal from the source pressure P_0 = 4.80 MPa (green) and P_0 = 9.60 MPa (red) at the source temperature of T_0 = 319.0 K. The strong decay clearly indicates no helium cluster will be observed at shorter distance below 100 mm, this cutoff is corresponding to the x/d = 1000 in our experimental setup. The maximized cluster transmission will only be reached by extending the distance nozzle – first skimmer at extreme high source densities.

In Figure 3.2-15, the QMS measurements of P_0 = 9.60 – 4.80 MPa at T_0 = 319 K extend the investigation of helium clusters to lower source densities. The roughly linear

correlation shown in the right side of Figure 3.2-15 implies that the helium cluster formation in the pulsed supersonic beam can be found even at very low source density of ~ 0.2 mol/dm^3. In short, the capture of helium clusters is a great achievement after carefully reviewing the skimmer effect by distance variation.

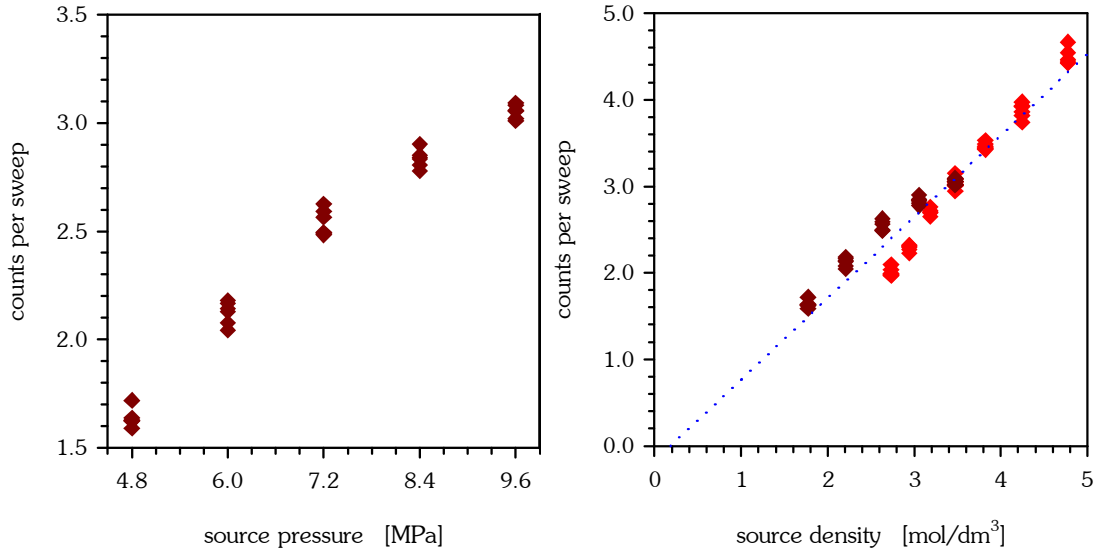

Figure 3.2-15 (*left*) The dark red diamonds represent the source pressure dependence of the m/z: 8 signal from the pulsed helium jets, where the source temperature is fixed at T_0 = 319.0 K and $d_{N–S}$: 233 mm. The ionization energy is ~ 100 eV from the filament in the QMS. (*right*) The dark red (fixed T_0 = 319.0 K) and red (fixed P_0 = 9.60 MPa) diamonds represent the source density dependence of the m/z: 8 signal from the pulsed helium jets, where the dashed line is the roughly linear correlation. The extrapolation gives a threshold of ~ 0.2 mol/dm^3, which can be converted to the P_0 = 0.60 MPa at T_0 = 319.0 K.

To sum up, we have verified two simple but useful concepts by systematically study source properties, vacuum conditions, and skimmer placements. To improve the beam transmission, the first concept was addressed to reduce the collisions of beam to the residual gases. Clearly, not only the upper threshold of average background pressure at 10^{-4} Pa is a good indicator for optimizing the sampling rate, but the spread of the pulsed beam can also be confined by this indicator afterwards.

When the aim turns to improve the translational cooling, the second concept of reducing the interaction between the beam and the skimmer was applied. Three different skimmers were then separately mounted and varied by multiple distances to the nozzle for extracting the pulsed beam. Later, the enlargement of distance between the nozzle and the first skimmer strongly improves the translational cooling of helium beam.

Ultimately, by combining the aforementioned enhancements, we are able to validate the helium clusters that were not assumed to exist in these source conditions before. These observations strongly indicate that the terminal size distribution of clusters in jet expansions may be varied by different degrees of the cluster–skimmer interactions, which should be determined more carefully in the future.

3.3 Spatial Distribution of Particles

The optimized source condition and the minimized interference result in extreme "cold" beams after a sufficiently long distance. Besides using UV photonic emission to demonstrate the valve operation and tagging of the metastable helium to scan the pulsed beam at the early stage, the terminal beam's distribution can be described according to the arrival time dependence. This spatial expansion allows us to experimentally verify the terminal beam's mean temperature by Maxwell-Boltzmann distribution. Also, the geometrical variation of the optimized pulse beam from various source conditions would be of interest for the design of an advanced detector for molecular beam experiment.

3.3.1 Parallel Distribution of Arrived Particles

In the current experimental setting, an MCP detector records each arrival time distribution of He^* along the beam axis for 2 ms. The resulted spectrum can be seen as a "photograph", which was taken at a specific time. That is to say, by streaming these photographs with a time coordinate, the output provides a film of terminal beam evolution. To align the time scale, with a fixed flight distance between the electronic excitation focus and the MCP detector, the mean arrival time of He^* in each spectrum is used to represent the interval. In the end, the mean arrival time versus signal intensity shows the parallel distribution of arrived particles, see Figure 3.3-1.

Apparently, the terminal beam has a mountain-liked shape, which is slightly different from the beam shape in the beginning. The main contributing factor is likely to be the beam–skimmer scattering, which should be verified in more detailed. As shown in Figure 3.3-1, the smaller the diameter of first skimmer is, the lower the signal is transmitted to the detector. If the diameter of the skimmer is fixed at $\phi_s = 3.0$ mm, the 50 mm shorter distance of nozzle–skimmer ($d_{N–S}$) results in a strong decay of signal intensity and the shape of the beam, especially at later times. These two observations have confirmed the strong effect from skimmer placements, which are in good agreement with the suggestion of extending the $d_{N–S}$ for better translational cooling.

Since the molecules do not exchange energy from collisions anymore after the jet expansion, the original energy of each molecule exhibits separate temperatures for vibrational, rotational and translational motion: T_{vib}, T_{rot}, T_{trans}. In particular the atomic helium beam, without vibrational and rotational movement, contains only translational energy, which can be measured as a translational spread in the experiments. Therefore, the lower translational temperature of the beam can be directly linked to the macroscopic "cold" beam.

Figure 3.3-2 shows the higher speed ratio is located at later arrival time, meaning that the front part of the beam is not as cold as the later part. Two possible reasons are listed here: (1) the leading particles do not reach steady state condition; (2) the leading particles face a stronger perturbation from the relatively warmer skimmer. When the valve is not fully opened, the collisional cooling during the jet expansion is not efficient. Only after the steady state flow condition reached, the quasi-equilibrium status allows the maximized

collisional cooling. Also, the front part of expanded beam surely passes through the skimmer earlier than the followed portion.

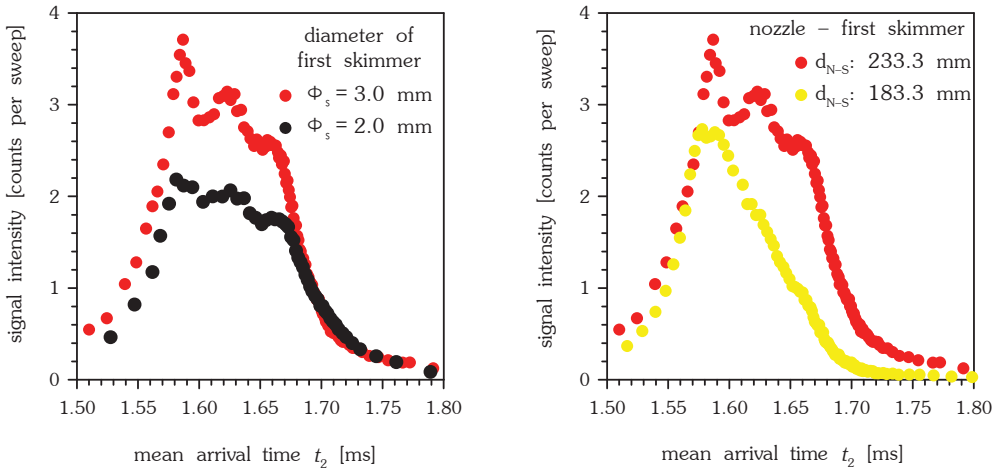

Figure 3.3-1 Depicted arrival time distribution is recorded by the MCP detector, which reveals the shape of terminal distribution of helium particles from a source condition of T_0 = 319.0 K and P_0 = 9.60 MPa. The signal intensity of arrived He^* and its mean arrival time can be statistically evaluated from a given TOF spectrum. A series of TOF spectra are taken from a scan of a pulsed helium beam with different time delay of electronic excitation, $t_1 - t_0$, in 1 μs step within the range of 32 to 126 μs. (*left*) According to different diameter of first skimmer, as predicted, the smaller cross section of the first skimmer yields lower particle signal on the detection side. (*right*) When the skimmer diameter is fixed at ϕ_s = 3.0 mm, shortening the distance between the nozzle and the first skimmer from 233.3 mm to 183.3 mm induces stronger beam to skimmer scattering. After that, the remaining non-disturbed particles result in less signal intensity. Also, the shape of helium beam is strongly changed especially in the later part of the beam because of the beam–skimmer interaction.

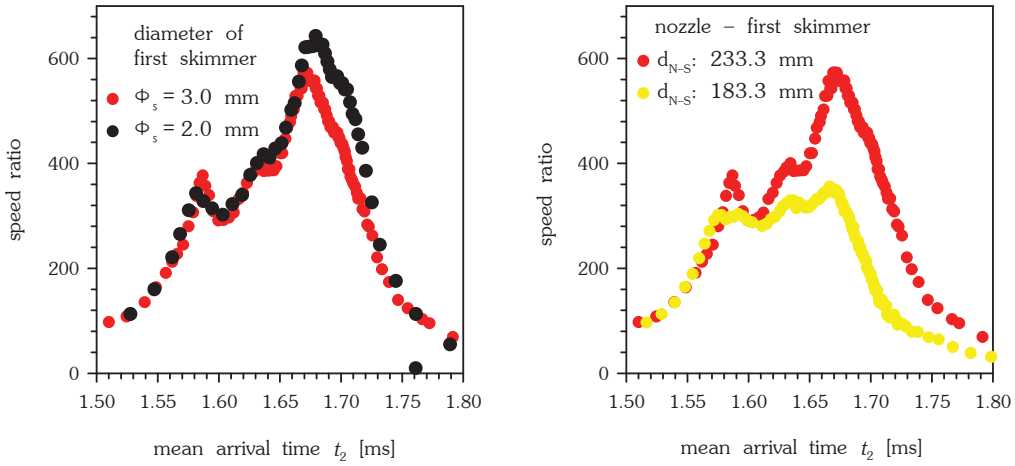

Figure 3.3-2 Skimmer effect on speed ratio from helium source conditions of T_0 = 319.0 K and P_0 = 9.60 MPa. (*left*) Smaller diameter of first skimmer reduces the consequent scattering of penetrated beam to the second skimmer, as discussed in section 3.3, which yields slightly higher speed ratio. (*right*) The reduced distance of d_{N-S} induces beam to the first skimmer scattering. This effect significantly reduces the terminal speed ratio, meaning that the helium beam seems to be "heated" by the first skimmer and not as cold as another setting.

3.3.2 Vertical Spread of Helium Beam

Besides the evolution of particles along the beam axis, the spatial spread displayed in the vertical direction also provides the "temperature" information of the beam. As long as the skimmed beam, in principle, allows all particles travel in the same direction behind the skimmer, the later particle spread in the vertical direction will display a transverse translational temperature ($T_{\perp}$). For one-dimensional Boltzmann distribution of helium particles perpendicular to the beam axis, the vertical velocity can be written as

$$f(v_y) = \sqrt{\frac{m}{2\pi K_B T_{\perp}}} e^{-\frac{1}{2K_B T_{\perp}} m v_y^2}, \qquad (3.3.1)$$

where the v_y is the velocity along the vertical direction and K_B is the Boltzmann constant. According to this formula, if the term m/K_BT is analogy to the σ^2 term of the Gaussian distribution function, the resulted particle spread will show a bell curve. Experimentally, the vertical velocity can be defined by the spatial spread of particles, see Figure 3.3-3. The geometrical relation between each particle and the central line of the beam gives the vertical velocity in certain time period. Therefore, the vertical velocity is able to correlate to the terminal temperature of a beam. Here, the temperature drop of particles from original source condition is often called geometrical cooling.

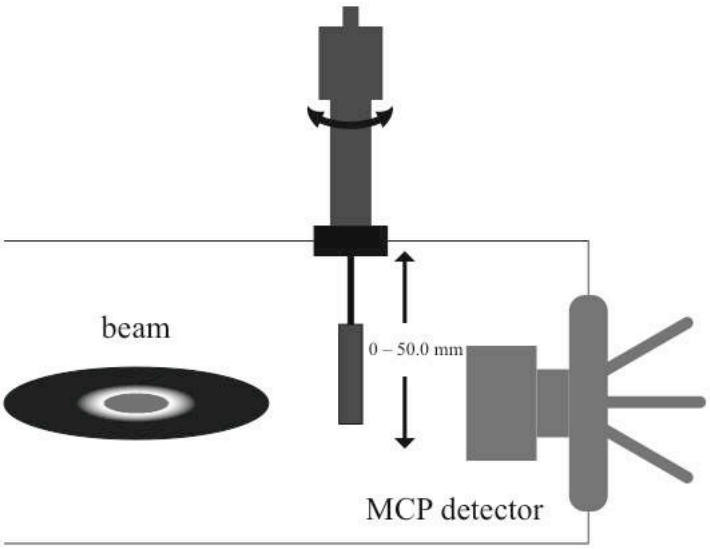

Figure 3.3-3 Drawing of a "beam blocker" sitting between pulsed beam and an MCP detector. This "beam blocker" is a vertically movable stainless steel plate (rounded square with a length of 40 mm). It is capable of linearly cut the beam and yields the vertical spread of particles in the beam.

We developed a "beam blocker" to stepwise cut the beam in front of the detector, aimed to learn the particle distribution along the vertical direction. As the beam blocker is mounted on a translator stage, which offers an interval of 0.01 mm and the scanning range of 50.00 mm. That is to say, the beam blocker gives a "green-light" at 50.00 mm and a "red-light" at 0.00 mm while it totally eclipses the MCP detector. In our current setting, the last

skimmer has ϕ_s = 3.0 mm in diameter, meaning that the helium beam inherently has 3.0 mm in width perpendicular to its central line.

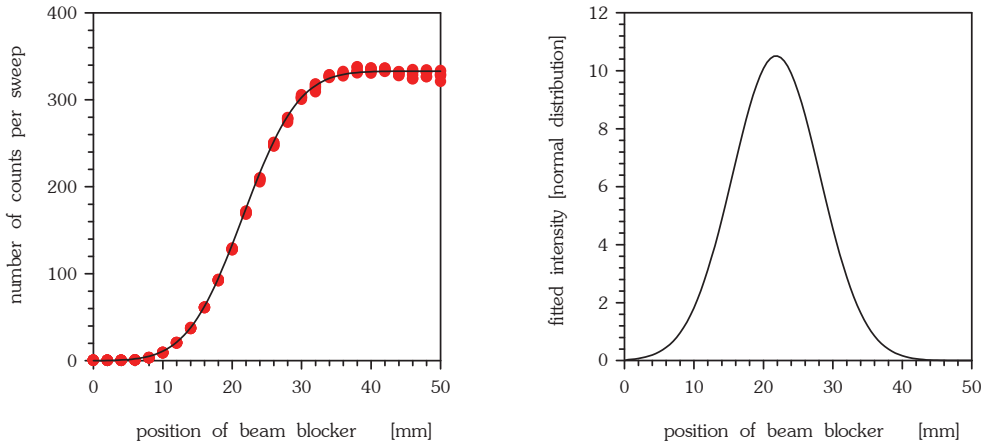

Figure 3.3-4 Vertical spread of helium particles at the position of "beam blocker". Helium source conditions are T_0 = 319.0 K and P_0 = 9.60 MPa, and the time-delay of electronic excitation is $t_1 - t_0$ = 52.0 μs for the maximum signal intensity within pulsed helium beam. (*left*) Recorded He^* signal intensities (red dots) versus the vertical positions of "beam blocker". Overall data are collected in 2.0 mm step by moving the "beam blocker" up or down. These data can be fitted by a scaled probability density function of cumulative normal distribution (or error function), which yields a black curve with fitting quality of R^2 = 0.997. The differentiation of this resulting cumulative normal distribution is a symmetric normal distribution. (*right*) Derived He^* distribution of excited particles along the vertical direction from previous differentiation. This normal distribution locates at 21.8 mm with a standard deviation of 6.3 mm.

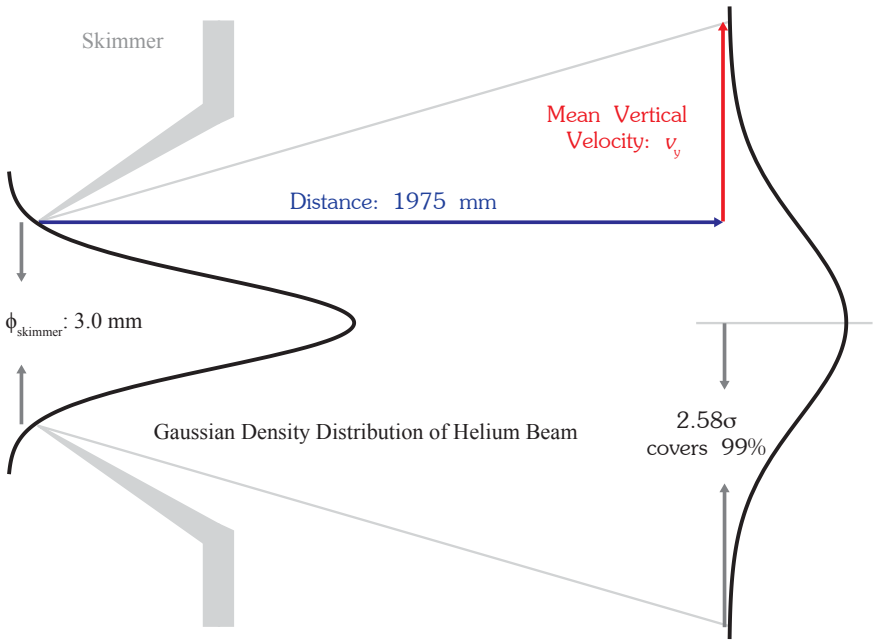

Figure 3.3-5 Schematic evolution of helium beam after passing the second skimmer in the ultra-high vacuum chamber. The position of "beam blocker" is located at ~ 1975 mm downstream to the second skimmer. Because of the Gaussian distribution (or normal distribution)-liked geometry, a ± 2.58σ range in vertical direction can be assumed to cover 99% of the helium particles. Thus, the mean vertical velocity of particles is calculated by a vertical shift (distance) over a helium flight time between second skimmer and the "beam blocker".

Figure 3.3-4 shows the vertical particle spread of helium beam from T_0 = 319.0 K and P_0 = 9.60 MPa. Apparently, the resulting curve is an error function-liked shape, which can be numerically derived to a bell curve. This resulted curve will be further fitted by a Gaussian distribution to estimate the standard deviation (σ) of the particle spread. Statistically, for a normal distribution, a ± 2.58σ ranges 99% of the confidence interval for the mean. The measured standard deviation of 6.32 mm should be multiplied by 2.58 to convert to 16.31 mm, this range in principle covers almost all the particles of the beam, see Figure 3.3-5.

In addition, by subtracting the inherently radius from $r_{skimmer}$ = 1.5 mm (diameter $\phi_{skimmer}$: 3.0 mm), the remaining 14.81 mm indicates the mean vertical velocity is ~ 13.58 m/s (the distance between last skimmer to the beam blocker is ~ 1975 mm and the mean velocity of helium beam is around 1825 m/s, which gives the time interval of ~ 1.08 ms). This transverse velocity correlates to the mean $T_\perp \approx$ 30 mK by Maxwell-Boltzmann speed distribution, $v_{rms} = (3RT/M)^{0.5}$, where M is the molar mass.

We have checked the spatial spread from two different segments by electronic tagging 52.0 – 52.3 μs (maximum of signal intensity) and 90.0 – 90.3 μs (minimum of spread along the expansion axis), both shows roughly the same size. At given source temperature, as shown in Table 3.3-1, pressure effect for helium gas expansion seems not to influence the mean $T_\perp$ over a wide range of P_0 = 0.60 – 9.60 MPa.

Table 3.3-1 Translational temperature of helium beam from a source temperature of T_0 = 319.0 K.

Source Pressure (MPa)	Time-Delay[a] (μs)	Center Position (mm)	Standard Deviation (mm)	Vertical Temperature ($T_\perp$ in mK)
0.60	65	21.84	5.91	25
1.20	60	21.83	6.26	29
2.40	60	21.60	6.53	32
4.80	59	21.86	6.40	30
9.60	52	21.81	6.32	30

[a] the time-delay of electronic excitation after valve opening, $t_1 - t_0$, represents the maximum signal intensity within a pulsed helium beam.

In short, the two directional scan of helium beam is discussed in this section. The vertical scan provides mean $T_\perp \approx$ 30 mK regardless the source pressure of the beam, while the parallel spread results in the coldest parallel temperature, $T_\parallel$, from 100 to 10 mK as the source pressure was increased from P_0 = 0.60 to 9.60 MPa, see Figure 3.2-12. Since all the precision of those translational temperatures are heavily relied on the accurate velocity determination, in the next section, we are going to demonstrate the improved methodology.

3.4 Ultra-Precise Particle Velocities

The experimental determination of the speed of particles is a frequent task in natural science because the change of particle's velocity expresses the energy transfer from internal energy to kinetic energy or the other way round. Despite the fact that the kinetic energies of atoms, molecules, and clusters are often given by measuring the mean speed of the particles, only few molecular beam experiments offer the highly accurate (uncertainty less than 1%) velocity of measured particles.

After defining the steady-state condition of the supersonic beam and optimizing the beam transmission, in this section, the advanced experimental setup will be used to derive the particle velocity with ultra-high accuracy. For the current settings of a pulsed high-pressure jet source with high brilliance and optimum repeatability, the flight distance of a few meters can be varied with a tolerance of 50 μm which results in a precision in the mean flight time of particles of better than 10^{-4}. To ensure data accuracy, one first has to consider thereproducibility of each measurement for a given source condition. Then, the repeated data should be evaluated by statistical analysis.

3.4.1 Statistics and Stability

In earlier section 2.2.2, the procedure of data acquisition from MCP detector to the TOF spectrum has been described. In short, the analog signal as a function of time from the excited particles has been converted to the digital signal, and this digital data is consequently split into short intervals of equal length. If this time interval is short enough, the interval length is often assumed not to affect the precision of identifying peak positions.

The random uncertainty in the estimate of the mean arrival time, $\langle t_2 \rangle$, is given by the standard deviation of the centroid, σ_c, and is independent of the peak shape:[97]

$$\sigma_c = \frac{\delta t_2}{\sqrt{N}}. \qquad (3.4.1)$$

Here N is the number of measurements contributing to the peak, δt_2 is the standard deviation. From this formula, it is straightforward to conclude that a narrow distribution with plenty of repeat measurements is going to diminish the uncertainty in the estimated peak position. When we consider the fast-acting pulsed beam, the width of the pulsed beam is limited by the mechanical design to a few microseconds. The advanced electronic tagging technique of excited particles allows us to probe a much narrower distribution in a hundred nanoseconds, which provides a good signal quality with respect to the statistics. As the internal uncertainty of the data acquisition from given arrival time distribution is reduced, one should also proceed to solve the external factors.

The stability of source conditions is the dominated factor of the entire molecular system, including source temperature, source pressure and sampling's repeatability. As mentioned earlier, the pulse duration of the nozzle is defined to reach the stationary flow condition at given source pressure and temperature. In addition to fixing the repetition rate of sampling at 2.0 Hz, this actual valve opening is thus varied by case with ± 1.5 μs difference as the true valve opening time of $\delta t_v \geq 80$ μs. However, the tagging technique by ultra-short

electronic excitation allows us to slice the quasi-equilibrium segment inside the pulse, meaning that the fluctuation of valve opening can be avoided if we only probe these excited particles.

As the speed of those excited particles in quasi-equilibrium segments are only influenced by source temperature and pressure, here, we quickly review the instrumental specifications. For source temperature, the combined uncertainties from sensor, meter, and calibration yields a maximum deviation in absolute temperature of ± 0.2 K in the operation range of 225 K – 425 K.[49,51] However, the poor thermal conductivity of the nozzle's stainless steel body provides a good "thermal equilibrium" of temperature oscillation of ± 0.05 K. On the other hand, for source pressure, it is stabilized to better than the accuracy of ± 0.5 kPa by a high resolution pump.

The terminal flow velocity has been calculated using the most recent equation of state of helium and assuming a terminal beam temperature of T_1 = 2.1768 K, resulting in a value of $\langle v \rangle$ = 1830.6 ms^{-1}. When the total flight distance is 3.000 m, this velocity corresponds to a time-of-flight of $\langle t \rangle$ = 1.6388 ms. Experimentally, isentropic expansion of helium at T_0 = 319.0 K and P_0 = 9.60 MPa with the short-term stability in source temperature of ± 50 mK only affects the mean terminal flow velocity by ± 0.14 ms^{-1}; for a flight distance of 3.000 m this corresponds to a scatter of ± 126 ns in the mean arrival time, equivalent to a spread around 7 × 10^{-5}. For helium at very high stagnation pressures, from 0.60 – 9.60 MPa, the influence of pressure stability is negligible, because a variation of ± 10 kPa is expected to alter the mean particle speed only by ± 0.02 ms^{-1}.

3.4.2 Experimental Results to Theoretical Predictions

In combination with the quasi-equilibrium condition, these results from pulsed high pressure jets with high signal intensity and optimum repeatability offer suitable parameters of source operation, which are consequently applied to the high-resolution experiments of atomic, molecular, and the cluster beams.

By using a tunable translator stage with a tolerance of 50 μm, the time-resolved MCP detector is able to record the arrival time of excited particles according to the very precise flight distance. Figure 3.4-1 shows a clear linearity of the mean time-of-flight versus the position of the detector with equal distance. The numeric regression of all measurements gives a slope and an intercept, which represent the terminal velocity of $\langle v \rangle$ = 1825.0 ± 0.2 ms^{-1} and the constant flight distance of l_c = 2883.0 ± 1.1 mm, respectively. This ultra-precise velocity of particles can be distinguished from either the theoretical prediction for the isentropic jet expansion of an ideal gas of 1820 ms^{-1} or the value of 1831 ms^{-1} calculated using a real gas EOS, which will surely not be resolved if the velocity resolution is larger than 1%.

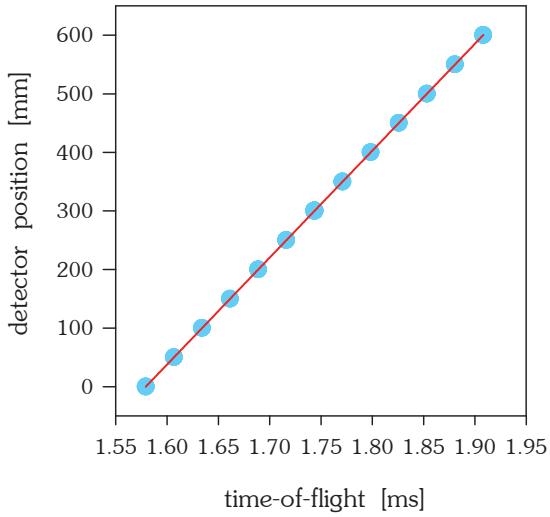

Figure 3.4-1 Linear dependence of mean flight time to the elongated flight distance with 50.0 µm interval (ensured by a linear translator). The numeric regression shows a slope of 1825.0 ± 0.2 ms^{-1}, which derives a precise terminal velocity of He^*. Also, the intercept of 2883.0 ± 1.1 mm represents a "real" distance between the place where He was electronically excited in the early stage and the MCP detector.

When we extend the source condition over a large temperature range, T_0 = 228.0 – 410.0 K, and repeat the same procedure to find the quasi-equilibrium region. The output velocities within this range fit to the theoretical predictions, see Figure 3.4-2. In the end, the experimental result of velocity implies that the helium clusters might exist even at elevated source temperatures because all experimental result of velocities are slightly higher than ideal gas model and tend to calculation from the real gas EOS. This interpretation is in good agreement with the result in the previous section, where the He_2^+ (m/z: 8) signal has been found by the QMS.

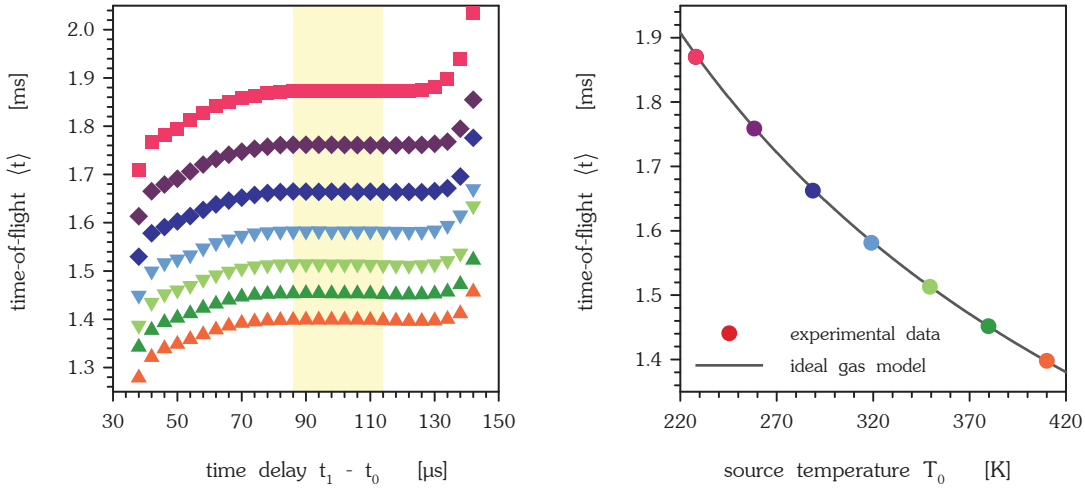

Figure 3.4-2 Comparison of theoretical predicted ideal gas velocity to the experimental helium terminal velocity.[49] (*left*) Probing the stable TOF region by "beam scan" in 1 µs step for source temperature of T_0 = 228.0 – 410.0K. (*right*) Good agreement to the ideal gas liked helium. All source pressures are fixed at 9.60 MPa, the experimental uncertainty is smaller than the size of the symbol.

3.5 Conclusions

In this chapter, to put it briefly, a comprehensive study of a dense helium jet is discussed. The combination of a state-of-the-art machine and careful statistical analysis, these up-to-date experiments of the exemplary helium beam system has demonstrated many new insights:

(1) Constant signal intensity from the expanded particles in the beam doesn't mean an equilibrium status. The steady-state condition is only available if the energies of those particles are the same. In other words, the terminal velocity and velocity spread should be constant in addition to the maximized intensity. The advanced control of these strict criteria confirms a quasi-equilibrium segment in a sufficient long pulse.

(2) The placement of skimmer strongly affects the beam's translational cooling. A trade-off of generating a colder beam and having high signal intensity, that is, good transmission of particles from the skimmer, should be considered with respect to the experimental need. At given source temperature and pressure, the translational cooled helium beam is improved from $T_{\parallel}$ = 120 mK to 4 mK by varying the distance between the nozzle and first skimmer from 143 mm to 233 mm.

(3) For a helium gas expansion, a promoted quasi-continuous segment in the pulsed beam with diminished interference allows the formation of weakly bound helium clusters, even at the source temperature of T_0 = 410 K.

(4) The ultra-precise velocity determination of helium beam differentiates the experimental results from the theoretical velocity of ideal gas expansion. Also, the small difference in velocity, which is only 0.3%, between the experimental result and the prediction from real gas EOS prompts the application to move forward to the carbon dioxide (CO_2) system.

CHAPTER 4

4 $(CO_2)_N$ Clusters Scattered off $Si(111)/SiO_2$ Surface

Cluster growth in the gas phase is an important issue for modern science and technology, because the condensation process of supersaturated gases is relevant to the fundamental research topics of molecular physics and atmospheric chemistry, while parameter control of particle size is essential to the development of nano-materials and semiconductor manufacturing.[17,46,133-136] Environmental engineering, on the other hand, also strongly requires sensitive analysis to examine all kinds of small particles relevant to air pollution. Despite the fact that many studies focusing on the aggregation of gas phase clusters as a consequence of the strong cooling process during supersonic jet expansions, only a few studies touch the macroscopic condensation progression in regard to the real fluid properties from the source.

To control the size distribution of clusters by jet expansion, Hagena's empirical scaling law expresses the effect of mean cluster size as a function of source geometry, source temperature and source pressure.[18] Commonly, the latter two physical parameters define the initial density or entropy of the working fluid and subsequently affect the collision probability during the expansion. When the beam starts at low density as gas expansion, the clusters are aggregated proportional to the number of particles in the beam, meaning that the terminal size of clusters can be referred to the source density. On the other hand, Henne *et al.* present another size distribution model of the clusters via liquid jet expansion.[105] These clusters are fragmented from large droplets, so the surface tension of droplets and also the size of a nozzle exit are relevant. That is to say, the formation channel of clusters, either condensation from the gas phase or fragmentation of a liquid phase, defines different size distributions and should be identified to improve the prediction of cluster growth.[137]

Northby *et al.* have suggested that the source entropy defines the mass distribution of fragmentation clusters from supercritical expansions of He^4 regardless of the specific pressure or temperature.[137] According to their supercritical expansion experiments, two distinct cluster groups were found, but only the larger-cluster group was used to correlate to the source entropy. "It is not clear why both types coexist in a range of temperatures." stated Northby *et al.*[138] Therefore, the aim of this project is to correlate the isentropic expansion path to the terminal cluster size distribution and further extend to resolve cluster formation channel from high source densities.

In order to expand the existing knowledge to molecular clusters, besides the few results from CO_2, SO_2, $CFCl_2$ and H_2O clusters scattering off different surfaces,[139-142] it is necessary to systematically investigate a representative model. In past years, Christen *et al.* focused on the CO_2 expansion from sources with high densities, for example, the rapid expansion of supercritical carbon dioxide (*sc*-CO_2). They not only recorded pronounced

molecular beam velocity change at high pressures,[113,143] but also pointed out very small translational temperatures of $(CO_2)_N$ clusters from the terminal arrival time distribution. As a result, the final status of $(CO_2)_N$ clusters seems to be strongly influenced by the source properties. For the applications of supercritical CO_2, these physical properties at such high density are essential to global atmospheric issues, food production and pharmaceutical industries.[144-146]

Herein, these previously obtained results prompt me to use the chemically inert CO_2 - with comprehensive source conditions as a touchstone - subsequently impacted on a crystal surface. The object of surface scattering is to collect the fragmented monomers after collision, which can be track back to better understand the incident $(CO_2)_N$ clusters. For instance, the terminal $(CO_2)_N$ cluster temperature can be derived by the isentropic process with respect to the initial source condition.[49] At the end, the cluster formation is directly linked to the source entropy of working fluid from the very early stage, which is not only affected by the widely commented source density.

4.1 Temperature of Clusters Generated from Gas to Supercritical Conditions

The experimental realization of highly accurate source conditions, in combination with an undisturbed flight path of precisely known length, reliably permits the generation of intense supersonic beams with a remarkably well-characterized axial velocity distribution.[49,50,106] Here, this achievement is used for a systematic investigation of condensation during the jet expansion of pure CO_2. The mean velocity of carbon dioxide is studied in great detail from medium to high pressures and sub- to supercritical temperatures, employing a generic thermodynamic model and a comprehensive equation of state.[147-149] Enthalpy changes (ΔH) of the working fluid can be obtained from the mean terminal flow velocity, $\langle v \rangle$.

$$\langle v \rangle = \sqrt{\frac{2\Delta H}{N_A m}}. \qquad (4.1.1)$$

Here, N_A is the Avogadro constant and the m is the atomic/molecular mass (in amu). It also permits an estimate of the mean temperature of larger clusters in supersonic beams. The detailed thermodynamic modeling permits for the deciphering of the 'provocative' velocity distributions of jet expansions of supercritical CO_2 reported earlier,[143,147] confirming recent theoretical predictions of high-density jet expansions: Close to the phase boundary solid CO_2 clusters are generated both from the gas and the liquid phase.

4.1.1 Cluster Temperature and Translational Cooling: $(CO_2)_N^+$ clusters

By utilizing the advanced source control from the last chapter, the CO_2 jet expansion is expected to result in a precise terminal velocity from the steady-state condition. However, a modification of this experiment is required. Aiming to observe the arrival time distribution of $(CO_2)_N$ clusters from MCP detector, an electron source with ionization energy of 80 eV is used to ionize the $(CO_2)_N$ clusters for 2.5 μs. The ionized $(CO_2)_N^+$ clusters were accelerated by electric field to gain sufficient energy and subsequently generate signal on the

detection side. The rest of the non-excited $(CO_2)_N$ clusters normally do not contain sufficient energy to generate the signal from MCP detector. However, the extreme high source pressure in this experiment and Even-Lavie type nozzle with trumped shape seems to generate very large $(CO_2)_N$ clusters, surprisingly, which can even be measured by MCP detector without further excitation.

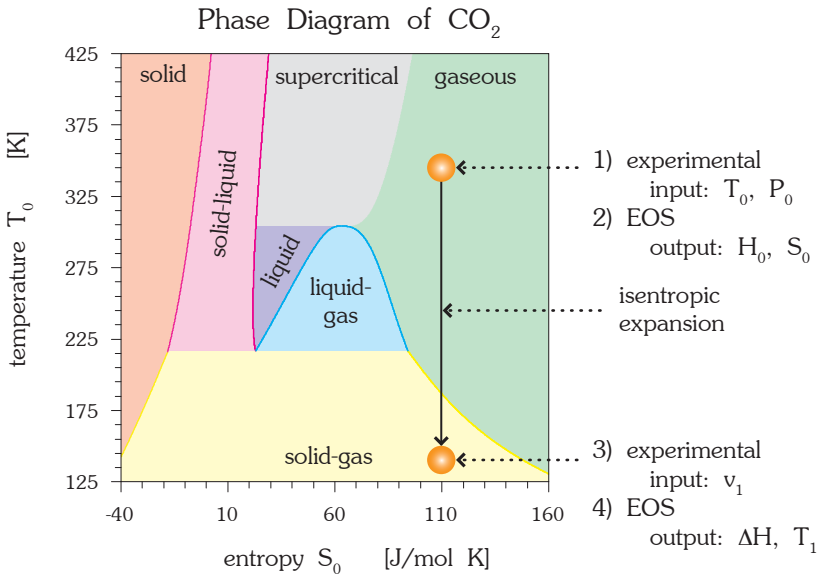

Figure 4.1-1 Macroscopic *T*–*S* diagram of carbon dioxide, which is based on the combination of an EOS for the fluid phases and for the solid phase.[148,149] The imaginary isentropic expansion is depicted at the right side as an arrow. This vertical arrow indicates the initial entropy (S_0) and enthalpy (H_0) from the top via energy transfer to the bottom of the final status, which allows us to use a thermodynamic method to determine the terminal beam (and cluster) temperature (T_1) and enthalpy (H_1).[49]

We first start with the evaluation of ionized $(CO_2)_N^+$ clusters because those "tagged" particles represent only the quasi-equilibrium segment in the entire beam, which is necessary for the calculation in thermodynamic equation of state (EOS). Assuming an initially isentropic expansion process, in Figure 4.1-1, the EOS of the supersonic beam can be deduced from the enthalpy change of the working fluid as following steps:

(1) The initial enthalpy of working fluid is defined by precisely controlling the source pressure, P_0, and the source temperature, T_0.

(2) Apply the EOS to calculate the thermodynamic quantities such as stagnation enthalpy, $H_0(P_0, T_0)$, and the stagnation entropy, $S_0(P_0, T_0)$, for a reversible adiabatic process during jet expansion into vacuum. This expansion process is also known as the isentropic process, where the $\Delta S = 0$.

(3) The transformation of internal energy from source enthalpy to the kinetic energy from terminal beam velocity, $\langle v \rangle$, can be precisely determined by the time-of-flight spectrum.

(4) Using Eq. 4.1.1 to determine the change in enthalpy, ΔH, and further to define the final enthalpy, $H_1 = H_0 + \Delta H$; with H_1 and S_0, the EOS can provide the desired physical property: mean beam temperature $T_1(H_1, S_0)$.

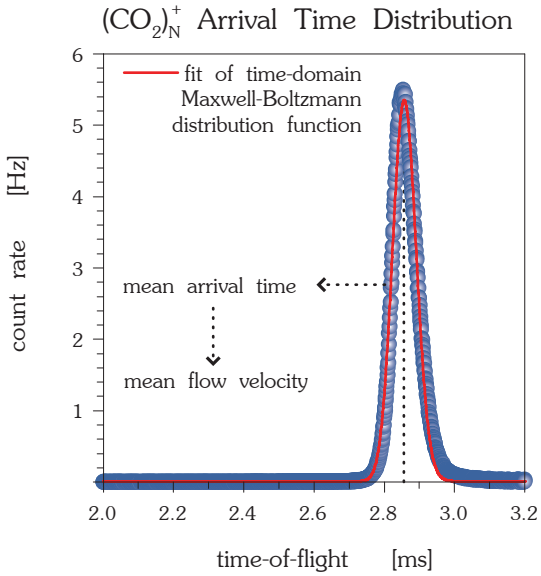

Figure 4.1-2 A typical time-of-flight spectrum of ionized $(CO_2)_N^+$ beam, which is fitted by a Maxwell-Boltzmann distribution. The beam was originally ionized by an electron source for 2.5 μs near the exit of the nozzle. The fitted mean arrival time can be converted to the mean flow velocity according to the flight distance.[150]

Figure 4.1-1 shows the concept of isentropic expansion journey in a CO_2 *T*–*S* diagram; the possible "final temperature" can easily be seen in this thermodynamic map. The source condition is then carefully calculated and set according to the simulated journey of isentropic process, from S_0 = 55 – 105 J/mol K. After recording the arrival signal with respect to the time scale, see Figure 4.1-2, a flight-time (t) dominated Maxwell-Boltzmann distribution for a flux sensitive detection is used to evaluate the recorded data[99]

$$f(t, t_F, d)\, dt = d\frac{l^3}{(t - t_F)^4} exp\left[-\left(\frac{\frac{l}{(t - t_F)} - v_1}{\Delta v}\right)^2\right] dt\,, \qquad (4.1.2)$$

parameter d gives a scale factor related to the signal intensity along the expansion axis. Here, the mean arrival time $\langle t \rangle$ is given by t_F and the Δv represents the width of the peak. And, a field-free flight distance, l, is applied to derive the mean terminal beam velocity, $\langle v \rangle$.

As a result, in Figure 4.1-3, all the velocities are plotted in regard to the source entropies.[151] At constant entropy, when S_0 = 90 J/mol K, higher source temperature (T_0 = 410 K) results slightly lower mean beam temperature (T_1 = 135 K) than lower source temperature (T_0 = 235 K to T_1 = 142 K). If we compare different source entropies, the lower the source entropy results in lower mean beam temperature: S_0 = 70, 65, 60 and 55 J/mol K to T_1 = 134, 129, 124 and 117 K, respectively.

In the literature, the infrared absorption measurements of $(CO_2)_N$ clusters show temperature of $T \approx$ 135 K,[5] which is in a good agreement with our result. The overall results from the comprehensive source conditions seem to end up with the mean beam temperature of

$T_1 \approx 138$ K, the independence implies that the terminal cluster temperature might related to the evaporation cooling from the surface of the $(CO_2)_N$ clusters. This evaporation cooling can also be experimentally measured by a thermocouple attached to a dry ice (solid CO_2), see Figure 4.1-4. When the chamber is evacuated, the surface temperature of dry ice decreased to $T \approx 150$ K at a low background pressure of $P \approx 100$ Pa. This result is also comparable with the theoretical sublimation temperature of bulk solid CO_2.

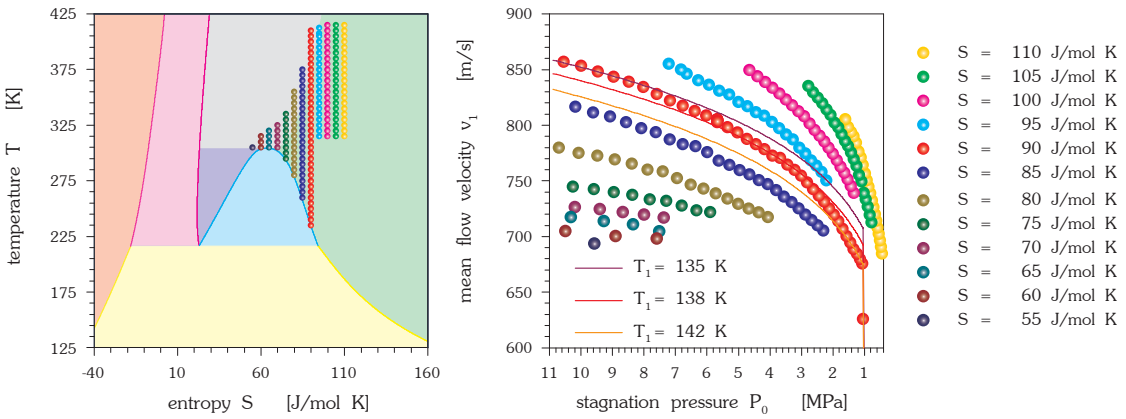

Figure 4.1-3 (*left*) Schematic visualization of the source conditions in temperature versus entropy, the entropy here is calculated by the combination of source temperature, pressure and an EOS for the fluid phases and for the solid phase.[148,149] (*right*) The terminal mean flow velocity with respect to the source pressure is depicted with different colors, where the higher pressure reflects higher temperature at given entropy. By using the thermodynamic EOS in combined with source temperature (T_0), source pressure (P_0) and beam velocity (v_1), as an isentropic process (e.g., S = 90 J/mol K, red dot), the terminal beam temperature (T_1) can be numerically derived to the red line (T_1 = 138 K). Here, the best fit for lower pressure region is given by T_1 = 142 K and T_1 = 135 K for higher pressures.[150] The experimental uncertainty is smaller than the size of the symbol.

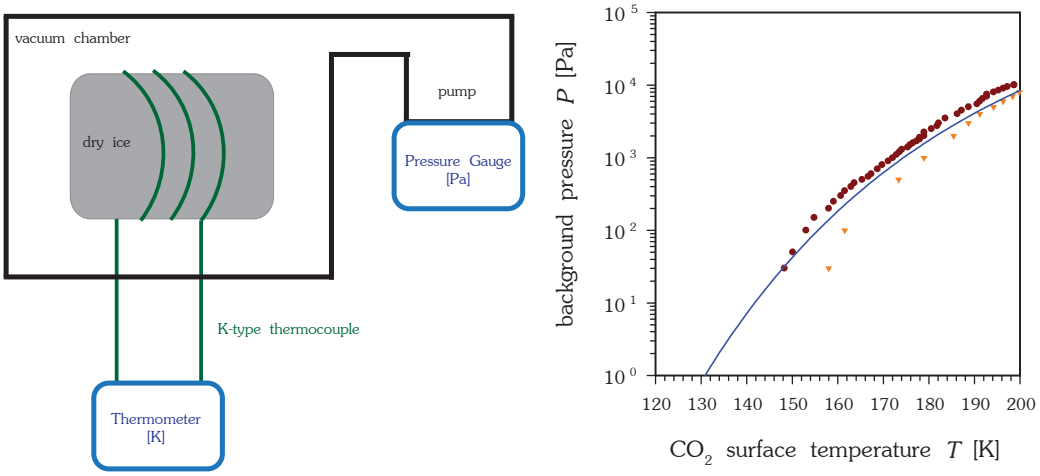

Figure 4.1-4 The sublimation temperature of isolated dry ice (solid CO_2). (*left*) The experimental setup of a dry ice wrapped by a K-type thermocouple, which is located in a closed chamber, which can be evacuated by a diaphragm pump. (*right*) The measured surface temperature of dry by two different processes: evacuation or pumping out (yellow triangle) and evaporation from low background pressure (brown circle) as a function of the background pressure. Two series of data are in good agreement with the bulk model from the Chemical Engineering Research Information Center, South Korea.[152]

In short, according to the comprehensive source conditions of CO_2 in this study, the macroscopic description of jet expansion holds even for the mean cluster sizes as small as $\langle N \rangle \approx 10^3$ (estimated by the Hagena's empirical scaling law in section 2.3.3 according to the source conditions of T_0 = 325 K and P_0 = 0.51 MPa, where S_0 = 110 J/mol K), which results in solid-gas phase.

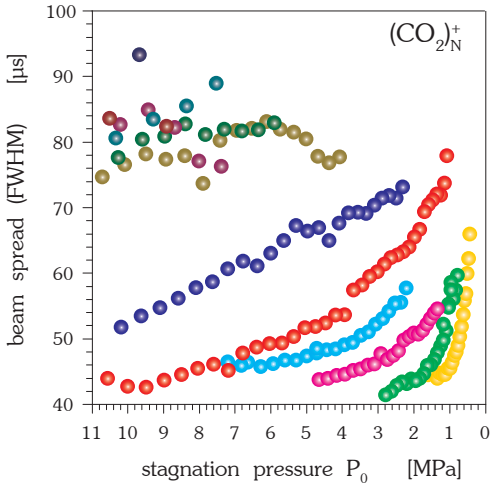

Figure 4.1-5 Peak spread of the ionized $(CO_2)_N^+$ beam, which was originally ionized by an electron source for 2.5 µs near the nozzle exit. At given source entropy larger than S = 85 J/mol K, the higher source pressure and source pressure result narrower spread in full width of half maximum (FWHM). When the source entropy is lower than S = 80 J/mol K, the peak spread is independent of the source pressure (P_0). The lowest source entropy results from the broadest peak in the end, which indicates the least translational cooling during the expansion process.[150]

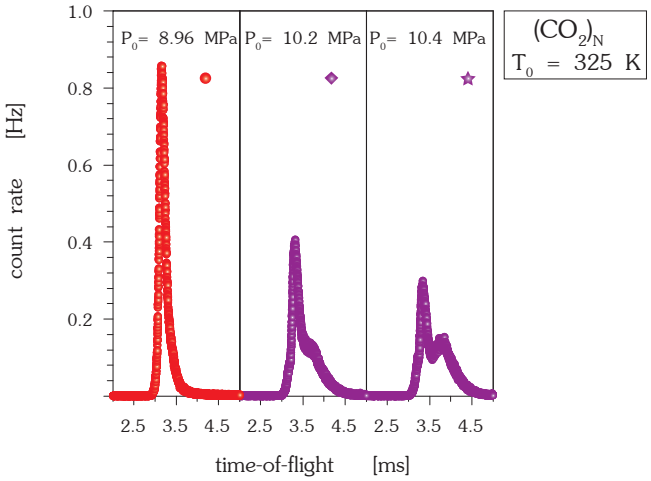

Figure 4.1-6 Depicted three time-of-flight spectra of neutral $(CO_2)_N$ beam, which are directly measured by the MCP detector without further electronic excitation.[153] At source temperature of T_0 = 325.0 K, the peak shape changes as the source pressure increases from P_0 = 8.96 MPa to 10.40 MPa. The emerged second peak (star shape) implies the partial condensation of CO_2 already happened during the jet expansion in the nozzle, where the larger liquid droplets arrive later at the detector.[150]

Another fitting term, Δv, represents the width of the peak can be transformed to the beam spread in FWHM, see Figure 4.1-5. As a direct indicator of the translational temperature, at higher entropies, the translational cooling increase with pressure. At lower entropies, the beam spread is largely constant, meaning that the translational cooling is limited by the partial condition.

4.1.2 Bifurcation of TOF Spectra at Higher Source Densities

It is known that the ionization process leads to degradation of mean cluster sizes and charge repulsion of ionized clusters in the molecular beam system.[130,154] Therefore, the result of detected cluster size and the determination of a beam velocity might be slightly affected by this method. In order to soft ionize the fragile sample, the CI, FI, ESI, and MALDI were developed to reduce the fragmentation. However, a detection of directly measure the neutral particle is always a challenge for analytical sciences. Here, a series of unexpected signal from non-excited $(CO_2)_N$ clusters is presented, the resulting spectra directly show velocity distributions of $(CO_2)_N$ clusters in the jet with the least perturbation.

Figure 4.1-6 depicts the arrival time distribution of $(CO_2)_N$ clusters from three different pressures at source temperature of T_0 = 325.0 K. The clear difference in peak shape demonstrates the velocity bifurcation at very high source pressure, especially when the source condition close to the critical point. That is to say, at higher source densities, the CO_2 jet expansion result two branches of $(CO_2)_N$ clusters: fast/narrow/high intensity and slow/broad/low intensity. According to the supposition of isentropic process, again, in the *T*–*S* diagram, the expansion of high-density jet is going to pass the liquid-gas phase boundary. Thus, these two branches of $(CO_2)_N$ clusters might analogy to the formation via vapor (fast/narrow/high intensity) and liquid (slow/broad/low intensity). In short, a partial condensation might happen during the jet expansion. This hypothesis will be further verified in the next section by time-resolved surface scattering method.

4.1.3 Source Condition to The Cluster Size

A higher source density is usually assumed to generate larger mean cluster size in the molecular beam, however the “larger mean cluster size” might be numerically broken down to either “formation of few extreme large clusters and some remaining smaller clusters” or “more large clusters with similar sizes”. When comparing the intensity of the ionic signal, $(CO_2)_N^+$ clusters, with the neutral signal, $(CO_2)_N$ clusters, at isothermal source conditions, we found an interesting contrast. The $(CO_2)_N^+$ signal decreases as the source pressure, P_0, increases, while the $(CO_2)_N$ signal shows a reverse tendency except at the extreme high-pressure region, see Figure 4.1-7. In order to understand this contrast, the question then arises: Are there more clusters with modest size or larger clusters with limited numbers from the high-density jet expansion?

According to the Hagena’s empirical scaling law, the mean cluster size is going to rise when the source pressure increases at given temperature. Figure 4.1-7 demonstrates this tendency by applying Eq. 2.2.10–12 from section 2.2.2. In principle, a defined source

density divided by the final mean cluster size results in the number of clusters in average, n_c. This number density parameter can be derived from the real gas (CO_2) source particle density from thermodynamic EOS, see the lower row of Figure 4.1-7. As a result, the number density (n_c) seems to be coherent to the $(CO_2)_N^+$ signal, meaning that the ionized $(CO_2)_N^+$ clusters were counted by the MCP detector regardless of the size. On the other hand, the $(CO_2)_N$ signal directly reflects the growth in cluster size as predicted by Hagena *et al.*[18,100] The inverse decay at high-density region may directly relate to the partial condensation during the expansion, because the slow/broad/low-intensity contribution of clusters from the liquid contains less kinetic energy for being detected.

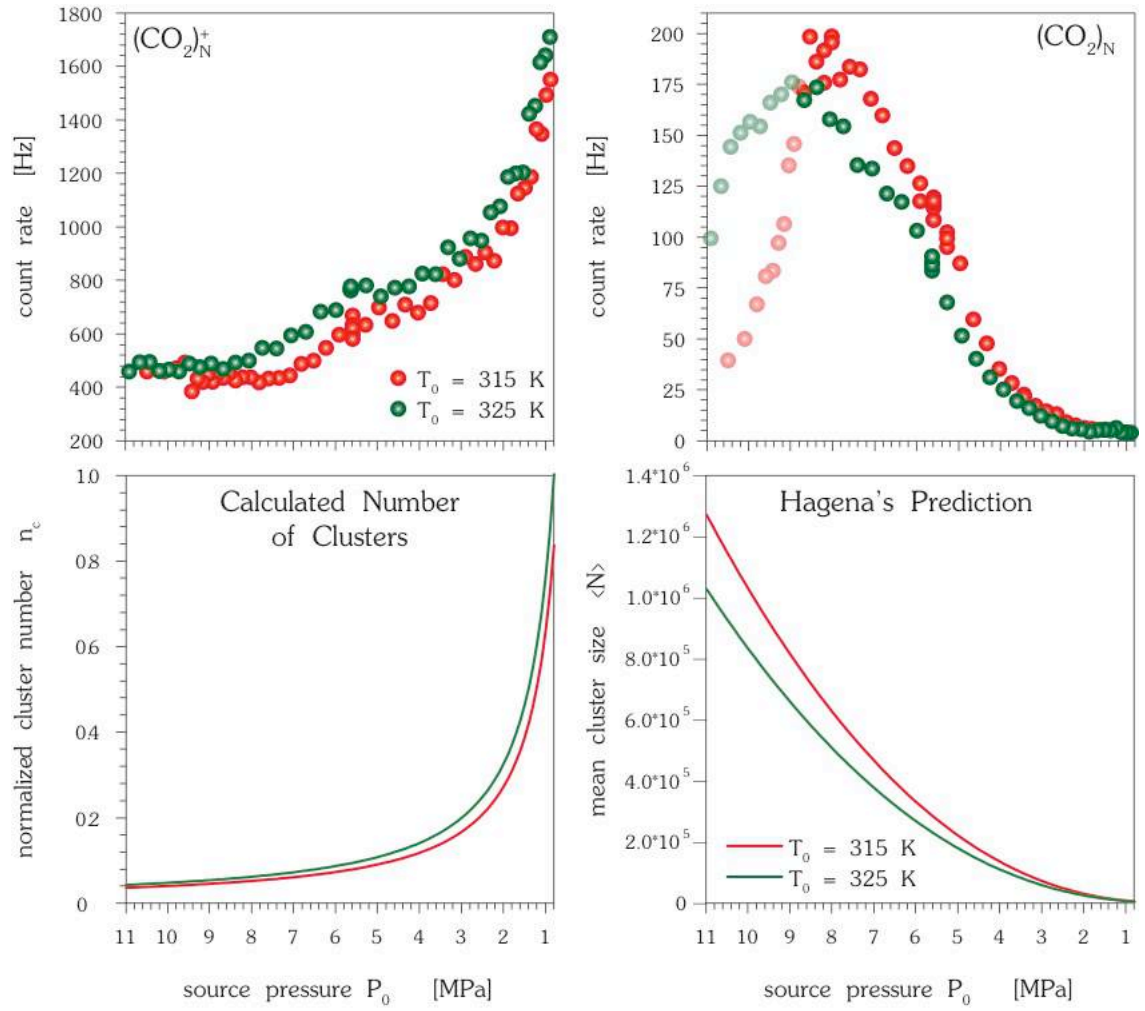

Figure 4.1-7 The upper row displays signal intensity of ionic $(CO_2)_N^+$ peak (*left*) and neutral $(CO_2)_N$ peak as a function of source pressure (P_0) at given source temperature (T_0) of 315.0 or 325.0 K.[151,153] At the lower part of the graph, the number of clusters (*left*) and the mean cluster size (*right*) are calculated by Hagena's empirical scaling in combined with real gas EOS.[104,107] In particular, the number of clusters is the source density divided by the mean cluster size.

To sum up in this section, the dependence of the mean flow velocity, $\langle v \rangle$, on source pressure P_0 and temperature T_0 is surprisingly well accounted for by a generic thermodynamic description using real fluid enthalpies. For high resolution measurement of charged clusters, $(CO_2)_N^+$, the combination of the most advanced equations of state for

fluid and solid phases opens up the possibility to derive the mean temperature, which is $T_1 = 138 \pm 4$ K. This value is largely independent of source conditions, suggesting that the mean cluster temperature is determined by evaporate cooling.

For neutral clusters, $(CO_2)_N$, a second peak in the time-of-flight spectra emerges around the gas-liquid phase boundary. It can be seamlessly explained by partial condensation already within the valve, resulting in solid clusters from the vapor phase (faster particles) and the liquid phase (slower particles). In the last part, the pressure and temperature dependence of Hagena's scaling law in mean cluster size appears to deviate from the experimental result at lower entropies ($S < 85$ J/mol K).

With the intention to understand the relation between the source entropy and cluster size, a consistent method of surface scattering is used to reflect the impacting cluster size from various source conditions. The angular distribution of the scattered particles offers two important parameters, direction (angle) and spatial spread (exponent term), to unravel the cluster contribution from the incoming beam.

4.2 Initial Entropy and Cluster Formation Channels

Employing a pulsed high-pressure supersonic jet expansion and a dedicated setup for the experimental investigation of chemical processes occurring between neutral, van der Waals bound clusters and a solid surface, we report on the angular distribution observed for large $(CO_2)_N$ clusters scattered off a Si(111)/SiO_2 surface under ultrahigh vacuum conditions.

To analyze a series of clusters in a broad range by a consistent method, scattered particles from surface collisions portray the continuous change in cluster sizes from a few hundred up to a million molecules. The comprehensive size information of $(CO_2)_N$ clusters from scattered angles can assess the limitation of Hagena's empirical scaling law, which has been widely compared to the size measurements from various analytic methods. For instance, the available optical methods provide a non-destructive way (e.g. IR spectroscopy, electron diffraction, Rayleigh scattering) to determine the size of ~ 10^3 to ~ 10^5 atoms/molecules per cluster. Also, the quadrupole mass spectrometer gives the size of daughter ions up to a cluster size of ~ 10^3.

Therefore, the presented studies cover comprehensive source conditions from gas to supercritical to liquid jet expansions, which generated clusters from a few angstroms to tens of nanometers.[150] The focus is on the influence of source entropy, realized by accurately setting source pressure and temperature. These new experimental results for the scattering of $(CO_2)_N$ clusters off Si(111)/SiO_2 surface were recorded at different incident angles between 0° to 90°. Two channels of clusters have been separated by time-resolved spectra from the quadrupole mass spectrometry.

4.2.1 Result: Time Dependent Angular Distribution

By rotating the surface manipulator and switching the mass-to-charge ratio (m/z) from the QMS, the angular distributions with respect to scattered monomer CO_2^+ (m/z: 44) were recorded. For pulsed supersonic beams, the intensity of particles often derived from either the integrated signal or the amplitude of measured signal from a time-of-flight spectrum. The time scale in the spectrum is thus a crucial parameter in the data evaluation. Although most of the atomic/molecular beams seemed to be homogeneous within the short pulse by the ideal valve driver, several reports have recently demonstrated the heterogeneity for different time segments of the detected signals.[50,155] To avoid the oversimplification by the integration of signal, one needs to carefully analyze the signal distribution of each spectrum.

Take Figure 4.2-1 for instance, this angular distribution is taken from the integrated signal in the time period of t = 2.0 – 10.0 ms. These data points can be fitted by two cosine functions with exponent terms, which gave a least squares fitting quality of R^2 = 0.995. In other words, the preliminary results might suggest two channels of this angular distribution: one contribution directs to 56.8° with a larger exponent of 154.2 and another contribution directs to 62.6° with a smaller exponent of 5.7. (Detailed method of numerical analysis has already been discussed in section 2.1.4, therefore we only report the output numbers in this chapter.)

However, if we look at its time-dependent plot of the angular distribution in Figure 4.2-2 (*left*), the margin of the arrival time of 5.0 ms has clearly separated the contour plot to two islands. When we again use two cosine functions with exponent terms to fit these two time periods independently, altogether four contributions were finally depicted in this scattering map, see Figure 4.2-2 (*right*).

By considering the time correlation, both early and late period have one relative narrow channel plus one broad channel. When this result is compared to initial evaluation of the entire spectrum (with only two channels), as mentioned in last paragraph, the two contributions from the early time period are finally emerged and can be separated by this careful consideration.

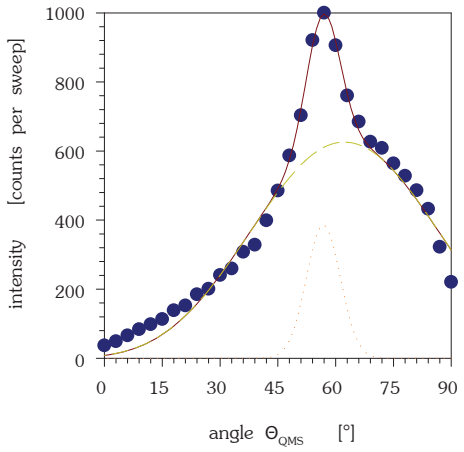

Figure 4.2-1 At given source temperature of T_0 = 305.0 K and P_0 = 10.90 MPa, the signal intensity distribution of scattering CO_2^+ monomer (m/z: 44) to the different detection angle (Θ_{QMS} = 0° – 90°). The signal intensity is the integrated signal with respect to each spectrum over the arrival time period of 2.0 – 10.0 ms. This angular distribution is fitted by two cosine functions with exponent terms: Θ_{QMS} = 62.6° and 56.8°, cosine exponent = 5.7 and 154.2, respectively.

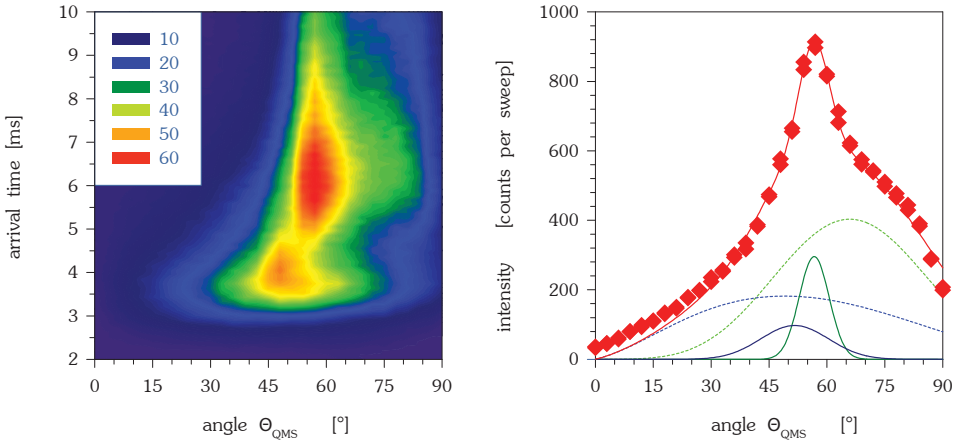

Figure 4.2-2 Source condition of T_0 = 305.0 K and P_0 = 10.90 MPa, the signal intensity distributions of scattering CO_2^+ monomer (m/z: 44) to the different detection angle (Θ_{QMS} = 0° – 90°). (*left*) Time coordinated contour plot. (*right*) Time resolved angular distribution, which is fitted by two cosine functions in two time segments, [2.5 – 5.0 ms]: Θ_{QMS} = 47.6° and 51.6°, cosine exponent = 2.7 and 42.2, respectively; [5.0 – 9.0 ms]: Θ_{QMS} = 65.9° and 56.8°, cosine exponent = 8.6 and 218.4, respectively.

This improvement of data evaluation with the consideration of time segment ensures all the channels we have assigned are all independent of each other in the following discussions, which is essential to verify the formation channel of clusters in the pulsed supersonic beam.

4.2.2 Relevant Source Condition: Entropy

The first series of angular distributions was obtained according to the isothermal condition at a source temperature of T_0 = 305.0 K with variable source pressures from P_0 = 0.20 up to 10.90 MPa. As shown in Figure 4.2-3, these six scattered monomer intensities were all plotted according to the time-dependency versus detection angles (Θ_{QMS}). Figure 4.2-4 demonstrates the fitting result of corresponding angular distribution. As mentioned earlier, those fitting curves were considered independently from two different time segments, 2.5 – 5.0 ms and 5.0 – 9.0 ms, which results single contribution at low pressures and up to four contributions at high pressures.

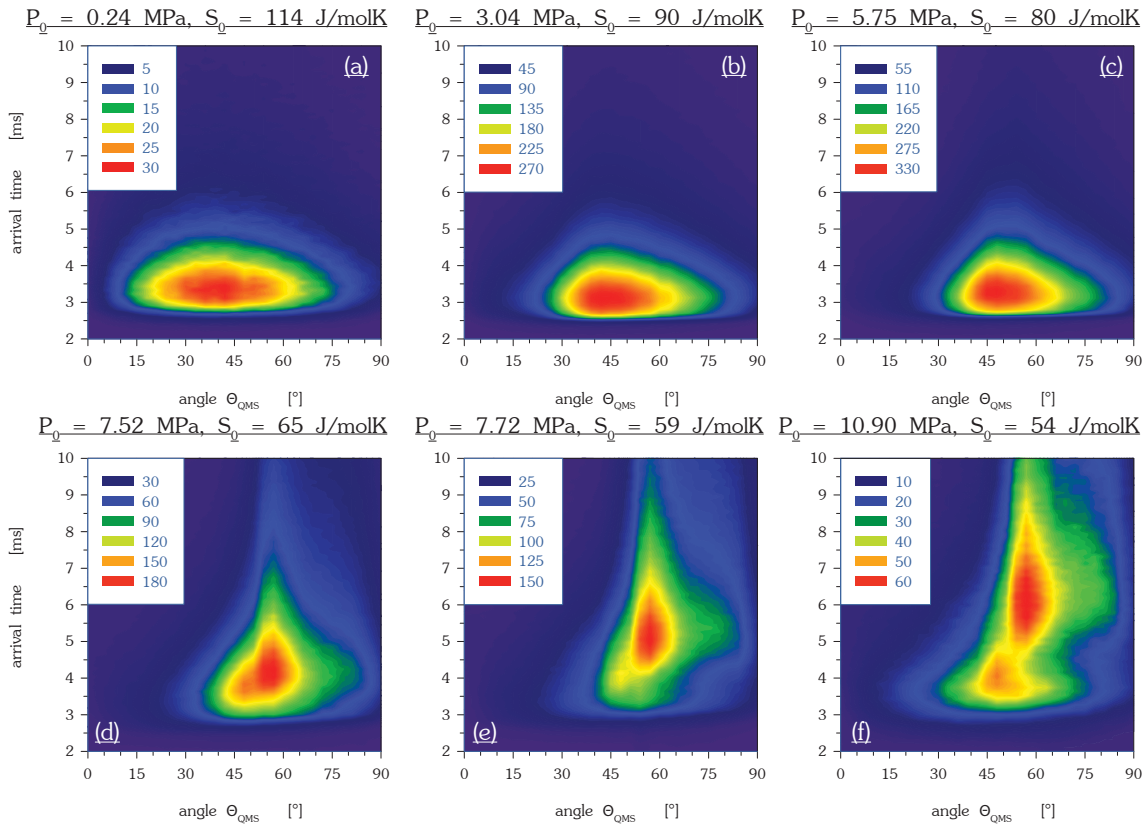

Figure 4.2-3 (a)–(f) the time-dependent scattering CO_2 monomer (m/z: 44) signal intensity contour plots according to the different complementary angle (Θ_{QMS} = 0° – 90°), from arrival time 2.0 to 10.0 ms by various source conditions at fixed source temperature of T_0 = 305.0 K.

Among these source conditions, the maximum scattering angles by raw data or fittings all locate between Θ_{QMS} = 32° – 67°, meaning that no trapping-desorption of CO_2 scattering off Si(111)/SiO_2 is observed (the simulated trapping-desorption channel shows a

$\Theta_{QMS} \approx 24°$, see section 2.1.4). In addition, both the scarcely signal intensity at $\Theta_{QMS} = 0°$ and the high values of exponent terms (2.5 – 200) from the cosine fitting confirm that no evaporative CO_2 were diffused along the surface normal from the surface with room temperature.

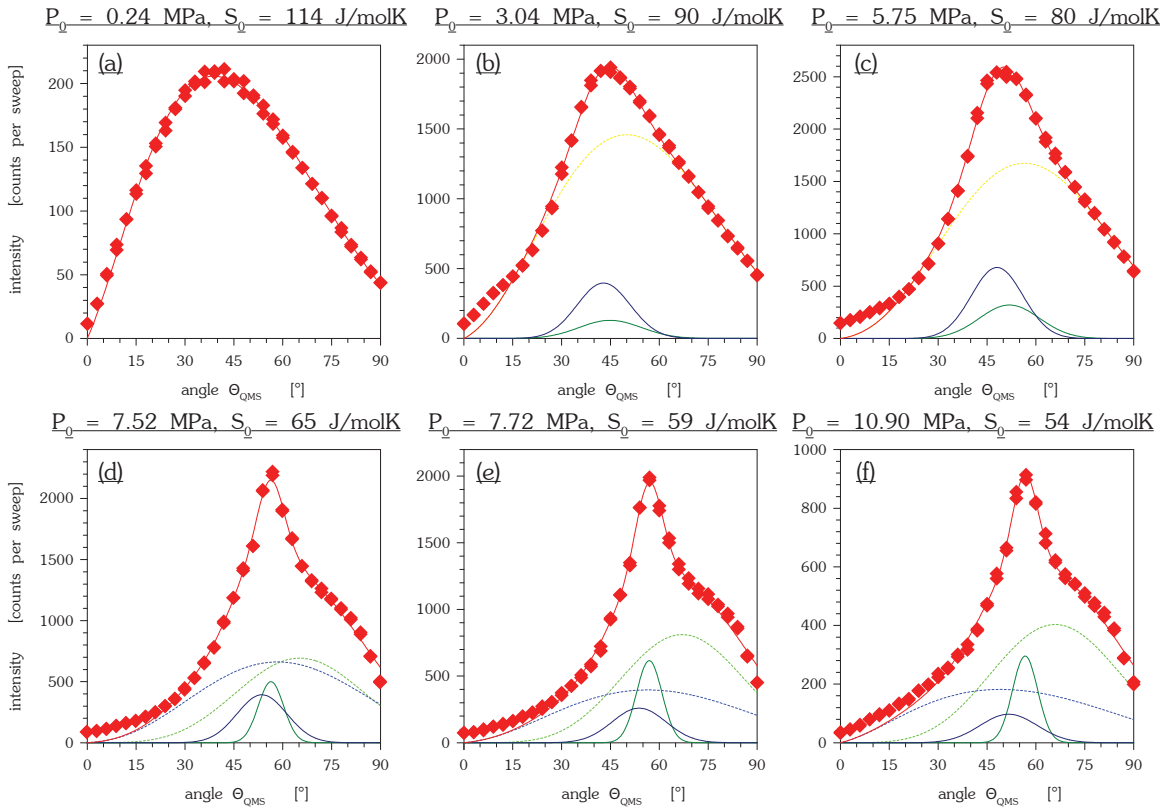

Figure 4.2-4 The integrated scattering CO_2 monomer (m/z: 44) signal according to the different complementary angle ($\Theta_{QMS} = 0° – 90°$) at fixed source temperature of $T_0 = 305.0$ K. All lines are the fitting results from cosine function with exponent term: (red) sum of all contributions, (blue) signal intensity from the time period of 2.0 – 5.0 ms, (green) signal intensity from the time period of 5.0 – 9.0 ms, (yellow) when the broader contributions from different time segments are identical, this fitted yellow curve represents the indifference signal intensity overall time period. The dashed line represents the broader contribution in certain time period. Here, the extra fitting function is added only if all the included parameters are passing the *t*-test to avoid the over-fitting, which is set at the p-value below 0.001 (one-tailed, d*f* = 31, this degree of freedom is rationalized by the experimental 3° interval over 90° range).

Earlier studies of cluster scattering have demonstrated that the scattering angle of outgoing particles increases accordingly to the increasing size of incoming clusters.[42,43,156] As expected, at fixed $T_0 = 305.0$ K, the maximum monomer intensities shift to larger angle when the source pressure increases, see Figure 4.2-4. Simultaneously, the exponent terms of the cosine fittings also become higher. Here, the higher exponent term at elevated pressures can be correlated to the narrower spatial spread of scattered $(CO_2)_N$ beam. To verify the role of source pressures in the scattering experiment, systematical studies of source temperatures from $T_0 = 310.0 – 325.0$ K were applied to investigate the angular change at given pressure.

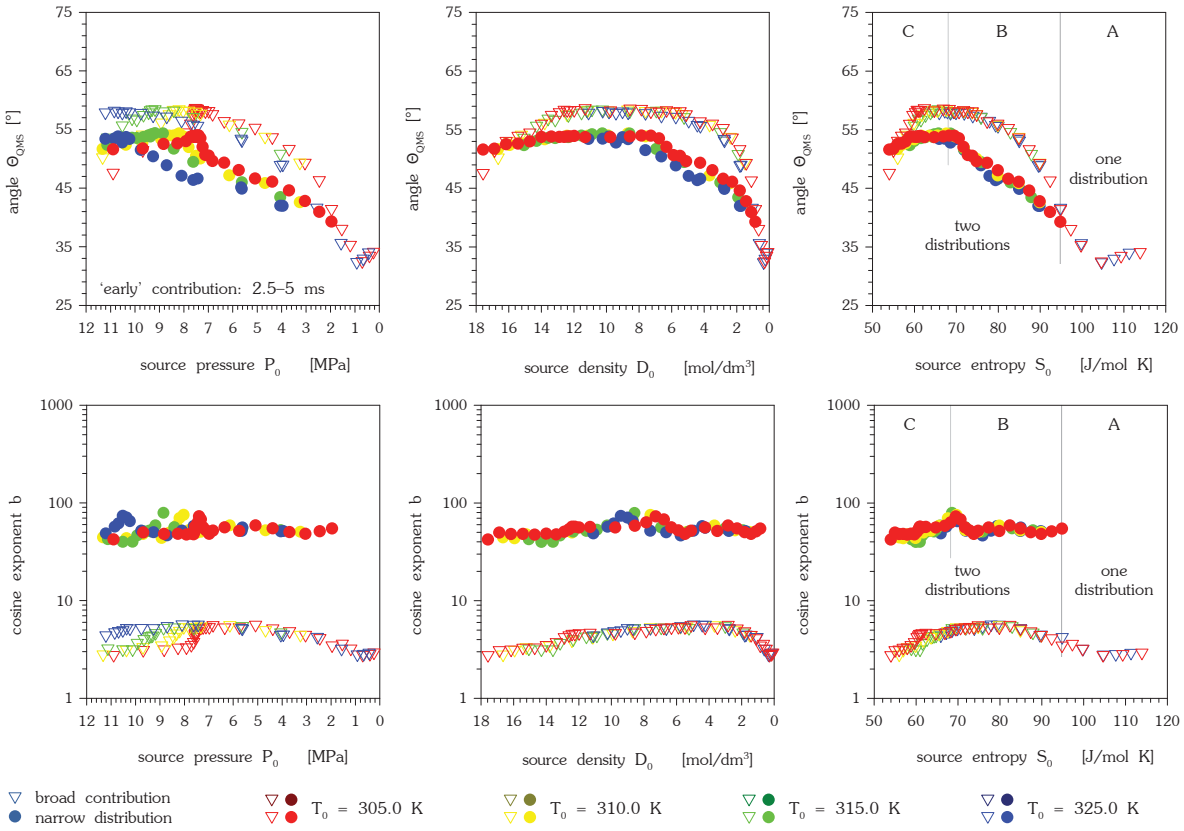

Figure 4.2-5 Data analysis of the $(CO_2)_N$ scattered off Si(111)/SiO_2, where the data points indicate all the experimental source conditions from T_0: 305.0 – 325.0 K with respect to source pressure (P_0), source density (D_0) and source entropy (S_0). (*upper row*) Signal analysis of scattered intensities based on the cosine fitting to CO_2 monomer (m/z: 44) from "early" time period [2.5-5.0 ms]. (*lower row*) signal analysis of angular spread based on the cosine fitting exponent to CO_2 monomer from "early" time period [2.5-5.0 ms].

In the *upper row* of Figure 4.2-5 and Figure 4.2-6, the overall scattering angles from a fixed source temperature behave similar to the results from other source temperatures but with a certain offset. For example, at T_0 = 305.0 K, the Θ_{QMS} moves toward larger angle when the source pressure increases to the pressure of ~ 7.2 MPa. Above this threshold, the Θ_{QMS} increases no more in both time period and even slightly decreases when the pressure is larger than ~ 9.6 MPa. This pattern can also be found at three other source temperatures: 310.0, 315.0 and 325.0 K, which result in three other thresholds in pressure of ~ 8.3, ~ 9.4 and ~ 10.6 MPa, respectively. In addition, this differentiation appears in the exponent terms as shown in the *lower row* of Figure 4.2-5 and Figure 4.2-6. In brief, the source pressure is not the proper factor to define the scattering distribution.

Another source property to be considered is the initial density, which strongly correlates to the collision possibility and further affects the cluster formation at the early stage of jet expansion. The combined source temperatures and pressures can be converted to the source densities by real gas EOS;[107] those adjusted plots of Θ_{QMS} and cosine exponent are shown in the *central column*. Surprisingly, all the trends are almost unified regardless to the source temperature. Only at the source density range of ~ 5.0 – 8.0 mol/dm^3, both fitting parameters (angle and exponent term) are slightly not match to each other. This outcome

infers that the status of CO_2 beam is not only determined by the number of source particles, but also should be related to the energetic property of each particle.

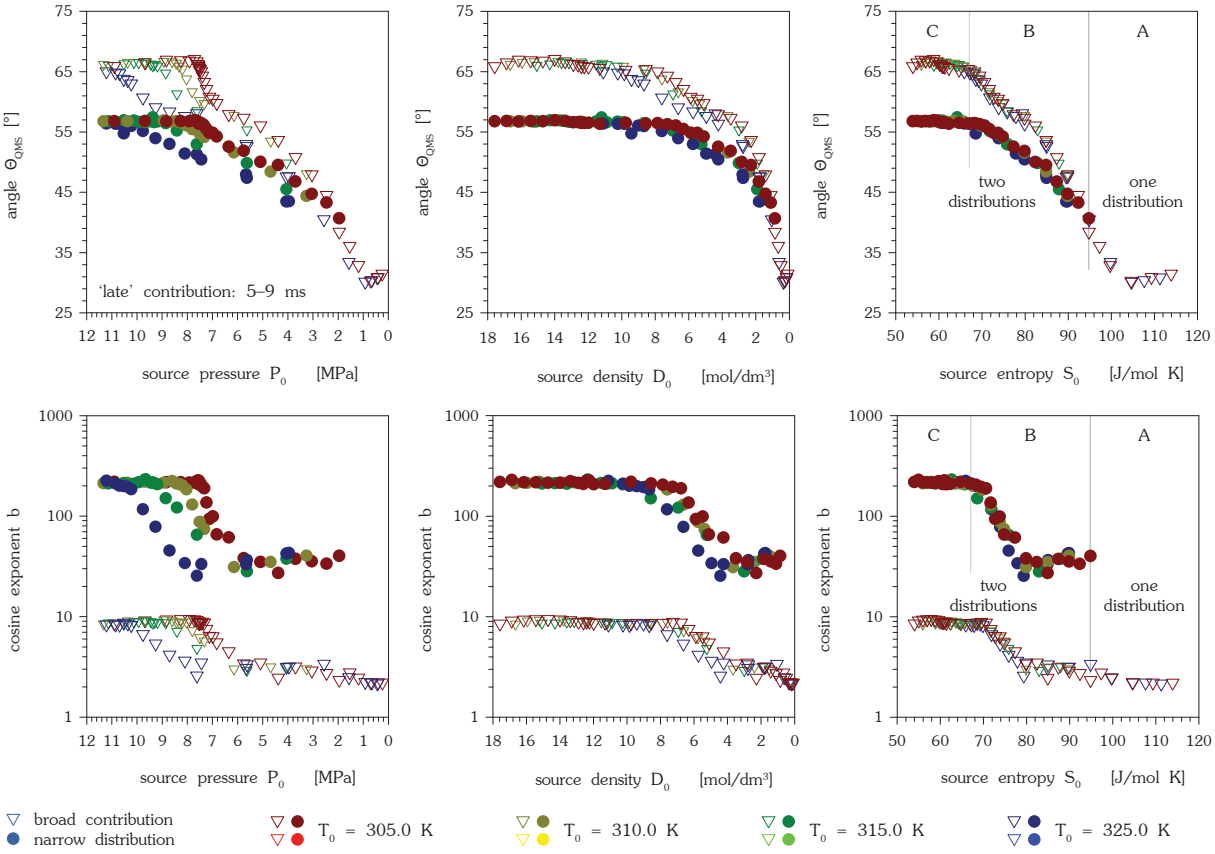

Figure 4.2-6 Data analysis of the $(CO_2)_N$ scattered off Si(111)/SiO_2, where the data points indicate all the experimental source conditions from T_0: 305.0 – 325.0 K with respect to source pressure (P_0), source density (D_0) and source entropy (S_0). (*upper row*) Signal analysis of scattered intensities based on the cosine fitting to CO_2 monomer (m/z: 44) from "late" [5.0-9.0 ms] period. (*lower row*) signal analysis of angular spread based on the cosine fitting exponent to CO_2 monomer (m/z: 44) from "late" [5.0-9.0 ms] period.

In view of the pulsed CO_2 beam undergoes reversible and adiabatic process in the Even-Lavie nozzle, which is well known as the isentropic expansion. Herein, we suspect that the source entropy could be the crucial parameter to influence the property of CO_2 beam.

Ultimately, the mean scattering angle (Θ_{QMS}) and the width of an angular distribution (exponent term) of detected monomers strongly dependent on source entropy. The *right column* of Figure 4.2-5 and Figure 4.2-6 demonstrate the coincidence of two scattering parameters regardless the scattered particles arrived at early or late time period. That is to say, in the system of a supersonic expansion, the macroscopic entropy of initial CO_2 fluid might primarily govern the terminal composition of the beam, e.g. the cluster formation.

4.2.3 Cluster Formation Channel

For the first time, a "three-stage" structure of angular dependency is observed in conjunction with source entropies. When the source entropy S_0 > 94 J/molK, only one contribution appears at smaller scattering angle and no separation of earlier and later time period is needed (the *t*-statistics and *P*-value test suggest rejecting the second cosine contribution for the fitting at the probability level of 10^{-3}). Although the maximum angles of outgoing particles slightly increases as the entropy decreases, in this range of entropy, the spread of angular distributions stays rather constant.

The next stage, for S_c (entropy at critical point) < S_0 < 94 J/molK, the maximum scattering angle increases as source entropy decreases, which indicates that the outgoing particles were scattered off and moved gradually closer to the surface. This shift, toward lower entropy, implies the mean size of incoming $(CO_2)_N$ is getting larger. Also, a noticeable difference at different time periods appears in the angular spread, where the cosine exponent term remains constant at earlier segments (2.0 – 5.0 ms) but rapidly raises at later segment (5.0 – 9.0 ms). This phenomenon can be related to the emergence of "slow" contributions in the contour plot of Figure 4.2-3.

In the third stage of source entropy, where S_0 < S_c, the maximum scattering angles and angular spreads decrease at the earlier time segments (2.0 – 5.0 ms) while they are both constant at the later times (5.0 – 9.0 ms). In short, this "three-stage" transition is directly related to the source entropy of CO_2. To better understand the transformation process from the initial status of CO_2 to the terminal $(CO_2)_N$ clusters, i.e. clustering, we introduce the macroscopic *T*–*S* phase diagram (Figure 4.2-7) to trace the expansion/clustering process.

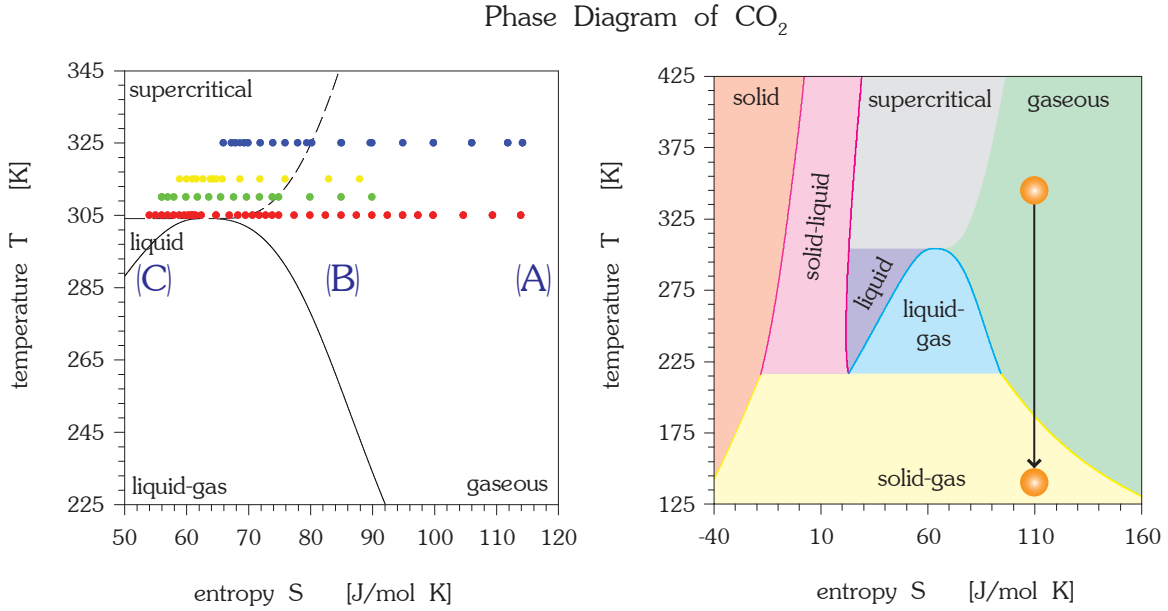

Figure 4.2-7 (*left*) Experimental source conditions versus the *T*–*S* phase diagram of CO_2, which are separated by three regions (A), (B) and (C). These regions correlate with the "three-stage structure" after the analysis of an angular distribution. (*right*) The depicted phase diagram of CO_2 is based on the combination of an EOS for the fluid phases and for the solid phase.[148,149]

I. Clusters from the supercritical CO_2 transited liquid phase and vapor-liquid phase boundary.

For the CO_2 jet expanded as a supercritical fluid, where the source entropy $S_0 < S_c$, the jet suffers pressure dropping as well as rapid cooling to the liquid phase at given entropy (a condensation process). Subsequently, the newly formed liquid jet undergoes the evaporation cooling process and meets the liquid-gas phase boundary when the temperature of the beam gets even lower.

It is worth to mention that, in earlier studies, Christen *et al.* have theoretically predicted the bifurcation of real flows with significant condensation after the co-phase boundary will not be fully isentropic, because the trajectory will include isothermal processes and move to different entropies in the T-S diagram.[49,147] Thus, using the real fluid EOS in combination with the isentropic process from the liquid jet might not yield a very precise terminal cluster temperature.

Experimentally, we have probed an extreme case at the source temperature of T_0 = 230.0 K from gas to liquid phase, where the small pressure change of 0.05 MPa can cause huge difference of source entropy (S_0) from 91.2 J/mol K to 28.1 J/mol K. At the source pressure of 0.87 MPa, in Figure 4.2-8, the CO_2 jet exhibits a gas expansion and results in only one component in the early time period. The scattered pattern also shows one angular distribution after the entire beam hit the Si(111)/SiO_2 surface.

On the other hand, notably, the liquid jet expansion from the source pressure of 0.92 MPa displays a clear separation of two components before and after scattering. From these two pressure settings, one might curious about whether the strong speed change in resulting CO_2 beams happens just at the macroscopic phase transition boundary. The detailed *in situ* experiments for CO_2 condensation by compressing the source fluid will be discussed in the next section. Here, two contributions from the angular distribution support the bifurcation concept that the continuously cooling liquid jet will split into two phases – vapor and liquid, which result in two branches of clusters. Namely, the dominated narrow contribution of terminal $(CO_2)_N$ clusters are formed via liquid fragmentation and arrive later in the TOF spectrum.

When supercritical CO_2 jet expansion at $S_0 < S_c$, the terminal CO_2 beams from this region also display two different patterns in different time periods. Figure 4.2-6 shows the scattering results with larger scattering angle and extremely narrow spread (the cosine exponent is very large) from the time period of 5.0 – 9.0 ms. This result indicates that those $(CO_2)_N$ clusters were formed via liquid channel. Concerning to the signal intensity (in Figure 4.2-9), the $(CO_2)_N$ clusters formed via liquid belong to the major channel. Oppositely, the minor contribution is revealed at the time period of 2.5 – 5.0 ms with smaller scattering angle and fairly narrow distribution (the cosine exponent of ~ 60). This contribution has demonstrated that small amount of clusters is formed via gaseous nucleation. The validation of gas is because of the expanded supercritical jet has already passed the vapor-liquid phase boundary.

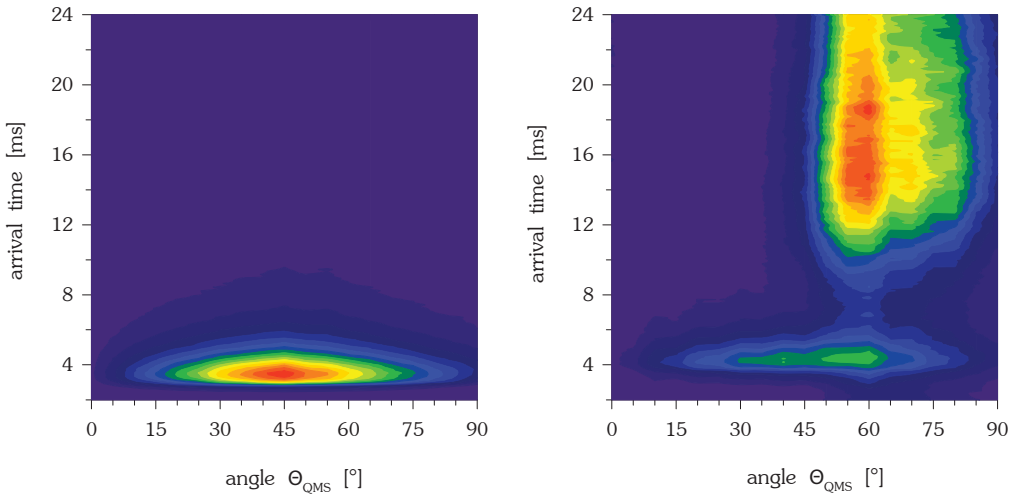

Figure 4.2-8 Difference in angular distributions of CO_2 gas jet and liquid jet. (*left*) Contour plot of time dependent scattering CO_2^+ monomer (m/z: 44) at S_0 = 91.2 J/molK while P_0 = 0.87 MPa from the gas expansion. (*right*) Scattering CO_2^+ monomer (m/z: 44) at S_0 = 28.1 J/molK while P_0 = 0.92 MPa from the liquid jet. The source temperature is fixed at T_0 = 230.0 K.

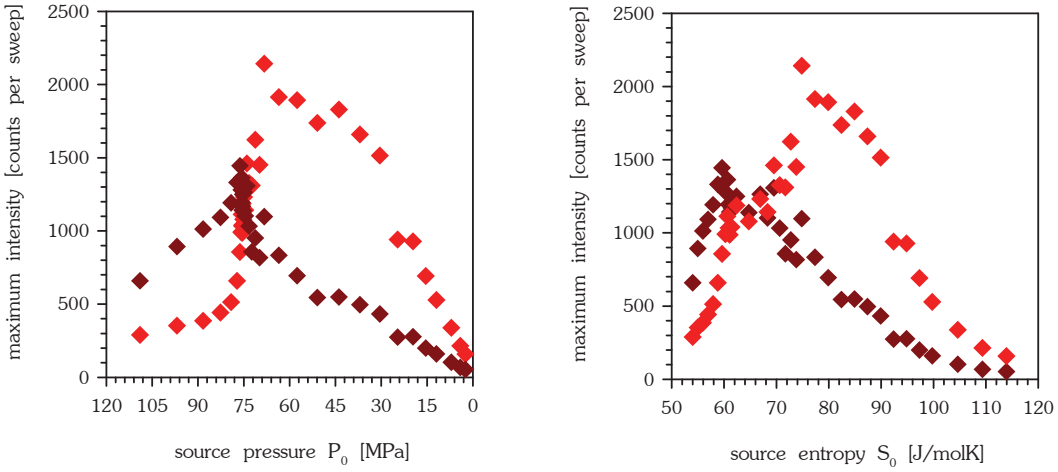

Figure 4.2-9 (*left*) T_0 = 305.0 K, maximum scattered monomeric CO_2^+ intensity with respect to each source pressure. Red squared symbol represents "early" [2.5–5.0 ms] period and dark red represents "late" [5.0 –9.0 ms] period. (*right*) The maximum scattered monomeric CO_2^+ intensities as a function of source entropies.

II. The supercritical/gas CO_2 beam passed co-phase boundary and formed clusters.

If the source entropy S_0 is smaller than 94.0 J/molK but greater than the critical entropy S_c (64.5 J/molK), the expanded CO_2 particles are going to transform from the supercritical/gas status and passing the liquid-gas phase boundary while the temperature of particles has dropped. That is to say, the CO_2 jet will partially turn to the liquid droplets due to the spinodal decomposition and the non-equilibrium status of the beam. As a result, after these beams were scattered off the surface, similar to the last section, two channels appear at different time periods.

Apparently, the dominated contribution at the time period of 2.5 – 5.0 ms should be the clusters formed via gaseous nucleation, which result decreasing scattering angle and constantly narrow distribution when the entropy increases. This observation in Figure 4.2-5 (*lower right*) indicates that the angular spread (exponent term) might not strongly depend on the change in size but the origin of the clusters. To verify the hypothesis, when the source entropy increases, the minor contribution of $(CO_2)_N$ clusters formed by liquid droplet shows diminution in scattering angle and gradually broaden spread from the cosine exponent of ~ 200 to ~ 50, see Figure 4.2-6 (*lower right*). Therefore, the exponent term seems to be an indicator of cluster formation channel: the exponent term is ~ 200 for the clusters from liquid fragmentation and ~ 50 for the clusters from gases aggregation. The value will be varied if the composition of each phase in the jet is altered. Again, the scattering pattern is a useful tool to differentiate the fragmented particles from different channels.

III. Clusters formed solely through the gas phase.

When the gaseous CO_2 molecules only collide and bond with each other after the rapid cooling of jet expansion, which represents the typical nucleation process. In the *T*–*S* phase diagram, Figure 4.2-6 (*right*), the depicted line indicates this nucleation process is moving along the isentropic path from the initial high temperature to the lower terminal temperature. For the given source entropy larger than S_0 = 94 J/molK, the aggregated $(CO_2)_N$ clusters might travel through the solid-gas phase boundary when the final temperature is lower than ~ 200 K.

Experimentally, we have verified the terminal temperature of $(CO_2)_N$ cluster at around 138 K for the source conditions in this study, the derivation of final temperature based on the equation of states (EOS) was already mentioned in section 4.1. As a result, the higher source entropy represents the lower density of source particles as well as the lower internal energy of individual particles at given temperature, which causes less efficient collisional congregation and is expected to form smaller $(CO_2)_N$ clusters. When the impacted cluster size is getting smaller, as source entropy S_0 changes from 94 to 104 J/molK, the scattering profile of fragmented CO_2^+ monomer displays sole cosine contribution toward smaller angle (Θ_{QMS}) and simultaneously become broader (cosine exponent below 10).

Summary: channel assignment of $(CO_2)_N$ clusters in the scattered beams.

After comparing the *T*–*S* phase diagram to the comprehensive scattering pattern of $(CO_2)_N$ and extracting the systematical information from each stage, in Figure 4.2-10, the formation of $(CO_2)_N$ clusters in the jet expansion seems to be resolved through three major channels:

1. Monomers numerously generated at surface impact of arbitrary $(CO_2)_N$ clusters, which show broad contribution in the whole time ranges.

2. Clusters generated via gaseous growth mechanism: the fragmented $(CO_2)_N$ arrive early and display narrow angular spread constantly.

3. Clusters generated via liquid degradation mechanism: the fragmented $(CO_2)_N$ arrive late and spread extremely narrower when the source entropy is decreased.

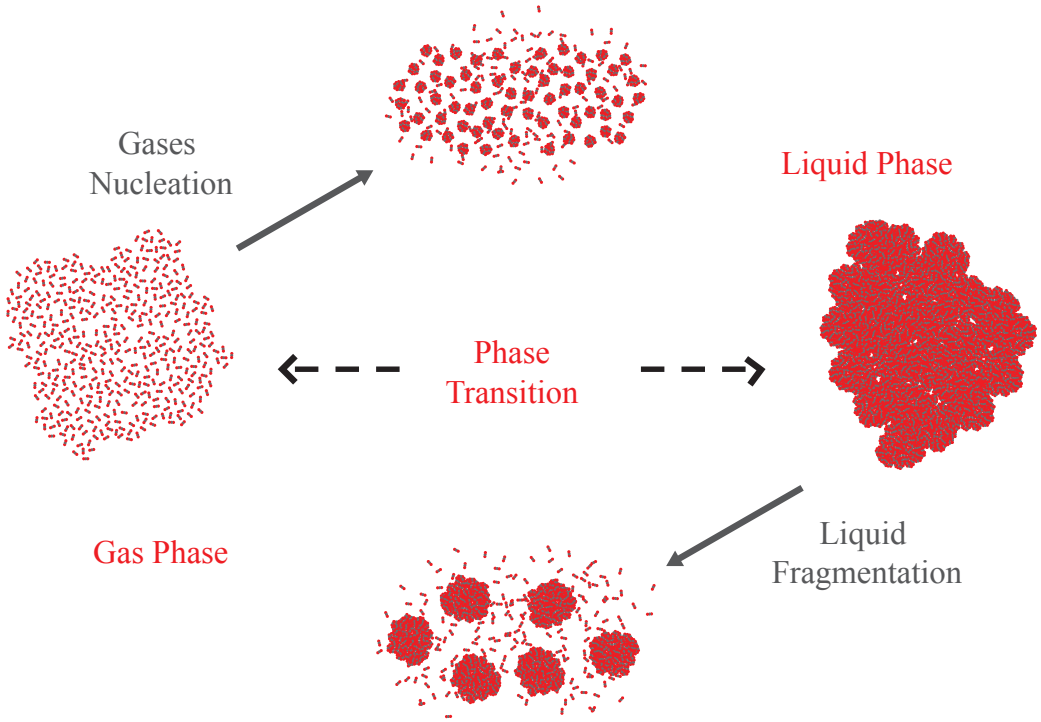

Figure 4.2-10 The concept of two cluster formation channels: aggregation of particles from the gas phase and the fragmentation process from liquid phase, which could happen at the same time as the phase transition has already started in the nozzle during the jet expansion.

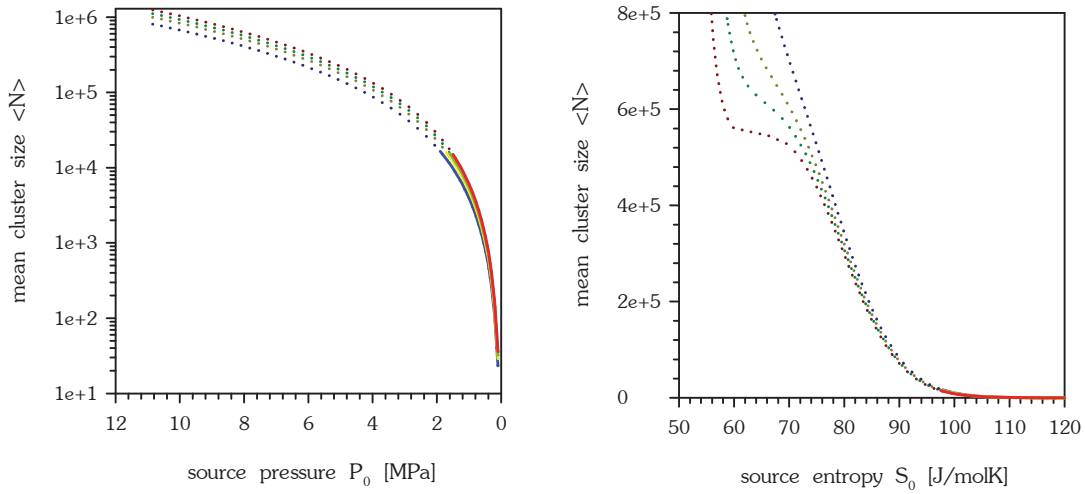

Figure 4.2-11 Solid curve (–), scaling law based on the experimental fitting; dashed curve (---), extrapolated region at higher source pressures T = 305.0 (red), 310.0 (yellow), 315.0 (green) and 325.0 K (blue). Mean cluster size as a function of source pressure (*left*) or entropy (*right*).[104,107]

4.2.4 Discussion: Size Effect of Scattering

To move forward a step, after scanning a wide range of CO_2 beams from the ultra-high density sources, the size of generated clusters from different channels are of interests to substantiate the nucleation process. For those CO_2 jet expansions, we have applied Hagena's empirical scaling law to estimate the mean cluster size from T_0 = 305.0 – 325.0 K and P_0 = 0.20 –11.00 MPa.

Combining the source temperature and pressure, further considering the nozzle shape (see section 2.2.3, half opening angle of 8°), the clusters formed in jet expansions result mean size distribution of $\langle N \rangle = 10^3 - 10^5$. Nevertheless, the outputs from current source settings include the presumed range where no experimental data were endorsed. Figure 4.2-11 distinguishes the extrapolated region of size from the validated range of Hagena's expressions; this narrow range at lower entropy (higher pressure) needs to be improved by the measurements in this study.

It is known that the scattering angle of inelastic outgoing particles will be varied by the original size of incoming particles. This correlation helps us to trace the growth of clusters in entire experiments. In Figure 4.2-5 and Figure 4.2-6 (*upper right*), the derived trends of scattering angles from the detected monomers, both early and late arrived, show similar curve between S_0 = 75 – 120 J/molK. The result displays that the cluster growth depends on the source entropy in jet expansion but not to the vicinity of the critical point.

When the source entropy is close to the critical entropy, the strong effect of condensation in the beam limits the later aggregation of CO_2 particles. For the earlier arrived clusters via gaseous aggregation, the slight decrease of scattering angle (after the source entropy were reduced from S_0 = 64 to 55 J/mol K) infers that the cluster is not growing further. Instead, the partial condensation reduces the mean cluster size in this manner. On the other side, the scattering angle from the late arrived CO_2^+ monomers seems to remain unchanged in the vicinity of the critical entropy. This phenomenon shows that the empirical scaling law is not applicable to the size of clusters generated via liquid degradation process. For those clusters that are fragmented from large droplets, in principle, one should estimate the dimensions according to the surface tension of droplets and the size of the nozzle exit (see section 2.2.3).

Note that, this deviation from the empirical law of mean cluster size at higher source densities has also been considered in the literature,[157] where the condensation parameter (Γ^*) here is calculated to be larger than 10^4 for argon clusters. After all, the classic scaling law should take an upper limit into consideration while the condensable gas has rapidly turned into liquid droplets before the jet is fully expanded to the vacuum, which no longer performs the pure nucleation of gaseous particles in the beam.

To sum up the results of these experiments, we have measured the angular-, mass- and time-resolved scattering of $(CO_2)_N$ clusters. By changing the source parameters of pressure and temperature over a broad range with high precision, we produce large and solid $(CO_2)_N$ clusters, which were scattered off the Si(111)/SiO_2 surface. The estimated mean cluster size is in the range of $\langle N \rangle = 10^3 - 10^5$. The angular distribution of monomer is asymmetric and strongly depends on source conditions, up to a threshold (close to the critical entropy).

Followed by comparing pressure and density, two main conclusions will be highlighted. Firstly, we have identified that the most relevant source parameter is the initial entropy (S). It defines the expansion path. Secondly, at higher entropies, the $(CO_2)_N$ clusters condense from pure gas phase jet expansions. On the other side, at lower entropies, the $(CO_2)_N$ clusters were generated mostly from the evaporation/fragmentation mechanism of liquid droplets.

In summary, the $(CO_2)_N$ cluster scattering show two major channels of the angular distribution depending on the initial entropy. We finally emphasize that no diffusive trapping-desorption mechanism from surface has been observed. When source entropy changes between S_c to S = 94 J/molK, the jet expansions cross the metastable liquid-gas phase boundary.

4.3 Phase Transition at the Nanometer Scale

From the last section, we have learned that the initial energetic status affects the cluster formation in an adiabatic jet expansion. In particular, the time-resolved analysis of spectra reveals a strong change in arrival time over large pressure ranges at a given source temperature. This experimental observation of a pronounced change in the terminal flow velocity is explained in terms of a thermodynamic model, which has been highlighted by Christen *et al*. in earlier studies.[49,147] An isentropic expansion path of working fluid can therefore be portrayed as indicating the jet expansion crosses the vapor-liquid phase boundary within a certain range of entropies. The main prediction of this model is a distinct pressure dependence of the mean terminal flow velocity that is caused by condensation during the jet expansion.

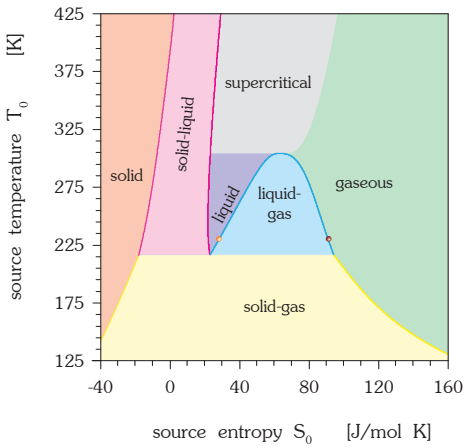

Figure 4.3-1 CO_2 *T*–*S* phase diagram. In this graph, the yellow dot on the left side of liquid-gas co-phase boundary represents the source condition of S_0 = 28.1 J/molK and T_0 = 230.0 K for the experiment of liquid jet expansion. Another brown dot at the right side of liquid-gas co-phase boundary represents the source condition of S_0 = 91.2 J/molK and T_0 = 230.0 K for a gas jet. This *T*–*S* phase plot is generated by the combination of an EOS for the fluid phases and for the solid phase.[49,148,149]

4.3.1 Jet Expansions: From Gas to Liquid

For a regular CO_2 gas expansion from a source temperature of T_0 = 230.0 K (Figure 4.3-1), the terminal CO_2 neutrals are recorded by a QMS is shown in Figure 4.3-2. As the source pressure is set at P_0 = 0.87 MPa, the calculated source density of the real fluid EOS is 0.5132 mol/dm^3.[107] This source density can be enlarged about 50 times higher to 26.648 mol/dm^3 by an increase of 5 % of the source pressure to P_0 = 0.92 MPa. As a result, the high-density liquid jet was expanded, which showed another shape of arrival time distribution also in Figure 4.3-2. Clearly, the liquid jet has a "slower" (than the gas jet) first peak and a broad "late-arrived" bunch.

As discussed in the previous section, the broad "late-arrived" bunch from the P_0 = 0.92 MPa can be directly related to the $(CO_2)_N$ clusters which come from liquid fragmentation. On the other hand, when the leading sharp peak is compared to another sharp peak from the lower source pressure P_0 = 0.87 MPa, although both peak shapes are

similar, the mean arrival time of each of them is already slightly different. This remaining sharp peak from the P_0 = 0.92 MPa could relate to a spinodal decomposition during the liquid jet expansion or simply some CO_2 gases from the non-equilibrium process during nozzle operation. To rule out the effect of the nozzle operation, one can use electronic tagging in combination with the MCP detector to select the steady state segment of the beam.

For the spinodal decomposition, the initial liquid jet is supercooled during the isentropic expansion process, if valid, and thus passes the vapor-liquid phase boundary, see Figure 4.3-1. Besides the majority of the liquid jet, the phase separation afterwards yields a minor contribution of gases, which consequently aggregates to the $(CO_2)_N$ clusters and shows up prior to the broad "late-arrived" bunch. This dramatic change seems to offer an opportunity for an *in situ* probe of the phase change from the velocity of $(CO_2)_N$ clusters. To begin, we choose to scan the phase change from the gas to the liquid, because the pulsed nozzle operation is mainly optimized for gas jet and may not be appropriate to liquid sources over a wide range of density.

4.3.2 From Gas to Vapor-Liquid Phase Boundary: On Site Velocity Study

The calculated viscosity of CO_2 fluid from source pressure of P_0 = 0.87 – 0.92 MPa at the temperature of T_0 = 230.0 K is depicted in Figure 4.3-3. Apparently, the "cliff" structure of the sudden change in viscosity comes from the boundary pressure of P = 0.8929 MPa in the real gas EOS,[107] which reflects the gas to liquid phase transition from a macroscopic point of view. Theoretically, Christen *et al.* has already predicted a pronounced change of beam velocities originating from the vicinity of the gas–liquid phase transition or the critical point by thermodynamic descriptions of elevated pressures.[158] Experimentally, in a pulsed jet expansion, if the effective source pressure in the quasi-continuous region reaches this boundary, the partial condensation may start and, therefore, results slower beam. Here, the phase of the beam will not totally convert to the liquid because the rest part of pulsed beam stays at gas phase and the sudden condensation also diminishes the differential pressure within quasi-continuous region. In the end, the sudden change of mean terminal velocity should be observed.

To eliminate the non-equilibrium process during nozzle operation, we electronically excite the narrowest and quasi-equilibrium region of each CO_2 pulse. According to the TOF measurements by MCP detector, the mean arrival time is plotted in Figure 4.3-4. Here, the error function like distribution shows two stages and one transition region. The source pressures lower than P_0 = 0.843 MPa (in 0.001 MPa interval) results faster beam which arrives at ~ 4.4 ms, while the source pressure above P_0 = 0.875 MPa results slower beam which arrives at ~ 4.8 ms. Just between these two districts, the transition region displays a strong oscillation of mean arrival time to the source pressure. Although the source pressure is slightly lower than the calculated boundary pressure of P = 0.8929 MPa (from EOS), the recent study by D. Rupp *et al.* also mentioned that the additional compression by valve operation might lead the effective pressure to this

theoretical boundary during the pulse.[159] Clearly, the onset condensation starts already in this transition region, thus, the ratio of gas and liquid is varying.

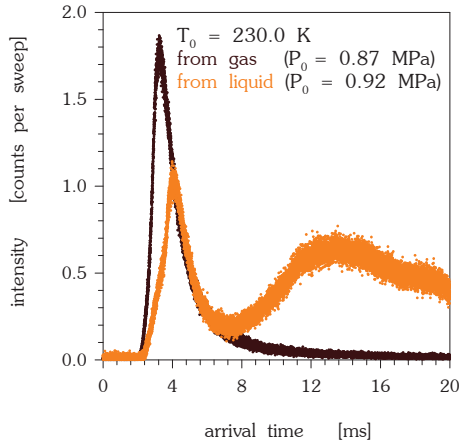

Figure 4.3-2 Illustration of CO_2 gas jet and liquid jet recorded by QMS. As the source temperature is fixed at T_0 = 230.0 K, the arrival time distributions are obtained by CO_2 source condition at S_0 = 91.2 J/molK while P_0 = 0.87 MPa from the gases expansion and S_0 = 28.1 J/molK while P_0 = 0.92 MPa from the liquid jet.

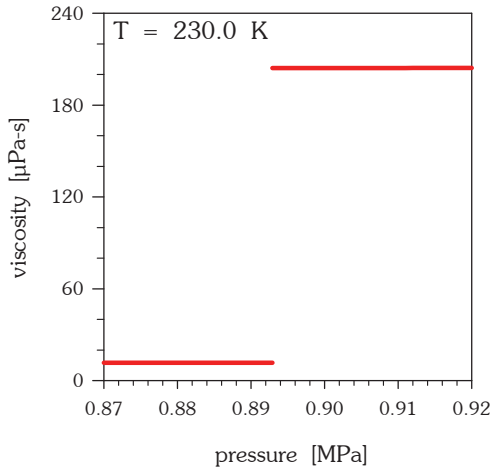

Figure 4.3-3 Calculated CO_2 viscosity change by the real gas equation of state.[107] The temperature of CO_2 is fixed at 230 K while the pressure is varied from 0.87 to 0.92 MPa. A large step in viscosity demonstrates the sudden change from $CO_{2(g)}$ to $CO_{2(l)}$ with distinct difference in their flow properties and initial energies.

Another possible influence of this ratio could be the external control of pressure and temperature. For the source temperature at T_0 = 230.0 K, the thermal stability of source temperature is $\Delta T_0 < 30$ mK,[32,160] which is corresponding to 0.01%. On the other hand, for the source pressure, our syringe pump allows a stability of $\Delta P_0 < 2.9$ kPa that causes 0.34% uncertainty in the range of P_0 = 0.843 – 0.875 MPa. To reduce the relative error from the experiment, a fixed source temperature at T_0 = 300.0 K (uncertainty < 0.01%) and pressure range of P_0 = 6.575 – 6.805 MPa (uncertainty < 0.04%) are chosen to probe the phase boundary.

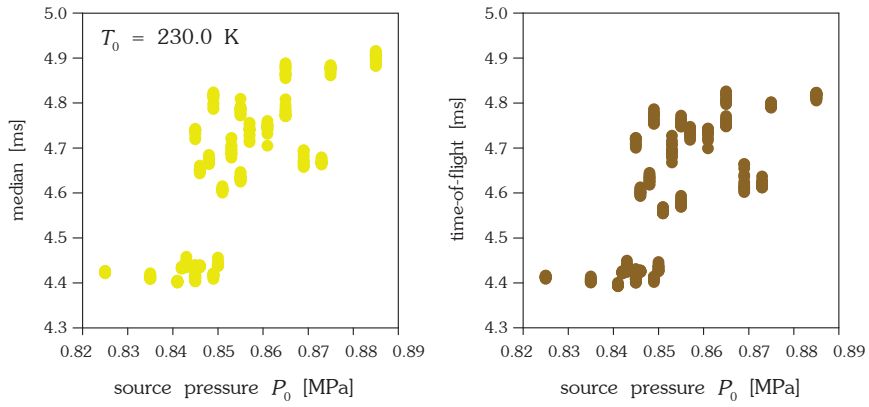

Figure 4.3-4 Sudden change of the beam velocity close to the vapor-liquid phase boundary. Pulsed CO_2 beam is electrically excited by e-gun, which determines the narrowest region inside of the beam. By ionizing CO_2 in this steady state region, the measured velocity of $(CO_2)_N^+$ displays a transition curve while the source pressure is increasing. Both statistical analysis (yellow) and the fitting results from student's t distribution (brown) show the similar changing of arrival time: from ~ 4.4 ms to ~ 4.8 ms by 0.02 MPa difference. All source temperatures of CO_2 beams are fixed at T_0 = 230.0 K.

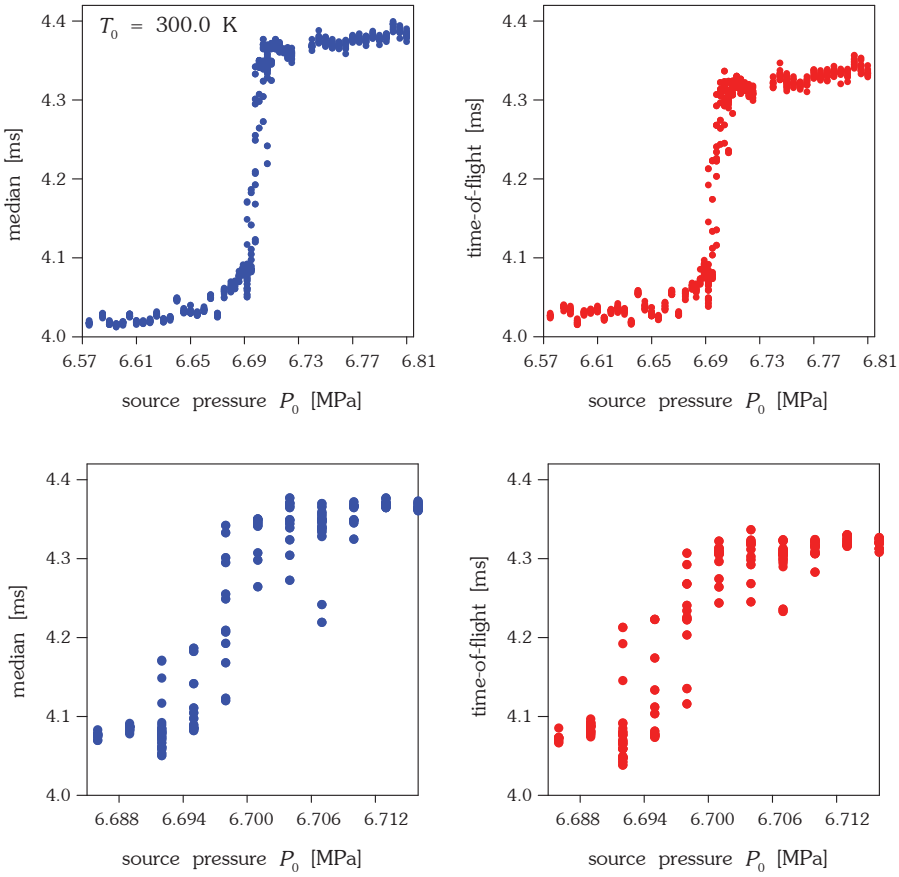

Figure 4.3-5 Clear "cliff" structure of terminal beam velocity near the CO_2 vapor-liquid phase boundary. By tagging the narrowest spread of CO_2 beams, the measured arrival time displays a step while the source pressure is continuously increased regardless of the statistical analysis (blue) or fitting results from student's t distribution (red). The upper row displays the change of terminal arrival time from ~ 4.0 ms to ~ 4.3 ms by 0.02 MPa when the source pressure was raised from 6.57 MPa to 6.81 MPa (overall 0.24 MPa). The lower row shows the magnified plots in the central region (only ~ 0.02 MPa difference) of the "cliff" structure. All source temperatures of CO_2 beams are fixed at T_0 = 300.0 K.

Figure 4.3-5 depicts a clear cliff structure in mean arrival time of terminal $(CO_2)_N$ beam, where the transition region covers the range of P_0 = 6.688 – 6.712 MPa. Profit from the reduced relative error, this metastable region ranges only 0.023 MPa which is narrower than the 0.043 MPa from previous experiment at T_0 = 230.0 K. Also the vapor-liquid phase boundary pressure of P = 6.713 MPa at T = 300.0 K seems to be very close to the experimental upper limit of transition region. That is to say, when the terminal velocity of $(CO_2)_N$ totally turns to "slow" mode, the CO_2 phase in the nozzle has already passed the vapor-liquid phase boundary.

To sum up, a strong correlation between the source phase condition and the terminal $(CO_2)_N$ velocity has been demonstrated. Because the formation path of $(CO_2)_N$, either from gas condensation or liquid fragmentation, involves different energetic transformation during the jet expansion, which alters the terminal arrival time of $(CO_2)_N$ to the MCP detector. Also, two distinct particle distributions of the $(CO_2)_N$ observed by QMS detector (Figure 4.3-2) differentiate gases CO_2 jet from liquid CO_2 jet. These results are in good agreement with the theoretical prediction.

4.4 Conclusions

A comprehensive study of supersonic jet expansions of CO_2 from the vapor, liquid, and supercritical phase is reported, employing ultra-high precision time-of-flight measurements of neutral/positively charged clusters. Subsequently, those large $(CO_2)_N$ clusters were scattered off a Si(111)/SiO_2 surface and analyzed by angular-, mass- and time-resolved QMS. By comparing the pressure, density, and initial entropy, four main conclusions will be highlighted.

First, we have identified that the most relevant source parameter is the initial entropy (S_0). It defines the expansion path.

Secondly, at higher entropies, the $(CO_2)_N$ clusters condense from the pure gas phase jet expansions. On the other side, at lower entropies, the $(CO_2)_N$ clusters were generated mostly from the evaporation/fragmentation mechanism of liquid droplets.

Third, even though the $(CO_2)_N$ cluster size seems to depend on the source entropy, the mean terminal temperature derived from the thermodynamic EOS is T_1 = 138 ± 4 K unrelated to source conditions. This result suggests that the cluster temperature is related to the evaporative cooling from the surface of the cluster.

Finally, rapid cooling causes the phase transition during the reversible adiabatic jet expansion, which is found to affect the cluster formation at very early stages. Meanwhile, at a given source temperature, the dramatic change of mean flow velocity illustrates a "visible liquid-gas phase boundary" revealed by an accurate pressure dependence.

CHAPTER 5

5 Summary and Outlook

5.1 Summary

This work has advanced the control of cluster beam by revealing the source entropy as a key factor, which allows precise probing of several physical properties of generated clusters in the supersonic beam. As a cluster always bridges the atomic level to the macroscopic, the improved understanding of clusters shows that the macroscopic thermodynamic properties can apply to the cluster size as small as ~ 10^3 atoms/molecules per cluster. These determinations from comprehensive and extreme source conditions provide the abundant references for improving the theoretical calculations.

VELOCITY For atomic beams such as a helium beam, the precise velocity represents a translational energy of the particles. Subsequently, the accurate kinetic energy determines a reliable enthalpy change, which as was demonstrated allows for the possibility of applying the fundamental equation of state to determine other physical properties e.g. terminal temperature of particles. A steady state source condition finally provides a meaningful examination of beam properties in pulsed ultra-high pressure jet expansions, regardless of the dramatic increasing or decreasing of flow densities during the mechanical valve operation. Stepwise evaluating the electronic slicing of the maximum signal intensity, the relative change of arrival time and the speed ratio of each part of the beam, the minimum effective opening duration is derived to reach the quasi-continuous flow properties in the pulsed jet. In parallel, to minimize the interference during the jet expansion, a systematic study of skimmer positioning as well as the residual gas effects have been carefully analyzed. Followed by using a translational stage with accurately adjustable length, the precise relative time difference per unit distance permits well-characterized mean speed with high reproducibility. In the end, a precision in the mean flight time of particles of better than 10^{-4} is achieved. Based on the ultra-high precision time-of-flight measurements, for the real gas system, we have thoroughly investigated both neutral and charged molecular clusters from the CO_2 jet expansions. The result is dedicated to reducing the uncertainty of mean flow velocities of supersonic beams in magnetic/electric deflection experiments and reactivity studies.

SCATTERING PATTERN We have measured the angular-, mass- and time-resolved scattering of $(CO_2)_N$ clusters. Again, by changing the source parameters of pressure and temperature, large and solid clusters, estimated mean cluster size $\langle N \rangle = 10^3 - 10^5$, were scattered off Si(111)/SiO_2 surface. The angular distribution of monomer is asymmetric and strongly depends on source entropies, S_0, up to a threshold (close to the critical entropy). Followed by comparing to pressure and density, the relevant source parameter is initial entropy, which defines the expansion path.

CLUSTER FORMATION CHANNEL Our results from the $(CO_2)_N$ cluster scattering show two major channels of the angular distribution; no diffusive trapping-desorption from the surface has been observed. According to the cosine fitted description, both scattering angle and distribution width show three distinct regions. At higher entropies, the $(CO_2)_N$ clusters condense from the pure gas phase jet expansions. On the other side, at lower entropies, the $(CO_2)_N$ clusters were generated mostly from the evaporation/fragmentation process of liquid droplets. When source entropy changes between S_c to $S = 94$ J/molK, the jet expansions cross the metastable liquid-gas phase boundary. The scattering angles of $(CO_2)_N$ clusters generated by co-phase process change certainly as the liquid/gas fraction change.

PHASE As the $(CO_2)_N$ clusters are comprehensively generated from supersonic expansions of CO_2 from the vapor, liquid, and supercritical phases, the phase alteration from the initial to terminal status affects the mean flow velocity of the cluster beam. In particular, when the source status sits close to the gas-liquid phase boundary, a second peak in the time-of-flight spectra emerges. These two peaks and aforementioned two separated channels of scattered clusters both can seamlessly be explained by partial condensation within the valve, resulting in solid clusters from the vapor phase (faster particles) and the liquid phase (slower particles). The predicted bifurcation limit has been experimentally confirmed by analysis of arrival time distribution of neutral $(CO_2)_N$ clusters.

5.2 Outlook

CLUSTER SIZE After verifying the interaction of cluster to skimmer in multiple degrees, the terminal cluster size distributions are clearly changed. The degradation of size appears when the beam–skimmer scattering is getting larger, which is measured by QMS with the diminishing of cluster masses. Currently, the widely used Hagena's empirical scaling equation contains no skimmer related terms, which should be revised more carefully in the future for cluster references. To achieve the goal, the tunable translation stage of nozzle to skimmer distance is still the most convenient tool to offer the continuous data string of downstream size distributions and step forward to modify the existing model of scaling law. The advanced technology to precisely define the particle size is an important issue in metrology, which will essentially contribute to the environmental analysis of aerosol in meteorology and further extend to simulate various atmospheric conditions of other planets in astronomy.

MIXED CLUSTER The success in predicting cluster status via macroscopic *T*–*S* phase diagram with pure compounds (carbon dioxide, CO_2) opens up the possibility to probe the mixed clusters by co-expansion process. An interesting issue will be whether the cluster is homogeneously mixed or segregated. If the cluster exhibits the homogeneous aggregation, the challenge could be to apply the binary phase diagram to characteristic the size or temperature of mixed clusters; on the other hand, if the cluster undergoes the core-shell structure, one can apply the surface scattering and probe the sputtering pattern to learn about the kinetic mechanism. The result may include the improvement of transferring the non-volatile biomolecules to the gas phase, which is of interest to the pharmaceutical research by cutting-edge optical and magnetic analysis.

6 Appendices

6.1 Bibliography

(1) Tully, R. B.; Courtois, H.; Hoffman, Y.; Pomarede, D. *Nature* **2014**, *513*, 71.

(2) Bauerecker, S. *Physical Review Letters* **2005**, *94*, 033404.

(3) Bush, A. M.; Bell, A. J.; Frey, J. G.; Mestdagh, J. M. *Journal of Physical Chemistry A* **1998**, *102*, 6457.

(4) Bonnamy, A.; Georges, R.; Hugo, E.; Signorell, R. *Physical Chemistry Chemical Physics* **2005**, *7*, 963.

(5) Bonnamy, A.; Georges, R.; Benidar, A.; Boissoles, J.; Canosa, A.; Rowe, B. R. *Journal of Chemical Physics* **2003**, *118*, 3612.

(6) Johnson, B. P.; Dielmann, F.; Balazs, G.; Sierka, M.; Scheer, M. *Angewandte Chemie-International Edition* **2006**, *45*, 2473.

(7) Farges, J.; de Feraudy, M. F.; Raoult, B.; Torchet, G. *Journal of Chemical Physics* **1986**, *84*, 3491.

(8) Golomb, D.; Good, R. E.; Busby, M. R.; Bailey, A. B.; Dawbarn, R. *Journal of Chemical Physics* **1972**, *57*, 3844.

(9) Gspann, J. *Journal of Chemical Physics* **1973**, *59*, 4726.

(10) Hartke, B. *Angewandte Chemie-International Edition* **2002**, *41*, 1468.

(11) Hoare, M. R.; Pal, P. *Advances in Physics* **1975**, *24*, 645.

(12) Lohr, L. L. *Molecular Physics* **1995**, *85*, 607.

(13) Ikeshoji, T.; Hafskjold, B.; Hashi, Y.; Kawazoe, Y. *Journal of Chemical Physics* **1996**, *105*, 5126.

(14) Disselkamp, R.; Ewing, G. E. *Journal of Chemical Physics* **1993**, *99*, 2439.

(15) Marković, N.; Pettersson, J. B. C. *Journal of Chemical Physics* **1994**, *100*, 3911.

(16) Even, U.; Jortner, J.; Noy, D.; Lavie, N.; Cossart-Magos, C. *Journal of Chemical Physics* **2000**, *112*, 8068.

(17) Cheng, H. P.; Landman, U. *Science* **1993**, *260*, 1304.

(18) Hagena, O. F.; Obert, W. *Journal of Chemical Physics* **1972**, *56*, 1793.

(19) Jansen, R.; Wysong, I.; Gimelshein, S.; Zeifman, M.; Buck, U. *Journal of Chemical Physics* **2010**, *132*.

(20) Laksmono, H.; Tanimura, S.; Allen, H. C.; Wilemski, G.; Zahniser, M. S.; Shorter, J. H.; Nelson, D. D.; McManus, J. B.; Wyslouzil, B. E. *Physical Chemistry Chemical Physics* **2011**, *13*, 5855.

(21) Shieh, M.; Miu, C.-Y.; Huang, K.-C.; Lee, C.-F.; Chen, B.-G. *Inorganic Chemistry* **2011**, *50*, 7735.

(22) Chen, B.-G.; Ho, C.-H.; Lee, C.-J.; Shieh, M. *Inorganic Chemistry* **2009**, *48*, 10757.

(23) Shieh, M.; Ho, C.-H.; Sheu, W.-S.; Chen, B.-G.; Chu, Y.-Y.; Miu, C.-Y.; Liu, H.-L.; Shen, C.-C. *Journal of the American Chemical Society* **2008**, *130*, 14114.

(24) Zacher, D.; Schmid, R.; Woll, C.; Fischer, R. A. *Angewandte Chemie-International Edition* **2011**, *50*, 176.

(25) Makiura, R.; Motoyama, S.; Umemura, Y.; Yamanaka, H.; Sakata, O.; Kitagawa, H. *Nature Materials* **2010**, *9*, 565.

(26) Lai, Y.-H.; Chen, B.-G.; Lee, Y. T.; Wang, Y.-S.; Lin, S. H. *Rapid Communications in Mass Spectrometry* **2014**, *28*, 1716.

(27) Buchenau, H.; Toennies, J. P.; Northby, J. A. *Journal of Chemical Physics* **1991**, *95*, 8134.

(28) Pollard, J. E.; Cohen, R. B. *Review of Scientific Instruments* **1987**, *58*, 32.

(29) Buchenau, H.; Knuth, E. L.; Northby, J.; Toennies, J. P.; Winkler, C. *Journal of Chemical Physics* **1990**, *92*, 6875.

(30) Bruch, L. W.; Schöllkopf, W.; Toennies, J. P. *Journal of Chemical Physics* **2002**, *117*, 1544.

(31) Vach, H.; Demartino, A.; Benslimane, M.; Châtelet, M.; Pradère, F. *Journal of Chemical Physics* **1994**, *100*, 8526.

(32) Christen, W.; Rademann, K. *Review of Scientific Instruments* **2006**, *77*, 015109.

(33) Hayden, C. C.; Penn, S. M.; Muyskens, K. J. C.; Crim, F. F. *Review of Scientific Instruments* **1990**, *61*, 775.

(34) Braun, J.; Day, P. K.; Toennies, J. P.; Witte, G.; Neher, E. *Review of Scientific Instruments* **1997**, *68*, 3001.

(35) Kroes, G. J. *Science* **2008**, *321*, 794.

(36) Pettersson, J. B. C.; Marković, N. *Chemical Physics Letters* **1993**, *201*, 421.

(37) Vach, H.; Benslimane, M.; Châtelet, M.; Demartino, A.; Pradère, F. *Journal of Chemical Physics* **1995**, *103*, 1972.

(38) Chaâbane, N.; Jundt, G.; Vach, H.; Koch, D. M.; Peslherbe, G. H. *International Journal of Mass Spectrometry* **2002**, *220*, 159.

(39) Fort, E.; Vach, H.; De Martino, A.; Châtelet, M.; Pradère, F. *European Physical Journal D* **1999**, *7*, 229.

(40) Heinbuch, S.; Dong, F.; Rocca, J. J.; Bernstein, E. R. *Journal of Chemical Physics* **2006**, *125*, 154316.

(41) Vach, H. *Physical Review B* **2000**, *61*, 2310.

(42) Holland, R. J.; Xu, G. Q.; Levkoff, J.; Robertson, A.; Bernasek, S. L. *Journal of Chemical Physics* **1988**, *88*, 7952.

(43) Fort, E.; Pradère, F.; De Martino, A.; Vach, H.; Châtelet, M. *European Physical Journal D* **1998**, *1*, 79.

(44) Lee, N.; Fenn, J. B. *Review of Scientific Instruments* **1978**, *49*, 1269.

(45) Tang, K.; Toennies, J.; Yiu, C. *Physical Review Letters* **1995**, *74*, 1546.

(46) Ramos, A.; Fernández, J. M.; Tejeda, G.; Montero, S. *Physical Review A* **2005**, *72*, 053204.

(47) Isenor, M.; Escribano, R.; Preston, T. C.; Signorell, R. *Icarus* **2013**, *223*, 591.

(48) Sipila, M.; Berndt, T.; Petaja, T.; Brus, D.; Vanhanen, J.; Stratmann, F.; Patokoski, J.; Mauldin, R. L., III; Hyvarinen, A.-P.; Lihavainen, H.; Kulmala, M. *Science* **2010**, *327*, 1243.

(49) Christen, W. *Journal of Chemical Physics* **2013**, *139*, 024202.

(50) Christen, W. *Journal of Chemical Physics* **2013**, *139*, 154202.

(51) Christen, W.; Krause, T.; Rademann, K. *Review of Scientific Instruments* **2007**, *78*, 073106.

(52) Märk, T. D. *International Journal of Mass Spectrometry* **1987**, *79*, 1.

(53) Gilmore, I. S.; Seah, M. P. *International Journal of Mass Spectrometry* **2000**, *202*, 217.

(54) Haberland, H.; Richter, T. *Zeitschrift für Physik D: Atoms Molecules and Clusters* **1988**, *10*, 99.

(55) Simpson, J. A.; Kuyatt, C. E. *Review of Scientific Instruments* **1963**, *34*, 265.

(56) Johnson, M. A.; Alexander, M. L.; Lineberger, W. C. *Chemical Physics Letters* **1984**, *112*, 285.

(57) NIST; NIST Standard Reference Data: http://webbook.nist.gov/chemistry/.

(58) Wiza, J. L. *Nuclear Instruments & Methods* **1979**, *162*, 587.

(59) Matsuura, S.; Umebayashi, S.; Okuyama, C.; Oba, K. *IEEE Transactions on Nuclear Science* **1985**, *32*, 350.

(60) Bahr, U.; Rohling, U.; Lautz, C.; Strupat, K.; Schurenberg, M.; Hillenkamp, F. *International Journal of Mass Spectrometry and Ion Processes* **1996**, *153*, 9.

(61) Feres, R.; Yablonsky, G. *Chemical Engineering Science* **2004**, *59*, 1541.

(62) Bergmann, P. G.; Lebowitz, J. L. *Physical Review* **1955**, *99*, 578.

(63) Lebowitz, J. L.; Frisch, H. L. *Physical Review* **1957**, *107*, 917.

(64) Millikan, R. A. *Physical Review* **1923**, *22*, 1.

(65) Steckelmacher, W. *Reports on Progress in Physics* **1986**, *49*, 1083.

(66) Gaede, W. *Annalen der Physik* **1913**, *41*, 289.

(67) Epstein, M. *AIAA Journal* **1967**, *5*, 1797.

(68) Clausing, P. *Annalen der Physik* **1930**, *4*, 533.

(69) Rideal, E. K. *Chpater III: Problems of the GasSolid Interface* The Cambridge Series of Physical Chemistry, University Press, 1929.

(70) Comsa, G. *Journal of Chemical Physics* **1968**, *48*, 3235.

(71) Palmer, R. L.; Smith Jr., J. N.; Saltsburg, H.; O'Keefe, D. R. *Journal of Chemical Physics* **1970**, *53*, 1666.

(72) Palmer, R. L.; O'Keefe, D. R. *Applied Physics Letters* **1970**, *16*, 529.

(73) Saftien, P., Diplomarbeit, Humboldt-Universität zu Berlin, 2015.

(74) Hurlbut, F. C. *Journal of Applied Physics* **1957**, *28*, 844.

(75) Perkins, B. G., Jr.; Nesbitt, D. J. *Proceedings of the National Academy of Sciences of the United States of America* **2008**, *105*, 12684.

(76) Ueta, H.; Gleeson, M. A.; Kleyn, A. W. *Journal of Chemical Physics* **2011**, *134*, 034704.

(77) Ertl, G. *Surface Science* **1979**, *89*, 525.

(78) Modl, A.; Gritsch, T.; Budde, F.; Chuang, T. J.; Ertl, G. *Physical Review Letters* **1986**, *57*, 384.

(79) Muhlhausen, C. W.; Williams, L. R.; Tully, J. C. *Journal of Chemical Physics* **1985**, *83*, 2594.

(80) Sarma, G.; Marinakis, S.; ter Meulen, J. J.; Parker, D. H.; McKendrick, K. G. *Nature Chemistry* **2012**, *4*, 985.

(81) Lu, J. W.; Alexander, W. A.; Morris, J. R. *Physical Chemistry Chemical Physics* **2010**, *12*, 12533.

(82) Holland, R. J.; Xu, G. Q.; Levkoff, J.; Robertson, A.; Bernasek, S. L. *Journal of Chemical Physics* **1988**, *88*, 7952.

(83) Tepper, G.; Miller, D. *Physical Review Letters* **1992**, *69*, 2927.

(84) Frankl, D. R. *Progress in Surface Science* **1983**, *13*, 285.

(85) De Martino, A.; Châtelet, M.; Pradère, F.; Fort, E.; Vach, H. *Journal of Chemical Physics* **1999**, *111*, 7038.

(86) Lee, Y. T. *Science* **1987**, *236*, 793.

(87) Van De Meerakker, S. Y. T.; Bethlem, H. L.; Meijer, G. *Nature Physics* **2008**, *4*, 595.

(88) Toennies, J. P. *Annual Review of Physical Chemistry* **2004**, *55*, 1.

(89) Saenger, K. L. *Journal of Chemical Physics* **1981**, *75*, 2467.

(90) Campargue, R. *Journal of Physical Chemistry* **1984**, *88*, 4466.

(91) Jones, G. G.; Taylor, J. W. *Journal of Chemical Physics* **1978**, *68*, 1768.

(92) Lee, N.; Fenn, J. B. *Review of Scientific Instruments* **1978**, *49*, 1269.

(93) Barker, J. A.; Auerbach, D. J. *Surface Science Reports* **1984**, *4*, 1.

(94) Scoles, G. *Atomic and Molecular Beam Methods*; Oxford University Press, 1988.

(95) Campargue, R. *Atomic and Molecular Beams: The State of the Art 2000*; Springer, 2001.

(96) Libuda, J.; Freund, H. J. *Surface Science Reports* **2005**, *57*, 157.

(97) Gedcke, D. A. *How Histogramming and Counting Statistics Affect Peak Position Precision*, Ortec Application Note AN58, 2005.

(98) Christen, W.; 2.6.3 ed.; SATRECH–Signal Analysis of Time-Resolved Event Counting Histograms: 2013.

(99) Christen, W.; ATD Fit, Arrival Time Distribution Fit: 2009.

(100) Hagena, O. F. *Surface Science* **1981**, *106*, 101.

(101) Hagena, O. F. *Zeitschrift für Physik D: Atoms, Molecules and Clusters* **1987**, *4*, 291.

(102) Hagena, O. F. *Review of Scientific Instruments* **1992**, *63*, 2374.

(103) Jansen, R.; Wysong, I.; Gimelshein, S.; Zeifman, M.; Buck, U. *Journal of Chemical Physics* **2010**, *132*, 244105.

(104) Harnes, J.; Winkler, M.; Lindblad, A.; Sæthre, L. J.; Børve, K. J. *Journal of Physical Chemistry A* **2011**, *115*, 10408.

(105) Knuth, E. L.; Henne, U. *Journal of Chemical Physics* **1999**, *110*, 2664.

(106) Christen, W.; Krause, T.; Kobin, B.; Rademann, K. *Journal of Physical Chemistry A* **2011**, *115*, 6997.

(107) Lemmon, E. W.; Huber, M. L.; McLinden, M. O. *NIST reference fluid thermodynamic and transport properties–REFPROP*; Version 9.1, 2013.

(108) Toennies, J. P.; Vilesov, A. F. *Angewandte Chemie-International Edition* **2004**, *43*, 2622.

(109) Van Dyck, R. S.; Johnson, C. E.; Shugart, H. A. *Physical Review A* **1971**, *4*, 1327.

(110) Hodgman, S. S.; Dall, R. G.; Byron, L. J.; Baldwin, K. G. H.; Buckman, S. J.; Truscott, A. G. *Physical Review Letters* **2009**, *103*, 053002.

(111) Rundel, R. D.; Dunning, F. B.; Stebbings, R. F. *Review of Scientific Instruments* **1974**, *45*, 116.

(112) Irimia, D.; Dobrikov, D.; Kortekaas, R.; Voet, H.; van den Ende, D. A.; Groen, W. A.; Janssen, M. H. M. *Review of Scientific Instruments* **2009**, *80*, 113303.

(113) Christen, W.; Rademann, K.; Even, U. *Journal of Chemical Physics* **2006**, *125*, 174307.

(114) Eder, S. D.; Samelin, B.; Bracco, G.; Ansperger, K.; Holst, B. *Review of Scientific Instruments* **2013**, *84*, 093303.

(115) Yan, B.; Claus, P. F. H.; van Oorschot, B. G. M.; Gerritsen, L.; Eppink, A. T. J. B.; van de Meerakker, S. Y. T.; Parker, D. H. *Review of Scientific Instruments* **2013**, *84*, 023102.

(116) Wang, J.; Shamamian, V.; Thomas, B.; Wilkinson, J.; Riley, J.; Giese, C.; Gentry, W. *Physical Review Letters* **1988**, *60*, 696.

(117) Krause, T.; unpublished work, Humboldt-Universität zu Berlin: 2010.

(118) Luria, K.; Christen, W.; Even, U. *Journal of Physical Chemistry A* **2011**, *115*, 7362.

(119) Hillenkamp, M.; Keinan, S.; Even, U. *Journal of Chemical Physics* **2003**, *118*, 8699.

(120) Luo, F.; Giese, C. F.; Gentry, W. R. *Journal of Chemical Physics* **1996**, *104*, 1151.

(121) Chen, G.; Geng, X.; Xu, H.; Mi, Y.; Zhang, X.; Wang, L.; Kim, D. E. *AIP Advances* **2013**, *3*, 032133.

(122) Knuth, E. L. *Journal of Chemical Physics* **1997**, *107*, 9125.

(123) Bergersen, H.; Abu-samha, M.; Harnes, J.; Björneholm, O.; Svensson, S.; Sæthre, . J.; Børve, K. J. *Physical Chemistry Chemical Physics* **2006**, *8*, 1891.

(124) Lu, H.; Ni, G.; Li, R.; Xu, Z. *Journal of Chemical Physics* **2010**, *132*, 124303.

(125) Chen, G.; Kim, B.; Ahn, B.; Kim, D. E. *Journal of Applied Physics* **2010**, *108*, 064329.

(126) Takahashi, K.; Nakajima, M.; Hasegawa, J.; Horioka, K. *Journal of Applied Physics* **2013**, *113*, 024502.

(127) Stephens, P. W.; King, J. G. *Physical Review Letters* **1983**, *51*, 1538.

(128) Pedemonte, L.; Tatarek, R.; Bracco, G. *Review of Scientific Instruments* **2003**, *74*, 4404.

(129) von Haeften, K.; Laarmann, T.; Wabnitz, H.; Möller, T.; Fink, K. *Journal of Physical Chemistry A* **2011**, *115*, 7316.

(130) Feil, S.; Gluch, K.; Denifl, S.; Zappa, F.; Echt, O.; Scheier, P.; Märk, T. D. *International Journal of Mass Spectrometry* **2006**, *252*, 166.

(131) Kariotis, R.; Bruch, L. W.; Kornilov, O. *Journal of Chemical Physics* **2004**, *121*, 3044.

(132) Harms, J.; Toennies, J. P.; Knuth, E. L. *Journal of Chemical Physics* **1997**, *106*, 3348.

(133) Bentley, P. G. *Nature* **1961**, *190*, 432.

(134) Laksmono, H.; Tanimura, S.; Allen, H. C.; Wilemski, G.; Zahniser, M. S.; Shorter, J. H.; Nelson, D. D.; McManus, J. B.; Wyslouzil, B. E. *Physical Chemistry Chemical Physics* **2011**, *13*, 5855.

(135) Lu, H.; Chen, G.; Ni, G.; Li, R.; Xu, Z. *Journal of Physical Chemistry A* **2010**, *114*, 2.

(136) Dorfeld, W. G.; Hudson, J. B. *Journal of Chemical Physics* **1973**, *59*, 1261.

(137) Jiang, T.; Northby, J. *Physical Review Letters* **1992**, *68*, 2620.

(138) Northby, J. A. *Journal of Chemical Physics* **2001**, *115*, 10065.

(139) Christen, W.; Kompa, K. L.; Schröder, H.; Stülpnagel, H. *Berichte der Bunsengesellschaft für physikalische Chemie* **1992**, *96*, 1197.

(140) Tomsic, A.; Gebhardt, C. R. *Journal of Chemical Physics* **2005**, *123*, 64704.

(141) Perkins, B. G., Jr.; Nesbitt, D. J. *Proceedings of the National Academy of Sciences of the United States of America* **2008**, *105*, 12684.

(142) Nogueira, J. J.; Vazquez, S. A.; Lourderaj, U.; Hase, W. L.; Martinez-Nunez, E. *Journal of Physical Chemistry C* **2010**, *114*, 18455.

(143) Christen, W.; Rademann, K. *Physical Review A* **2008**, *77*, 012702.

(144) Sarfraz, A.; Rademann, K.; Christen, W. *Analytical and Bioanalytical Chemistry* **2012**, *404*, 2087.

(145) Christen, W.; Krause, T.; Rademann, K. *International Journal of Mass Spectrometry* **2008**, *277*, 305.

(146) Christen, W.; Geggier, S.; Grigorenko, S.; Rademann, K. *Review of Scientific Instruments* **2004**, *75*, 5048.

(147) Christen, W.; Rademann, K.; Even, U. *Journal of Physical Chemistry A* **2010**, *114*, 11189.

(148) Span, R.; Wagner, W. *Journal of Physical and Chemical Reference Data* **1996**, *25*, 1509.

(149) Jäger, A.; Span, R. *Journal of Chemical & Engineering Data* **2012**, *57*, 590.

(150) Chen, B. G.; Kositzki, R.; Heinig, S.; Krause, T.; Rademann, K.; Christen, W. In *DPG Frühjahrstagung* Stuttgart, Germany, 2012.

(151) Heinig, S., Bachelorarbeit, Humboldt-Universität zu Berlin, 2011.

(152) CERIC; Chemical Engineering Research Information Center, South Korea: http://www.cheric.org/.

(153) Kositzki, R., Diplomarbeit, Humboldt-Universität zu Berlin, 2012.

(154) Bobbert, C.; Schutte, S.; Steinbach, C.; Buck, U. *European Physical Journal D* **2002**, *19*, 183.

(155) Karnbach, R.; Joppien, M.; Stapelfeldt, J.; Wormer, J.; Möller, T. *Review of Scientific Instruments* **1993**, *64*, 2838.

(156) Xu, G. Q.; Holland, R. J.; Bernasek, S. L.; Tully, J. C. *Journal of Chemical Physics* **1989**, *90*, 3831.

(157) Dorchies, F.; Blasco, F.; Caillaud, T.; Stevefelt, J.; Stenz, C.; Boldarev, A.; Gasilov, V. *Physical Review A* **2003**, *68*.

(158) Christen, W.; Rademann, K. *Physica Scripta* **2009**, *80*, 048127.

(159) Rupp, D.; Adolph, M.; Flückiger, L.; Gorkhover, T.; Müller, J. P.; Müller, M.; Sauppe, M.; Wolter, D.; Schorb, S.; Treusch, R.; Bostedt, C.; Möller, T. *Journal of Chemical Physics* **2014**, *141*, 044306.

(160) Wünsche, H., Diplomarbeit, Humboldt-Universität zu Berlin, 2014.

6.2 List of Abbreviations

P	pressure
T	temperature
S	entropy
H	enthalpy
v	velocity
t	time
d	diameter of the nozzle
n_p	number of particles per pulse
l	length
γ	ratio of heat capacities, $\gamma = C_p$(constant pressure)/C_v(constant volume)
$\langle N \rangle$	mean cluster size, number of atoms/molecules per cluster
d_{N-S}	distance between nozzle and skimmer
UV	ultraviolet
SR	speed ratio
NP	nanoparticle
vdW	van der Waals force
EOS	equation of state
IQR	interquartile range
TOF	time-of-flight
UHV	ultra high vacuum
QMS	quadrupole mass spectrometry
MCP	micro-channel plate
PMT	photomultiplier tube
e-gun	electron gun
FWHM	full width at half maximum

TB, TD, TN, TS and TQ:
translational stage of beam blocker, detector, nozzle, surface and QMS

7 Publications (first author)

2014 [Conference] 247th American Chemical Society Spring Meeting, Dallas, USA, March

- Cluster Growth: $(CO_2)_n$ from dense supersonic beams and scattered off $Si(111)/SiO_2$ surface

2013 [Talk] Clustertreffen, Herzogenhorn im Schwarzwald, Freiburg, Germany, October

- Surface Scattering of $(CO_2)_n$ off $Si(111)/SiO_2$

2013 [Conference] Tag der Chemie, Potsdam, Germany, June

- Reference Beams from Dense Fluids

2012 [Conference] DPG Frühjahrstagung, Stuttgart, Germany, April

- Supersonic Beams of Neutral and Ionic CO_2 Clusters

2010 [Conference] 240th American Chemical Society Fall Meeting, Boston, USA, August

- The Role of Energy Threshold Played in MALDI: Studies from the Corresponding Measurements of Gly-Gly-His, Glu-Val-Phe and Three Matrices

2009 [Journal Article] *Inorg. Chem.* **2009**, *48,* 10757

- Copper Halide-Incorporated Tellurium-Iron Carbonyl Complexes: Transformation, Electrochemical properties, and Theoretical Calculations

Co-Authored Publications (selected)

2014 [Journal Article] *Rapid Commun. Mass Spectrom.* **2014**, *28*, 1716

- Contribution of Thermal Energy to Initial Ion Production in Matrix-Assisted Laser Desorption/Ionization Observed with 2,4,6-Trihydroxyacetophenone

2014 [Conference] Bunsentagung, Hamburg, Germany, May

- Surface Scattering of $(CO_2)_n$ off $Si(111)/SiO_2$

2013 [Conference] DPG Frühjahrstagung, Hannover, Germany, March

- Stationary Flow Conditions in Pulsed Supersonic Beams

2012 [Conference] Tag der Chemie, Berlin, Germany, June

- Phase Transitions at the Nanometer Scale

2011 [Conference] 5th International Symposium on Atomic Cluster Collisions, Berlin

- The Temperature of Clusters

2011 [Journal Article] *Inorg. Chem.* **2011**, *50,* 7735

- Stepwise Construction of Manganese Chromium Carbonyl Chalcogenide Complexes: Synthesis, Electrochemical Properties, and Computational Studies

2011 [Journal Article] *Russ. J. Inorg. Chem.* **2011**, *56,* 61

- Theoretical and Experimental Study of the Structure and Stability of Multiply Na-Substituted Glucose and 2,4,6-Trihydroxyacetophenone Derivatives

2008 [Journal Article] *J. Am. Chem. Soc.* **2008**, *130*, 14114

- Semiconducting Tellurium-Iron-Copper Carbonyl Polymers

Paper *in preparation*

- Supersonic $(CO_2)_N$ beams scattered off $Si(111)/SiO_2$ surface
- Optimized helium jet transmission and translational cooling
- From gas phase to vapor-liquid phase boundary: On site velocity study

8 Acknowledgements

After finishing my thesis, I first would like to thank my adviser, Prof. Dr. Klaus Rademann, at Humboldt University Berlin, for his scientific guidance, valuable discussion, and for organizing such an energetic working group in physical chemistry department. I really enjoy all his stories and his humor.

I acknowledge the strong support by Dr. Wolfgang Christen. He carried me from a chemist to the field of physics. He sharped my logical thinking as well as my integration skill by very fruitful discussions and exchange of ideas through the whole period of my Ph.D. work. I also learned a lot from him for being as precise as possible in many aspects. In the end, I would like to thank him for being an important role in commenting this thesis.

I enjoyed a lot of being a member of the Max Planck Society through the International Max Planck Research School: Complex Surfaces in Materials Science, we share ideas and experiences from different backgrounds. I am very grateful to Prof. Dr. Hajo Freund for accepting me to this IMPRS program and becoming the second adviser for my thesis. I will never forget such kind help and support from Mrs. Bettina Menzel at the FHI-MPG. Here, I would also like to thank Mr. Christopher Nicholson for proofreading this thesis.

To work as a Ph.D. student in Adlershof, many colleagues have supported me a lot during past four years. Mr. Tim Krause is the one who lead me to the technical issues for our UHV machine, without him I couldn't run all my experiments so efficient. Ms. Ramona Kositzki, Mr. Hannes Wünsche, Mr. Paul Saftien, Mr. Stefan Heinig, and Mr. Arnau Cobo all provide me a good discussion environment through various research topics. Our interns, Ms. Neha Ghotane and Ms. Elena Shylko, Ms. Yolanda Carrillo, and Ms. Jianchao Si, bring the lab more international prospects. I would like to thank them for listening to the "turbo band" with me in the cluster lab.

For the instrumental components, Mr. Bernd Lück and Mr. Sven Zillmann from the mechanical workshop always provide me the finest parts I required while Mr. Bernhard Buck and Mr. Helmut Draba from the electronic workshop also give me the technical support throughout the years. Also, all the assistance for documentation by Ms. Elizabeth Ehlers is really important for my stay and work in the Chemistry Institute in HU-Berlin. I would like to thank all of them by my awkward German "Vielen Dank!"

It is my pleasure to meet family Riech, Peter and Karin, started on the second day of my stay in Berlin. They are the best landlord ever for hosting me as a family member till now. I will always remember the East German stories they told me, the life attitudes they showed me as well as all encouragements they gave me in past 4 more years.

Finally, I thank my parents for their support from Taiwan, my sister for her greetings from USA and my wife for travel two times to Germany to accompany with me. I thank all the messages and Skype calls from MK, An-Chun, Yi-An and Chi-An in Taiwan and all the lovely friends, Pei-Shan, Ya-Ju, Chun-Yang, Shang-Ju, and Vince in Berlin.

Bo-Gaun Chen, Feb. 2015 in Berlin

9 Declaration (Selbständigkeitserklärung)

Hiermit versichere ich Bo-Gaun Chen (陳柏綱), Nationalität Taiwan R.O.C., die vorliegende Dissertation selbst verfasst und nur unter Zuhilfenahme der angegebenen Hilfsmittel angefertigt zu haben.

Berlin, den 23. 02. 2015 陳柏綱 Bo-Gaun Chen